



Aalborg Universitet

AALBORG UNIVERSITY
DENMARK

Humidity and temperature prediction for reliability of electronics

Hygum, Morten Arnfeldt

Publication date:
2015

Document Version
Early version, also known as pre-print

[Link to publication from Aalborg University](#)

Citation for published version (APA):

Hygum, M. A. (2015). *Humidity and temperature prediction for reliability of electronics*. Department of Physics and Nanotechnology, Aalborg University.

General rights

Copyright and moral rights for the publications made accessible in the public portal are retained by the authors and/or other copyright owners and it is a condition of accessing publications that users recognise and abide by the legal requirements associated with these rights.

- Users may download and print one copy of any publication from the public portal for the purpose of private study or research.
- You may not further distribute the material or use it for any profit-making activity or commercial gain
- You may freely distribute the URL identifying the publication in the public portal -

Take down policy

If you believe that this document breaches copyright please contact us at vbn@aub.aau.dk providing details, and we will remove access to the work immediately and investigate your claim.

Humidity and temperature prediction for reliability of electronics

Ph.D. Dissertation
Morten Arnfeldt Hygum

Dissertation submitted month 10, 2015

Thesis submitted: Month 10, 2015
PhD Supervisor: Assoc. Prof., Dr. Vladimir N. Popok,
Aalborg University
PhD Committee: Prof., Dr. Ulrich Rüde, University of Erlangen-
Nuernberg
Dr. Jens Peter Krog, Grundfos A/S
Assoc. Prof., Dr. Thomas Søndergaard, Aalborg Uni-
versity
PhD Series: Faculty of engineering and science, Aalborg University

ISBN: 87-89195-39-6

Published by:
Department of Physics and Nanotechnology, Aalborg University
Skjernvej 4A, DK-9220 Aalborg Øst
Phone +45 99 40 92 15. Fax +45 99 40 92 35.
www.nano.aau.dk

© Copyright by author

Printed by Uniprint
Aalborg, Denmark 2015

Abstract

Power electronics find applications in more and more harsh environments. To ensure reliable products it is important to predict the effect of various environmental stresses to which the electronics will be exposed to. Among them, humidity and temperature are the most common addressed factors. They are modeled and experimentally studied in the current work for different practically important cases in order to address the reliability issues.

The obtained results cover three main topics: (i) modeling and experimental investigation of humidity and temperature distribution and evolution in a test enclosure with increasing complexity (taking into account water evaporation), (ii) modeling of film condensation on a wall and (iii) reliability assessment of an enclosure for electronics based on climatic simulations.

The modeling for the first topic is carried out using finite element software tool. Firstly, the phenomenon thermodiffusion of water vapor in air in the test enclosure is investigated. It is found that this transport mechanism does not play a significant role for humidity-related reliability issues. As a next step, the local humidity distribution inside the test enclosure is studied including the water evaporation. This is carried out using a simplified expression for the mass flux at liquid-vapor interfaces which is based on so-called statistical rate theory. The role of convection is clarified and it is found to significantly affect the humidity evolution. The developed model is shown to be in good agreement with the conducted experiments. The final study in the first part is devoted to an investigation of so-called breathing effects of the test enclosure. Thermal gradients generated by operating electronics induce pressure gradients between the interior of the enclosure and its surrounding at openings (in practice, there are no completely hermetic enclosures). There will, therefore, be a convection and the developed model can predict this moisture migration. The model is also experimentally verified.

The second main topic deals with an extended version of the free surface lattice Boltzmann method. It is demonstrated how the method can be used to model film condensation, in particular, condensation of a liquid from the vapor phase on a vertical wall with downward stream. The developed approach, which is called the free surface entropic lattice Boltzmann method,

is verified by comparison with other well-proved theoretical and empirical models.

The final topic described in the thesis concerns an approach to use the developed climatic models for reliability assessment. The simulations are carried out for a model enclosure with a relatively simple geometry where the failing criterion is set to be the relative humidity at the location of a printed circuit board. The modeling is performed by combining a finite volume simulation of the water vapor distribution with a Monte Carlo sampling approach. This part, thus, shows an example on how to use the developed physical models to make reliability predictions in relation to environmental factors such as temperature and humidity.

Resumé

Effektelektronik bliver anvendt i stadig mere barske miljøer. For at sikre pålidelige produkter, er det vigtigt at kunne forudsige effekten af de forskellige miljømæssige belastninger, som elektronikken vil blive udsat for. Her er luftfugtighed og temperature blandt de mest almindelige kendte faktorer. I det nærværende arbejde er disse faktorer modelleret og eksperimentelt undersøgt for forskellige praktiske tilfælde for herved at adressere pålidelighedsproblemet.

De opnåede resultater dækker tre hovedemner: (i) modellering og eksperimentelle undersøgelser af luftfugtighed og temperaturfordelinger samt disses udvikling i en testindkapsling med en tiltagende kompleksitet (medtagende vandfordampning), (ii) modellering af filmkondensering på en væg og (iii) pålidelighedsvurdering af en indkapsling til elektronik baseret på klimatiske simuleringer.

Modelleringen ved første hovedemne er udført med software, der benytter elementmetoden. Først er fænomenet termodiffusion af fugt i luft i testindkapslingen undersøgt. Det er fundet, at denne transportmekanisme ikke spiller nogen signifikant rolle for fugtrelateret pålidelighedsproblemer. Som næste skridt er den lokale fugtfordeling inde i testindkapslingen studeret, hvor vandfordampning er inkluderet. Dette er gjort med et simplificeret udtryk for massestrømmen ved væske-damp grænsefladen, som er baseret på statistisk rateteori. Rollen for konvektion er klargjort, og denne er fundet have en signifikant betydning på fugtfordelingen. Den udviklede model er vist at være i god overensstemmelse med de udførte eksperimenter. Det sidste studie i den første del er allokeret til en undersøgelse af såkaldte åndingseffekter af testindkapslingen. Termiske gradienter genereret af den opererende elektronik inducerer trykgradienter mellem det indre af indkapslingen, og dets omgivelser ved åbninger (i virkeligheden er ingen hermetiske indkapslinger). Der vil derfor være konvektion, og den udviklede model kan forudsige denne fugtvandring. Modellen er også eksperimentelt verificeret. Det andet hovedemne omhandler en udvidet version af den frie overflade gitter Boltzmann metode. Det er demonstreret, hvordan metoden kan anvendes til at modellere filmkondensering, helt specifikt kondensering af væske

fra gasfasen på en vertikal væg med væske løbende nedad. Den udviklede tilgang, som er kaldt den frie overflade entropisk gitter Boltzmann metode, er verificeret med sammenligninger af andre stadfæstede teoretiske og empiriske modeller.

Omdrejningspunktet for det sidste emne beskrevet i denne afhandling beskriver en tilgang til at bruge de udviklede klimatiske modeller til pålidelighedsvurdering. Simuleringerne er udført for en modelindkapsling med en relativ simpel geometri, hvor svigtkriteriet er sat til at være den relative luftfugtighed ved printpladens lokalitet. Modelleringen er foretaget ved at kombinere kontrolvolumen simulation af vanddampfordelingen med en Monte Carlo udtagningsmetoden. Denne del fremstiller dermed et eksempel på, hvordan man kan bruge de udviklede fysiske modeller til at lave pålidelighedsforudsigelser i relation til miljømæssige faktorer, såsom temperatur og luftfugtighed.

Contents

Thesis Details	xi
Preface	xiii
1 Introduction	1
2 Transport of diluted gases	3
2.1 The Boltzmann equation	3
2.1.1 Properties of the Boltzmann equation	8
2.1.2 Boltzmann’s H-theorem	10
2.2 From Boltzmann to Navier-Stokes equations	12
2.3 Diffusion in monatomic gas mixtures	13
3 Evaporation at liquid-vapor interfaces	17
3.1 Hertz-Knudsen evaporation flux	18
3.1.1 Coefficients of evaporation and condensation	19
3.2 Non-equilibrium thermodynamics	20
3.3 Statistical rate theory	22
3.3.1 Calculation of entropy change	24
3.3.2 Equilibrium exchange rate	25
4 Lattice Boltzmann method	29
4.1 The lattice Boltzmann equation	29
4.1.1 The choice of LB units	33
4.1.2 The LB algorithm	33
4.2 Entropic lattice Boltzmann method	34
4.3 Boundary conditions	35
4.4 Multiphase flow	37
4.4.1 Shan-Chen pseudo-potential method	37
4.4.2 Free surface framework	38
4.4.3 Entropic multiphase approach	39

5	The reliability concept	41
5.1	Failure rate	41
5.2	Probability of failure	42
5.3	Humidity-related reliability	43
6	Experimental setup and modeling methods	45
6.1	Overview of the simulations and experimental studies	45
6.2	Experimental equipment	46
6.3	Modeling approaches	48
6.3.1	Transport of water vapor as a diluted species in air	48
6.3.2	Free surface lattice Boltzmann modeling of condensation	51
6.3.3	Finite volume modeling of diffusion	53
7	Humidity and temperature evolution in AquaRIUM	57
7.1	Investigation of thermodiffusion of water vapor in air	57
7.2	Humidity distributions affected by presence of liquid water	60
7.3	Natural convection in the AquaRIUM	64
8	Free surface entropic lattice Boltzmann method	69
8.1	Fundamentals of film condensation	69
8.2	Simulation results	71
9	Humidity-related reliability assessment	77
10	Conclusions	81
I	Appendix	83
I.1	Clausius–Clapeyron relation	83
I.1.1	Origin of water vapor	83
I.1.2	Phase transition and stability	84
I.2	Nüsselt film condensation	86
	References	91
	References	91
	Acknowledgments	99
	Publications	101
A	Humidity distribution affected by freely exposed water surfaces: Simulations and experimental verification	103
B	Free surface entropic lattice Boltzmann simulations of film condensation on vertical hydrophilic plates	113

Contents

C	Humidity evolution (breathing effect) in enclosures with electronics	123
D	Modeling of humidity-related reliability in enclosures with electronics	131

Thesis Details

Thesis Title: Humidity and temperature prediction for reliability of electronics
Ph.D. Student: Morten Arnfeldt Hygum
Supervisor: Assoc. Prof. Vladimir N. Popok, Aalborg University

The thesis consist of the following published peer-reviewed journal papers:

- [A] Morten A. Hygum, Vladimir N. Popok, "Humidity distribution affected by freely exposed water surfaces: Simulations and experimental verification," *Physical Review E*, vol.90, no.013023, 2014.
- [B] Morten A. Hygum, Ilya V. Karlin, Vladimir N. Popok, "Free surface entropic lattice Boltzmann simulations of film condensation on vertical hydrophilic plates," *International Journal of Heat and Mass Transfer*, vol.87, pp. 576–582, 2015.

In addition, the following peer-reviewed conference papers have been accepted for publication:

- [C] Morten A. Hygum, Vladimir N. Popok, "Humidity evolution (breathing effect) in enclosures with electronics," *The IMAPS Nordic Annual Conference Proceedings*, 2015.
- [D] Morten A. Hygum, Vladimir N. Popok, "Modeling of humidity-related reliability in enclosures with electronics," *The IMAPS Nordic Annual Conference Proceedings*, 2015.

This thesis has been submitted for assessment in partial fulfillment of the PhD degree. The thesis is based on the submitted or published scientific papers which are listed above. Parts of the papers are used directly or indirectly in the extended summary of the thesis. As part of the assessment, co-author statements have been made available to the assessment committee and are also available at the Faculty. The thesis is not in its present form acceptable for open publication but only in limited and closed circulation as copyright may not be ensured.

Preface

This thesis finalizes my work done at the Department of Physics and Nanotechnology, Aalborg University, Denmark as a Ph.D. student. Throughout the period, spanning from August 2012 to September 2015, I have been under the supervision of Associate Professor Vladimir Popok. From October 2014 to December 2014 I had the pleasure of a research stay abroad in the group of Professor Ilya Karlin at the Department of Mechanical and Process Engineering, ETH Zurich, Switzerland.

My research concerns the aspect of humidity-related reliability for power electronic enclosures. It is a concatenation of fluid dynamic simulations, experiments verifying the models and reliability assessment. The thesis summarizes two published journal articles and two accepted conference papers. The publications are attached at end of the thesis.

Outline of the thesis

The thesis is divided into several parts. Chapter 1 is an introduction to the reliability issue of power electronics and provides a motivation for the the carried out research. Chapter 2 - 5 constitutes the theoretical part of the thesis. Chapter 2 presents the kinetic theory of diluted gases. This is a foundation for simulations of gas transport and the lattice Boltzmann modeling approach. Chapter 3 partly extends the field to systems with liquid-vapor interfaces. The remaining part of chapter 3 describes other popular methods to model liquid evaporation with linkage to paper A. The lattice Boltzmann method is introduced in chapter 4 which is connected to the developed free surface lattice Boltzmann model presented in paper B. A mathematical formulation of the reliability concept is given in chapter 5. This formulation is the starting point of the work presented in paper D.

In chapter 6 the experimental and modeling methodologies are presented. Chapter 7 gives an overview of main experimental and simulation results of a test enclosure called AquaRIUM. Chapter 8 briefly presents the developed free surface entropic lattice Boltzmann method used to model film condensa-

tion, describes advantages of the method and presents a couple of simulation examples utilizing this method. The material is based on paper B. Finally, an approach to provide reliability assessment using humidity transport modeling is given in chapter 9 which is based on paper D.

Morten Arnfeldt Hygum
Aalborg University, October 1, 2015

1. Introduction

Power electronics is crucial part in a wide range of applications covering automotive devices, power controllers and actuators as well as transformers and converters used in the systems of electricity production, distribution and consumption [1, 2]. Today, more than 40% of the total global energy is consumed in form of electricity. This number increases every year due to tendencies to use alternatives to fossil fuels in energy production [3]. Furthermore, the members of the EU have decided to increase the percentage of renewable energy and reduce CO₂ emissions by 20% by 2020 [4]. These statements signify the importance of reliable and efficient power electronic systems and components used in energy production and distribution [1, 2]. The reliability of a system is defined as the ability to perform under a set of conditions for a certain amount of time [5]. To get this knowledge one requires to test a significant number of devices until they fail. This approach allows to develop a statistical model for the life time. However, there are several reasons preventing to go in this direction. One of the reasons being that the expected life time of many power electronic systems is more than ten years and for high power modules more than thirty years [1]. To reduce the testing period the systems may be stressed under accelerated conditions from which the estimated life time can be extrapolated [6]. This approach has also been proven to be associated with difficulties. The accelerated failures may be due to a failure mechanism which will not be induced under normal operating conditions. Also, if the failure mechanism of interest is not due to wear-out or degradation and more like an on-off failure, it is difficult to accelerate. An example of this may be water condensation on a printed circuit board (PCB) causing an instant short circuit. Finally, the economical aspect of having to destroy enough products to obtain statistical evidence may be undesirable.

Nowadays, power electronics find applications in more and more harsh environments [7], the devices are used outdoor in a wide range of climatic conditions. Examples of such systems are converters of wind turbines placed offshore, controllers of water pumps, windows actuators and many others. Among the environmental factors humidity and temperature as well as re-

lated to them phenomenon of water condensation are significant stressors. With an average droplet formation size varying between 20-50 μm , depending on temperature and humidity level, the high-density packing on PCBs becomes an increased challenge. The smallness in component size makes it easier for a droplet to form a local electrochemical cell where the water layer connects two electric points and, thus, initiate a shortcut [8]. Corrosion becomes another important degradation mechanism especially for the devices with long life period [9, 10].

This project aims to address humidity-related reliability issues relevant for power electronic packaging. It is the goal to develop models and simulation approaches which can be used to predict local humidity and temperature in enclosures for power electronics. From this one also aims to gain physical understanding of processes and phenomena in order to improve the device reliability from the climatic point of view.

2. Transport of diluted gases

The theoretical part of the thesis is divided into three main chapters. This chapter is a general introduction to the classic kinetic theory of gases which makes a necessary foundation for the understanding of various transport mechanisms in gases. Also, the theory is one of the mile stones in the field of heat and mass transfer at liquid-vapor interfaces, which will be presented in chapter 3. Finally, it helps to have an understand of the kinetic theory for the so-called lattice Boltzmann method (LBE), an approach for simulating various kinds of transport, which will be described in chapter 4.

To address the humidity issue one can consider water molecules mixed with conventional air. One of the widely used ways to describe such system is to apply standard gas theories. The dominant theory of transport in diluted gases at the mesoscopic level is the kinetic theory. By averaging the properties of individual gas molecules the macroscopic properties of the system, like pressure, density, and temperature can be obtained. Since the gas kinetics theory is pretty wide topic, several key issues, which are especially important for the current work, are over viewed below using materials from [11] and [12].

2.1 The Boltzmann equation

In the field of kinetic theory of gases Ludwig Boltzmann derived a famous transport equation which later was named after him.

To derive the Boltzmann equation (BE) one needs to consider a monatomic gas of N identical molecules. Such a gas molecule is characterized by its position \vec{r} and velocity \vec{c}_1 which is combined for all the molecules constituting the phase space. The state of the gas is described by the distribution function

$$f(\vec{c}_1, \vec{r}, t), \quad (2.1)$$

which is the probability of having a molecule at the position \vec{r} with the velocity \vec{c}_1 at time t . Thus, the number of molecules dN_1 in a infinitesimal volume

of phase space is

$$dN_1 = f(\vec{c}_1, \vec{r}, t) d^3\vec{c}_1 d^3\vec{r}. \quad (2.2)$$

Now, it is assumed that the gas is diluted meaning that the molecules mostly experience free travels and collide from time to time. The gas is of so low density that simultaneous collisions of more than two molecules can be neglected. The analysis will be restricted to gas molecules modeled as hard spheres with a diameter σ . Furthermore, the system of interest is described with a volume $V \rightarrow \infty$ and the number of molecules $N \rightarrow \infty$. The average density of molecules is considered to be constant $N/V \sim \text{const}$ and the volume occupied by the molecules is negligible $N\sigma^3/V \rightarrow 0$. The molecules are, however, not so small that they do not interact, meaning $N\sigma^2 \sim \text{const}$. For such a system there are two mechanisms which may change the distribution function in time and space, namely free flight with possible influencing forces like gravity \vec{F} and binary collisions. Hence,

$$\frac{\partial f(\vec{c}_1, \vec{r}, t)}{\partial t} + \vec{c}_1 \cdot \frac{\partial f(\vec{c}_1, \vec{r}, t)}{\partial \vec{r}} + \frac{\vec{F}}{m} \cdot \frac{\partial f(\vec{c}_1, \vec{r}, t)}{\partial \vec{c}_1} = \left(\frac{\partial f(\vec{c}_1, \vec{r}, t)}{\partial t} \right)_{\text{coll}}, \quad (2.3)$$

where m is the mass of the gas molecules. The change in f due to collision $\left(\frac{\partial f}{\partial t} \right)_{\text{coll}}$ is only affected by short-range forces and will be instant in time. The right hand side is also referred to as the collision integral or operator. It can be written with a gain-loss formulation as follows:

$$\left(\frac{\partial f}{\partial t} \right)_{\text{coll}} = Q^+ - Q^-, \quad (2.4)$$

where $Q^+ d^3\vec{c}_1 d^3\vec{r} dt$ is the number of molecules of type "1" which has entered the elementary phase space volume $d^3\vec{c}_1 d^3\vec{r}$ due to collisions with other molecules in the time interval dt . $Q^- d^3\vec{c}_1 d^3\vec{r} dt$ is the loss of molecules of type "1" in the same elementary phase space volume also because of collisions with other molecules in that same time interval.

Before proceeding with the derivation of the Boltzmann equation, some dynamics of binary collisions need to be considered. As mentioned, the collision is instantaneous. The pre-collisional velocities are denoted by $\{\vec{c}_1, \vec{c}_2\}$, while $\{\vec{c}'_1, \vec{c}'_2\}$ refer to the post-collisional velocities, where the indexes 1 and 2 are introduced so that the molecules are distinguishable before and after the collision. Similarly, the center of mass velocity \vec{G} and relative velocity \vec{g} before the collision are given as

$$\vec{G} = \frac{\vec{c}_1 + \vec{c}_2}{2} \quad (2.5)$$

and

$$\vec{g} = \vec{c}_1 - \vec{c}_2. \quad (2.6)$$

2.1. The Boltzmann equation

For the velocities the notation ' refers to post-collision. Furthermore, $\vec{e} = \frac{\vec{g}}{g}$ is the unit vector in the direction of \vec{g} . Since the considered molecules have the same mass the conservation of momentum and energy dictates that

$$\vec{c}_1 + \vec{c}_2 = \vec{c}'_1 + \vec{c}'_2 \quad (2.7)$$

and

$$|\vec{c}_1|^2 + |\vec{c}_2|^2 = |\vec{c}'_1|^2 + |\vec{c}'_2|^2, \quad (2.8)$$

where fully elastic collisions have been assumed. From equation (2.7) it can be deduced that the center-of-mass is conserved during the collision

$$\vec{G} = \vec{G}', \quad (2.9)$$

while equation (2.8) infers that the magnitude of the relative velocity is also unchanged

$$g = g'. \quad (2.10)$$

The conservation laws reveal that the post-collision velocities can be written as

$$\vec{c}'_1 = \frac{\vec{c}_1 + \vec{c}_2}{2} - \frac{|\vec{c}_1 + \vec{c}_2|}{2} \vec{e}' \quad (2.11a)$$

$$\vec{c}'_2 = \frac{\vec{c}_1 + \vec{c}_2}{2} + \frac{|\vec{c}_1 + \vec{c}_2|}{2} \vec{e}', \quad (2.11b)$$

where the deflection angle θ is the angle between \vec{e} and \vec{e}' and it is obtained from

$$\cos \theta = \vec{e} \cdot \vec{e}'. \quad (2.12)$$

Now, consider an inlet jet where the interaction between the gas molecules is presumed to be through a central potential and, therefore, only depends on the distance between the molecules. In the center-of-mass frame the molecules move with the velocity \vec{g} and the reduced mass is $m_0 = m_1 m_2 / (m_1 + m_2) = m/2$. The impact factor b is as shown in figure 2.1. The azimuth angle ϵ then gives the orientation of the trajectory with respect to an arbitrary fixed plane containing the center of the force and parallel to \vec{g} . The area between two concentric circles, through which the jet passes, with the radii b and $b + db$, cut with the angle between ϵ and $\epsilon + d\epsilon$ can be written as

$$dA_{in} = b db d\epsilon. \quad (2.13)$$

The molecules traveling through dA_{in} become scattered into the solid angle

$$dA_{out} = d^2 \vec{e}' = \sin \theta d\theta d\epsilon. \quad (2.14)$$

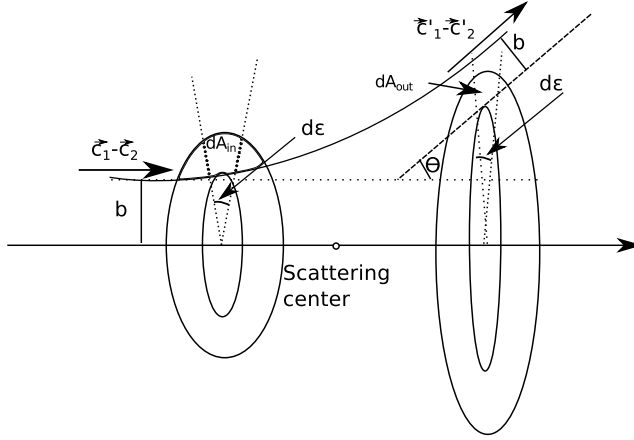


Fig. 2.1: Illustration of the scattering of two molecules.

The differential scattering cross section α_{12} is then defined as the ratio of the two areas

$$\alpha_{12} = \frac{dA_{in}}{dA_{out}} = \frac{bdbd\epsilon}{\sin \theta d\theta d\epsilon}. \quad (2.15)$$

or it can be written as

$$\alpha_{12} = b \left| \frac{\partial b / \partial \theta}{\sin \theta} \right|, \quad (2.16)$$

where the absolute value is introduced to ensure α_{12} to be a positive scalar. For repulsive forces the derivative of b parameter with respect to θ is negative.

The differential scattering cross section is a measure of the intensity of the incoming molecules through the cross section element in terms of the scattered molecules into the solid line. For molecules represented by hard spheres α_{12} can be found from geometric considerations:

$$\alpha_{12} = (\sigma/2)^2/4. \quad (2.17)$$

As mentioned, the rate of change in the distribution function can be written in the gain-loss formulation as indicated by equation (2.4). To evaluate these quantities the statistics of molecular collisions needs to be addressed. It is assumed that colliding molecules are completely uncorrelated. This is known as the molecular chaos assumption meaning that one can write number of colliding pairs as $dN_{12} = dN_1 dN_2$.

The amount of molecules of type "2" dN_2 which encounters number of type "1" molecules dN_1 can be written as

$$dN_2 = f(\vec{c}_2, \vec{r}, t) d^3 \vec{c}_2 (|\vec{c}_2 - \vec{c}_1| dt \times b db d\epsilon), \quad (2.18)$$

2.1. The Boltzmann equation

where $(|\vec{c}_2 - \vec{c}_1| dt \times b db d\epsilon)$ is the elementary collision volume. The number of colliding pairs is, thus, given as

$$dN_{12} = dN_1 dN_2 = f(\vec{c}_1, \vec{r}, t) d^3 \vec{c}_1 d^3 \vec{r} f(\vec{c}_2, \vec{r}, t) d^3 \vec{c}_2 (|\vec{c}_2 - \vec{c}_1| b db d\epsilon dt), \quad (2.19)$$

which can be rewritten using the differential cross section to

$$dN_{12} = \left(f(\vec{c}_1, \vec{r}, t) f(\vec{c}_2, \vec{r}, t) |\vec{c}_2 - \vec{c}_1| \alpha_{12} d^2 \vec{e}' d^3 \vec{c}_2 \right) d^3 \vec{c}_1 d^3 \vec{r} dt. \quad (2.20)$$

The counting of the gain is greatly simplified by reverse the scattering process in time. The collisions are described by Newtonian mechanics, which indeed is time reversal. Thus, the initial and final velocities due to a scattering process are reversible. This enables to write the number of pair collisions of the type $\{\vec{c}'_1, \vec{c}'_2\} \rightarrow \{\vec{c}_1, \vec{c}_2\}$ as

$$dN'_{12} = f(\vec{c}'_1, \vec{r}, t) f(\vec{c}'_2, \vec{r}, t) |\vec{c}'_2 - \vec{c}'_1| \alpha'_{12} d^2 \vec{e} d^3 \vec{c}'_2 d^3 \vec{c}'_1 d^3 \vec{r} dt. \quad (2.21)$$

Since the differential scattering cross section does not changed under the inversion of the velocities and the magnitude of the relative velocity remains unchanged one can write

$$dN'_{12} = f(\vec{c}'_1, \vec{r}, t) f(\vec{c}'_2, \vec{r}, t) |\vec{c}_2 - \vec{c}_1| \alpha_{12} d^2 \vec{e} d^3 \vec{c}'_2 d^3 \vec{c}'_1 d^3 \vec{r} dt. \quad (2.22)$$

Now, the elementary volume $d^2 \vec{e} d^3 \vec{c}'_2 d^3 \vec{c}'_1$ will be transformed into $d^2 \vec{e}' d^3 \vec{c}_2 d^3 \vec{c}_1$ by evaluating the following Jacobian:

$$J = \frac{\partial(\vec{G}, \vec{g}_{21})}{\partial(\vec{c}_1, \vec{c}_2)} = 1. \quad (2.23)$$

Hence,

$$d^3 \vec{G} d^3 \vec{g}_{21} = |J| d^3 \vec{c}_1 d^3 \vec{c}_2 = d^3 \vec{c}_1 d^3 \vec{c}_2. \quad (2.24)$$

Likewise, it can be obtained that

$$d^3 \vec{G} d^3 \vec{g}'_{21} = d^3 \vec{c}'_1 d^3 \vec{c}'_2. \quad (2.25)$$

With $d^3 \vec{g}_{21} = g_{21}^2 d^2 \vec{g}_{21} d^3 \vec{e}$ and $d^3 \vec{g}'_{21} = g_{21}^2 d^2 \vec{g}_{21} d^3 \vec{e}'$ it can be found that

$$d^2 \vec{e} d^3 \vec{c}_2 d^3 \vec{c}_1 = d^2 \vec{e}' d^3 \vec{c}_2 d^3 \vec{c}_1, \quad (2.26)$$

which gives rise to

$$dN'_{12} = \left(f(\vec{c}'_1, \vec{r}, t) f(\vec{c}'_2, \vec{r}, t) |\vec{c}_2 - \vec{c}_1| \alpha_{12} d^2 \vec{e}' d^3 \vec{c}_2 \right) d^3 \vec{c}_1 d^3 \vec{r} dt. \quad (2.27)$$

The rate of loss and gain can, respectively, be written as following:

$$Q^- = f(\vec{c}_1, \vec{r}, t) \int_{\mathbb{R}^3} \int_{S^2} f(\vec{c}_2, \vec{r}, t) |\vec{c}_2 - \vec{c}_1| \alpha_{12} d^2 \vec{e}' d^3 \vec{c}_2 \quad (2.28a)$$

$$Q^+ = \int_{\mathbb{R}^3} \int_{S^2} f(\vec{c}'_1, \vec{r}, t) f(\vec{c}'_2, \vec{r}, t) |\vec{c}_2 - \vec{c}_1| \alpha_{12} d^2 \vec{e}' d^3 \vec{c}_2. \quad (2.28b)$$

with \mathbb{R}^3 to be the real space and S^2 to be the 2-sphere space. The rate of change in the one-particle distribution can, thus, be written as

$$\left(\frac{\partial f}{\partial t}\right)_{coll} = \int_{\mathbb{R}^3} \int_{S^2} [f'_1 f'_2 - f_1 f_2] |\vec{c}_2 - \vec{c}_1| \alpha_{12} d^2 \vec{c}' d^3 \vec{c}_2, \quad (2.29)$$

where the notation $f(\vec{c}'_1, \vec{r}, t)$ has been changed to f'_1 . Similarly $f(\vec{c}_1, \vec{r}, t)$ has been changed to f_1 , $f(\vec{c}'_2, \vec{r}, t)$ has been changed to f'_2 , and $f(\vec{c}_2, \vec{r}, t)$ has been changed to f_2 . Equation (2.29) is the famous Boltzmann Stosszahlansatz (collision number hypothesis) also known as the Boltzmann collision integral or operator. With this the Boltzmann transport equation is derived as

$$\frac{\partial f_1}{\partial t} + \vec{c}_1 \cdot \frac{\partial f_1}{\partial \vec{r}} + \vec{F} \cdot \frac{\partial f_1}{\partial \vec{c}_1} = \int_{\mathbb{R}^3} \int_{S^2} [f'_1 f'_2 - f_1 f_2] |\vec{c}_2 - \vec{c}_1| \alpha_{12} d^2 \vec{c}' d^3 \vec{c}_2, \quad (2.30)$$

which is a complicated non-linear integro-differential equation. It describes the change in the distribution function by two processes: streaming and colliding.

2.1.1 Properties of the Boltzmann equation

As mentioned above, the Boltzmann equation is a transport equation which can be used to describe molecular properties. Let's consider a molecular property of a general form $\psi(\vec{c})$. The macroscopic property associated with the microscopic one is obtained by averaging over the velocity space. Thus, the macroscopic density $\rho(\vec{r}, t)_{\psi(\vec{c})}$ for the $\psi(\vec{c})$ property is obtained from

$$\rho(\vec{r}, t)_{\psi} = \int_{\mathbb{R}^3} \psi(\vec{c}) f(\vec{c}, \vec{r}, t) d^3 \vec{c}. \quad (2.31)$$

The flux of the microscopic property can be defined as $\vec{j}_{\psi} = \psi(\vec{c}) \vec{c}$, which gives rise to the following macroscopic flux :

$$\vec{j}(\vec{r}, t)_{\psi} = \int_{\mathbb{R}^3} \vec{c} \psi(\vec{c}) f(\vec{c}, \vec{r}, t) d^3 \vec{c}. \quad (2.32)$$

Introducing the collision kernel as

$$B = |\vec{c}_2 - \vec{c}_1| \alpha_{12} \quad (2.33)$$

and, for simplicity, omitting the force term allows to write the transport equation for any macroscopic density as

$$\frac{\partial \rho_{\psi}}{\partial t} + \nabla \cdot \vec{j}_{\psi} = \int_{\mathbb{R}^3} \int_{\mathbb{R}^3} \int_{S^2} \psi_1 [f'_1 f'_2 - f_1 f_2] B d^2 \vec{c}' d^3 \vec{c}_2 d^3 \vec{c}_1. \quad (2.34)$$

2.1. The Boltzmann equation

The rate due to collisions is, thereby, given as

$$R_\psi = \int_{\mathbb{R}^3} \int_{\mathbb{R}^3} \int_{\mathbb{S}^2} \psi_1 [f'_1 f'_2 - f_1 f_2] B d^2 \vec{e}' d^3 \vec{c}_2 d^3 \vec{c}_1 \quad (2.35a)$$

$$= \int_{\mathbb{R}^3} \int_{\mathbb{R}^3} \int_{\mathbb{S}^2} \psi_2 [f'_1 f'_2 - f_1 f_2] B d^2 \vec{e}' d^3 \vec{c}_2 d^3 \vec{c}_1 \quad (2.35b)$$

$$= - \int_{\mathbb{R}^3} \int_{\mathbb{R}^3} \int_{\mathbb{S}^2} \psi'_1 [f'_1 f'_2 - f_1 f_2] B d^2 \vec{e}' d^3 \vec{c}_2 d^3 \vec{c}_1 \quad (2.35c)$$

$$= - \int_{\mathbb{R}^3} \int_{\mathbb{R}^3} \int_{\mathbb{S}^2} \psi'_2 [f'_1 f'_2 - f_1 f_2] B d^2 \vec{e}' d^3 \vec{c}_2 d^3 \vec{c}_1 \quad (2.35d)$$

as a consequence of time invariance and renaming of the molecules. Therefore,

$$R_\psi = \frac{1}{4} \int_{\mathbb{R}^3} \int_{\mathbb{R}^3} \int_{\mathbb{S}^2} (\psi_1 + \psi_2 - \psi'_1 - \psi'_2) [f'_1 f'_2 - f_1 f_2] B d^2 \vec{e}' d^3 \vec{c}_2 d^3 \vec{c}_1. \quad (2.36)$$

The molecular properties $m, m\vec{c}$ and $mc^2/2$, thus, correspond to

$$\rho(\vec{r}, t) = m \int_{\mathbb{R}^3} f(\vec{r}, \vec{c}, t) d^3 \vec{c} \quad (2.37a)$$

$$\rho(\vec{r}, t) \vec{u}(\vec{r}, t) = m \int_{\mathbb{R}^3} \vec{c} f(\vec{r}, \vec{c}, t) d^3 \vec{c} \quad (2.37b)$$

$$E(\vec{r}, t) = m/2 \int_{\mathbb{R}^3} c^2 f(\vec{r}, \vec{c}, t) d^3 \vec{c}, \quad (2.37c)$$

respectively. \vec{u} is the macroscopic velocity, not to be confused with \vec{c} , and E is the energy. These properties are also called the moments of $f(\vec{r}, \vec{c}, t)$. Since pair collisions conserve the number of molecules, the momentum and the energy of the molecules, the following applies

$$\psi_1 + \psi_2 - \psi'_1 - \psi'_2 = 0 \quad (2.38)$$

for $\psi = m, m\vec{c}, mc^2/2$. The direct implication of this is the following transport equations for the locally conserved properties:

$$\frac{\partial \rho}{\partial t} + \nabla \cdot (\rho \vec{u}) = 0, \quad (2.39a)$$

$$\frac{\partial (\rho \vec{u})}{\partial t} + \nabla \cdot \mathbf{P} = 0, \quad (2.39b)$$

$$\frac{\partial E}{\partial t} + \nabla \cdot \vec{q} = 0, \quad (2.39c)$$

where \mathbf{P} is the pressure tensor, and \vec{q} is the energy flux. They can be written as

$$\mathbf{P}(\vec{r}, t) = m \int_{\mathbb{R}^3} \vec{c} \vec{c} f(\vec{r}, \vec{c}, t) d^3 \vec{c} \quad (2.40)$$

and

$$\vec{q}(\vec{r}, t) = m/2 \int_{\mathbb{R}^3} c^2 \vec{c} f(\vec{r}, \vec{c}, t) d^3 \vec{c}. \quad (2.41)$$

Now, with appropriate boundary conditions the mass, momentum and energy are likewise globally conserved. With the derived transport equation for the conserved macroscopic properties we now turn to a special property described below.

2.1.2 Boltzmann's H-theorem

A special molecular property

$$\psi = \ln f + 1, \quad (2.42)$$

is associated with the following rate

$$\begin{aligned} R_{\ln f+1} &= \frac{1}{4} \int_{\mathbb{R}^3} \int_{\mathbb{R}^3} \int_{S^2} (\ln f_1 + \ln f_2 - \ln f'_1 - \ln f'_2) [f'_1 f'_2 - f_1 f_2] B d^2 \vec{e}' d^3 \vec{c}_2 d^3 \vec{c}_1 \\ &= \frac{1}{4} \int_{\mathbb{R}^3} \int_{\mathbb{R}^3} \int_{S^2} \ln \frac{f_1 f_2}{f'_1 f'_2} [f'_1 f'_2 - f_1 f_2] B d^2 \vec{e}' d^3 \vec{c}_2 d^3 \vec{c}_1 \end{aligned} \quad (2.43)$$

From equation (2.43) it is seen that the rate $R_{\ln f+1}$ is non-positive

$$R_{\ln f+1} \leq 0 \quad (2.44)$$

for any f . By investigating the time derivative of the so-called Boltzmann H-function

$$\frac{\partial H}{\partial t} = \int_{\mathbb{R}^3} \frac{\partial}{\partial t} (f \ln f) d^3 \vec{c} = \int_{\mathbb{R}^3} (\ln f + 1) \frac{\partial f}{\partial t} d^3 \vec{c} = R_{\ln f+1} \quad (2.45)$$

one arrives at the H-theorem. Due to the Boltzmann equation, the H-function never increases. As will be shown later, one can relate the H-function to entropy known from the second principle of thermodynamics. Again, with suitable boundary conditions it is possible to reach the same non-increasing conclusion for the space-dependent H-function $H_{tot} = \int \int f \ln f d^3 \vec{c} d^3 \vec{r}$ [11]. It can be shown that H is bound since $\int f \ln f d^3 \vec{c}$ does not diverge [11]. It goes to a limit in which $\partial H / \partial t = 0$. According to equation (2.45) this occurs if and only if

$$f_1^{eq} f_2^{eq} = f_1^{eq'} f_2^{eq'} \quad (2.46)$$

or, equivalently,

$$\ln f_1^{eq} + \ln f_2^{eq} - \ln f_1^{eq'} - \ln f_2^{eq'} = 0, \quad (2.47)$$

where the notation eq indicates that the gas is at equilibrium. From equation (2.47) it can be concluded that logarithm of f^{eq} must be a linear combination

2.1. The Boltzmann equation

of the local conserved microscopic properties and following equation can be introduced:

$$\ln f^{eq} = a + \vec{b} \cdot m\vec{c} + w \frac{mc^2}{2}. \quad (2.48)$$

Since these five parameters are arbitrary it is possible to write

$$f^{eq} = A e^{-\frac{(\vec{c}-\vec{a})^2}{2\beta}}. \quad (2.49)$$

Combining equation (2.49) with (2.39a)-(2.39c) and the Maxwell-Boltzmann distribution function with $E = \frac{3\rho k_B T}{2m} + \frac{\rho u^2}{2}$ leads to

$$f^{eq} = n \left(\frac{2\pi k_B T}{m} \right)^{3/2} e^{-\frac{(\vec{c}-\vec{u})^2}{2k_B T}}, \quad (2.50)$$

where T is temperature, k_B is Boltzmann's constant and $n = \rho/m$ is the number density. The Maxwell-Boltzmann distribution annuls the collision integral. Since ρ , T and \vec{u} are space dependent variables, equation (2.49) is a local equilibrium distribution function, which only annuls the right-hand side of the Boltzmann equation. Hence, it is not a solution to the Boltzmann equation. However, if ρ , T and \vec{u} are space independent variables, the Maxwell-Boltzmann distribution becomes a solution and, thereby, a global equilibrium or simply equilibrium. The maxwellian is sometimes expressed with the peculiar velocity $\vec{C} = \vec{c} - \vec{u}$.

The H-function at equilibrium can be obtained as following:

$$H^{eq}(f^{eq}) = n \ln n + \frac{3n}{2} \ln \left(\frac{m}{2\pi k_B T} \right) - \frac{3n}{2}, \quad (2.51)$$

with M being the total mass of the gas. The total H -function is found by evaluating the following volume integral:

$$H_{tot}^{eq} = \int H^{eq} d^3\vec{r} = \frac{M}{m} \left(\ln n + \frac{3}{2} \ln \left(\frac{m}{2\pi k_B T} \right) - \frac{3}{2} \right). \quad (2.52)$$

The entropy of an ideal gas S_{tot} is [11]

$$S_{tot} = \frac{Mk_B}{m} \ln(T^{3/2}/n) + \frac{M}{m} \text{const.} \quad (2.53)$$

Thus, except for an additive constant, the entropy is related to the H-function through

$$S_{tot} = -k_B H_{tot}^{eq} \quad (2.54)$$

when the gas is in a uniform steady state. For non-uniform or non-steady states the concept of entropy can be generalized with equation (2.54) [11]. A discussion of this is, however, beyond the scope of this work.

This section finalizes the gas properties which can be obtained from the BE without solving it. Below, a method for solving the BE is discussed and some transport mechanisms which arise from this equation are presented.

2.2 From Boltzmann to Navier-Stokes equations

For certain systems, representing the hydrodynamic limit, it is possible to show that the governing equations of continuum mechanics, also known as the Navier-Stokes (NS) equations, arise from the Boltzmann transport equation. These systems will be specified below. However, it is worth mentioning that a full rigorous connection from the kinetic theory to continuum mechanics has not been made. This problem is known as Hilbert's 6th problem [13]. The analysis will not be done in detail. Only the main steps in deriving the continuum equations from the BE will be mentioned.

The BE is first rewritten to a non-dimensional equation while the hydrodynamic arises from an expansion of the non-dimensional equation. This is known as the Chapman-Enskog method [11, 12].

The thermal speed of an atom or molecule can be introduced as

$$v_T = \sqrt{\frac{2k_B T}{m}}, \quad (2.55)$$

which enables to write the Maxwell-Boltzmann distribution as $f^{eq} = \pi^{-3/2} n v_T^{-3/2} e^{-(C/v_T)^2}$. The mean free path of molecules (between two sequential collisions), L_{mfp} can be shown to be $L_{mfp} = (\sqrt{2}n\sigma)^{-1}$ for hard spheres [11] with σ as the diameter. Introducing the reduced time $t^* = t/\bar{t}$ and space $\vec{r}^* = \vec{r}/L$ with \bar{t} as the characteristic time and L as the characteristic length of the system, the BE can be rewritten as

$$\left(\frac{L}{\bar{t}v_T}\right) \frac{\partial f_1^*}{\partial t^*} + \vec{c}_1^* \cdot \frac{\partial f_1^*}{\partial \vec{r}^*} = \left(\frac{L}{L_{mfp}}\right) \int_{\mathbb{R}^3} \int_{\mathbb{S}^2} [f_1'^* f_2'^* - f_1^* f_2^*] B^* d^2 \vec{e}^* d^3 \vec{c}_2^*, \quad (2.56)$$

where the reduced scattering kernel $B^* = \frac{B}{\sigma^2 v_T}$, velocity $\vec{c}^* = \vec{c}/v_T$ and distributions $f^* = f/f_c$ are introduced. The characteristic distribution $f_c = n/v_T^3$. To classify different systems the Strouhal St and Knudsen Kn numbers are used. They are defined as

$$St = \left(\frac{L}{\bar{t}v_T}\right), \quad Kn = \left(\frac{L_{mfp}}{L}\right), \quad (2.57)$$

which gives rise to

$$St \frac{\partial f_1^*}{\partial t^*} + \vec{c}_1^* \cdot \frac{\partial f_1^*}{\partial \vec{r}^*} = \left(\frac{1}{Kn}\right) \int_{\mathbb{R}^3} \int_{\mathbb{S}^2} [f_1'^* f_2'^* - f_1^* f_2^*] B^* d^2 \vec{e}^* d^3 \vec{c}_2^*. \quad (2.58)$$

The hydrodynamics limit is characterized by small Knudsen numbers $Kn \rightarrow 0$. Depending on the size of St different aspects of the continuum mechanics,

2.3. Diffusion in monatomic gas mixtures

compressible or incompressible, arise from the BE. In particular, for small Strouhal, Knudsen, and March Ma numbers

$$St \sim Kn \sim Ma \ll 1,$$

the incompressible Navier-Stokes equations can be obtained from the BE. $Ma = u/c_s$ with c_s to be the speed of sound. In the method of Chapman and Enskog, the distribution function f is expanded in power series of a parameter ϵ . The ϵ parameter is in the order of the Knudsen number and the series expansion is expressed as

$$f = f^{(0)} + \epsilon f^{(1)} + \epsilon^2 f^{(2)} + \dots = \sum_{r=0}^{\infty} \epsilon^r f^{(r)}. \quad (2.59)$$

with $f^{(0)}$ as the first order expansion, $f^{(1)}$ as the second order expansion, $f^{(2)}$ as the third order expansion and so on.

As mentioned, the full Chapman–Enskog analysis is cumbersome and will not be done here. For more details, see the references [11–13]. The incompressible NS equations are given as

$$\begin{aligned} \nabla \vec{u} &= 0, \\ \frac{\partial u}{\partial t} + (\vec{u} \cdot \nabla) \vec{u} + \nabla p &= \nu \nabla^2 \vec{u}, \end{aligned} \quad (2.60)$$

where the kinematic viscosity for hard spheres can be shown to be [11]

$$\nu = \frac{5}{16\sigma^2} \left(\frac{k_B m T}{\pi} \right)^{1/2} \quad (2.61)$$

For certain systems the BE can be shown to be associated with the macroscopic equations of fluid mechanics. One of the biggest accomplishments of Chapman and Enskog was, however, the theoretical foundation of thermodiffusion in gases discussed below.

2.3 Diffusion in monatomic gas mixtures

It is common practice in the field of computational fluid dynamics (CFD) to address air as a monatomic gas [14]. The water molecules can be approximated as hard spheres with a radius $\sigma_{H_2O} = 2.7\text{\AA}$ and $m_{H_2O} = 18\text{u}$ [15]. For air $\sigma_{air} = 3.75\text{\AA}$ and $m_{air} = 28.85\text{u}$ [11]. This allows for a significant simplification of the modeling.

In a gas mixture, e.g. constituting of two gases, molecules diffuse relative to each other and the following equation can be introduced

$$\vec{C}_1 - \vec{C}_2 = \frac{1}{n_1} \int \vec{C}_1 f_1 d\vec{c}_1 - \frac{1}{n_2} \int \vec{C}_2 f_2 d\vec{c}_2 \neq 0, \quad (2.62)$$

where $\overline{\vec{C}}_1$ denotes the mean of the peculiar velocity of the type "1" gas and $\overline{\vec{C}}_2$ is the same quantity for gas "2". It can be shown that equation (2.62) can be put in the form [11]

$$\overline{\vec{C}}_1 - \overline{\vec{C}}_2 = -\frac{1}{x_1 x_2} D_{12} \left(\nabla x_1 + k_T \nabla \ln T + \frac{n_1 n_2 (m_2 - m_1)}{n p} \nabla \ln p \right) \quad (2.63)$$

where $n = n_1 + n_2$, $x_i = n_i/n = p_i/(p_1 + p_2)$ and p_i is the partial pressure of the i 'th gas, D_{12} is the diffusion coefficient and k_T is the thermal-diffusion ratio given as $k_T = D_T/D_{12}$ with D_T to be the thermal-diffusion coefficient. Diffusive mass transfer can happen due to several types of gradients with one of them being the number density ∇x_1 . This is known as Fickian diffusion [16–18]. The diffusion due to pressure gradient $\nabla \ln p$, also referred to as baro-diffusion or pressure diffusion, is negligible when $\Delta p/p \ll 1$ [19]. It will, therefore, not be considered here. Finally, the thermal diffusion or thermo-diffusion due to $\nabla \ln T$ will dominate over baro-diffusion when $\Delta p/p < \Delta T/T$ but in most of the cases where $\Delta x_1/x_1 \gg \Delta T/T \gg \Delta p/p$, the Fickian diffusion usually is the only diffusion mechanism that needs to be considered.

If hard spheres are assumed, the binary diffusion coefficient can be obtained with a first order approximation [11]

$$D_{12} = \frac{3}{8n\sigma_{12}^2} \sqrt{\frac{k_B T}{2\pi}} \left(\frac{1}{m_1} + \frac{1}{m_2} \right) \quad (2.64)$$

where $\sigma_{12} = (\sigma_1 + \sigma_2)/2$.

The thermal diffusion ratio k_T can be shown to be [12, 19]

$$k_T = \frac{5C x_1 x_2}{x_1^2 Q_1 + x_2^2 Q_2 + x_1 x_2 Q_{12}} (x_1 S_1 - x_2 S_2), \quad (2.65)$$

with the coefficients for hard spheres given as

$$\begin{aligned} C &= \frac{1}{5}, & Q_1 &= \frac{m_1}{m_1 + m_2} E_1 (m_1^2 (5 - 4B) + 8A m_1 m_2 + 6m_2^2), \\ A &= \frac{2}{5}, & B &= \frac{3}{5}, & Q_{12} &= 3(m_1^2 + m_2^2) + 4m_1 m_2 A (11 - 4B) + 2m_1 m_2 E_1 E_2, \\ S_1 &= m_1^2 E_1 - 3m_2(m_2 - m_1) + 4m_1 m_2 A, & E_1 &= \frac{2}{5m_1} \sqrt{\frac{2}{m_2}} (m_1 + m_2)^{3/2} \frac{\sigma_{11}^2}{\sigma_{12}^2} \end{aligned}$$

where the expressions for S_2 , Q_2 and E_2 are obtained by interchanging the subscripts.

It is noticed that for the hard sphere model k_T is independent of T but it is dependent on the ratio of the mixture n_1/n_2 . For water vapor in air

2.3. Diffusion in monatomic gas mixtures

$k_T \sim -0.005$, from which it is seen that thermal diffusion tends to "push" the lighter water molecules towards the hotter regions and the heavier molecules towards the cooler regions. This coincides with the observations done for thermal diffusion [11].

3. Evaporation at liquid-vapor interfaces

At liquid-vapor interfaces molecules can be emitted from the liquid to the gas phase or incident molecules from the vapor can collide with the liquid phase, either to be absorbed and condensed or reflected and return to the vapor. Condensing and evaporating molecules are not necessarily characterized by the same velocity distribution function and temperature jumps can, therefore, occur at the interface [20]. Incident molecules condensing on the liquid surface are characterized by the vapor pressure p_v and temperature T_v of the vapor. Likewise, the evaporating molecules are described by an evaporation pressure p_{evap} and the temperature of the liquid T_l . The system under study is shown in figure 3.1 with the velocity distribution for the condensing molecules $f_v(p_v, T_v)$ and evaporating molecules $f_l(p_{evap}, T_l)$.

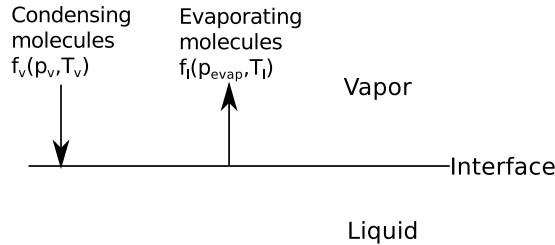


Fig. 3.1: Schematic of the evaporation and condensation velocity distribution functions.

In this work only semi-infinite interfaces are considered. Furthermore, effects of the Knudsen layer will be discarded. The Knudsen layer is a thin layer near a liquid or solid where the different molecular streams collide with each other. Due to the colliding streams the distribution functions may affect each other. The thickness of the Knudsen layer is in the order of a few mean free paths [21] and the effect of the layer is negligible for systems with small Knudsen numbers $Kn \rightarrow 0$. An illustration of the Knudsen layer is shown in figure 3.2.

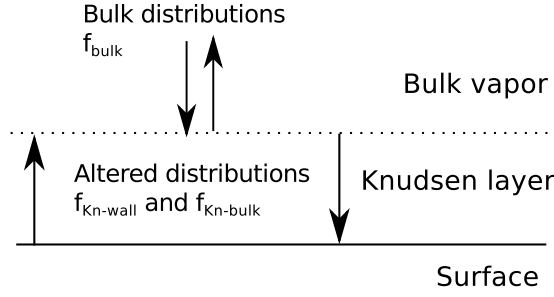


Fig. 3.2: Schematic of the Knudsen layer at a surface.

Nearly two decades ago an important observation was carried out for evaporation and condensation at water surfaces by Ward and Fang [22–25]. A considerable temperature jump at the surface, in the order of a few degree K , was observed. To explain this a new expression for the mass flux at a water surface was developed using statistical rate theory (SRT) [22–25]. These scientific contribution triggered new interest in the field and it is applied to model water-vapor interfaces in various domains, see e.g. [26].

The chapter serves to introduce different approaches to model the mass flux at a planar liquid-vapor interface as shown in figure 3.1. The classic kinetic theories pioneered by Hertz and Knudsen will first be reviewed. This will be followed by a phenomenological introduction to a non-equilibrium thermodynamical description of evaporation and condensation. Finally, SRT will be described and an expression for mass fluxes at water surfaces will be derived.

3.1 Hertz-Knudsen evaporation flux

Hertz [27] and Knudsen [28] (HK) made pioneering contributions within this field. They derived a simple one-dimensional expression for the mass flux at a liquid-vapor interface based on kinetic theory.

The HK expression is obtained by assuming that the liquid-vapor interface is close to equilibrium so the condensing and evaporating streams follow a Maxwell-Boltzmann distribution with $\vec{u} = \vec{0}$. This allows the mass flux integral to be split into two half-range Maxwellians:

$$j_{HK} = \iiint_{c_y > 0} mc_y f_l(p_{evap}, T_l) d^3\vec{c} + \iiint_{c_y < 0} mc_y f_v(p_v, T_v) d^3\vec{c}, \quad (3.1)$$

with c_y being the velocity component perpendicular to the surface. Conducting the integrals leaves the mass flux as

$$j_{HK} = \sqrt{\frac{m}{2\pi k_B}} \left(\frac{p_{evap}}{\sqrt{T_l}} - \frac{p_v}{\sqrt{T_v}} \right). \quad (3.2)$$

3.1. Hertz-Knudsen evaporation flux

At equilibrium there is no net flux, the temperature across the interface is constant and the pressure is equal to the saturated vapor pressure $p_{sat}(T)$. Hence, close to equilibrium the pressure of the evaporating molecules is approximately the saturated vapor pressure allowing for

$$j_{HK} = \sqrt{\frac{m}{2\pi k_B}} \left(\frac{p_{sat}}{\sqrt{T_l}} - \frac{p_v}{\sqrt{T_v}} \right). \quad (3.3)$$

An expression for the saturated vapor, usually described by the Clausius–Clapeyron relation, is reviewed in appendix I.1. It must be noted that one major assumption in deriving the HK expression is that the evaporation and condensation are uncoupled and justified by the diluteness of the gas.

3.1.1 Coefficients of evaporation and condensation

It is worth noting that in derivation of the HK mass flux it is assumed that all incident molecules from vapor colliding with the interface condensate and all liquid molecules at interface evaporate staying then in the vapor. To account for this the condensation η_{con} and evaporation η_{ev} coefficients are introduced. The definition of the condensation coefficient is the ratio of incident molecules that condense on the interface in terms of the number of molecules that collide with the interface [29]. Hence, if $\eta_{con} = 1$ all incident molecules will condense while if no condensation occurs $\eta_{con} = 0$.

The definition of the evaporation coefficient is not so straight forward. The evaporation coefficient η_{ev} can be defined to determine the magnitude of the distribution of the evaporating molecules, which is assumed to be a Maxwellian: $f_{ev} = \eta_{ev} f_M(p_{evap}, T_l, \vec{u})$ [29, 30]. Note, that the coefficients are not necessary constants. With the assumption that the reflected molecules do not affect the incident molecules the generalized HK formula is given as

$$j_{HK} = \sqrt{\frac{m}{2\pi k_B}} \left(\frac{\eta_{ev} p_{sat}}{\sqrt{T_l}} - \frac{\eta_{con} p_v}{\sqrt{T_v}} \right). \quad (3.4)$$

There is still a debate in the literature concerning η_{con} and η_{ev} and, for example, the values of the coefficients for water vary in the range 0.01-1.00 [31, 32]. However, since at equilibrium $j = 0$, $T_v = T_l$ and $p_v = p_{sat}$, it is agreed that $\eta_{con} = \eta_{ev}$ at equilibrium.

Small bulk velocities of the vapor can be taken into account in the Maxwellian distributions in equation (3.1) by which the Hertz–Knudsen–Schrage equation [20] also called Kucherov–Rikenglaz equation [33] is obtained:

$$j_{HKS} = \frac{2}{2 - \eta_{con}} \sqrt{\frac{m}{2\pi k_B}} \left(\frac{\eta_{ev} p_{sat}}{\sqrt{T_l}} - \frac{\eta_{con} p_v}{\sqrt{T_v}} \right). \quad (3.5)$$

There has also been efforts to get j_{HKS} which includes effects from the Knudsen layer [34]. It has, however, been reported that the so-called Schrage velocity distribution does not conserve momentum and energy [30]. In addition,

perturbation approaches such as the Chapman-Enskog method have been adapted to evaluate the distribution functions enabling, in principle, a full kinetic theory for the evaporation and condensation [29].

For theoretical insights in the evaporation and condensation coefficients one can look into molecular dynamics (MD) simulations [35, 36], which deal with this problem at the fundamentals. For computational simplicity argon is often simulated [37–39] with this approach. As mentioned, the coefficients are still debated in the literature and, thus, also subject of research until today.

The Hertz–Knudsen–Schrage equation finalizes the overview of the kinetic theory applied to the liquid-vapor interface. As shown in the section below, the kinetic theory can also be used in combination with thermodynamics to derive expression for heat and mass transfer across the interface.

3.2 Non-equilibrium thermodynamics

To complete the description of theoretical approaches, the concepts of non-equilibrium thermodynamics (NET) for prediction of mass and heat fluxes at a water-vapor interface are reviewed below. NET is sometimes also referred to as irreversible thermodynamics [29].

One of the advantages of NET is that it is not limited to dilute monatomic gases compared to the kinetic theory [40–42]. In NET the second law of thermodynamics is written in terms of local entropy production under the assumption of local equilibrium. This entropy production is, thus, written as the product sum of conjugated fluxes J_i and forces X_i in the system:

$$ds = \sum_i J_i X_i \geq 0, \quad (3.6)$$

The fluxes are obtained from a linear combination of the forces, hence

$$J_i = \sum_j L_{ij} X_j. \quad (3.7)$$

Equation (3.7) describes the fluxes as linear functions of forces with L_{ij} to be phenomenological coefficients. A famous example of this is Fourier’s law of heat conduction, where the heat flux is described by the thermal conductivity and a temperature gradient as driving force. The coefficients must follow the so-called Onsager relation, which states that $L_{ij} = L_{ji}$ [43].

A full set of independent extensive variables A_i is needed to predict the fluxes and forces with

$$J_i = \frac{\partial A_i}{\partial t} \quad (3.8)$$

and

$$X_i = \frac{\partial s}{\partial A_i}. \quad (3.9)$$

3.2. Non-equilibrium thermodynamics

It worth noting that there is no unique choice of fluxes and forces.

With NET an expression for the entropy production rate at the water-vapor interface, in units of surface area, for a one-component system can be derived [44, 45]:

$$ds = J_q^v \Delta(1/T) - J \frac{1}{T} \Delta\mu(T^l), \quad (3.10)$$

with J_q^v representing the measurable heat flux from the vapor into the surface, μ as the chemical potential and J to be the mass flux through the surface. Energy conservation dictates that the magnitude of the energy flux is given as

$$J_E = J_q^v + H_v J = J_q^l + H_l J, \quad (3.11)$$

where H_l and H_v are the enthalpy of the liquid and vapor, respectively. The thermal driving force is

$$X_q = \Delta(1/T) = \frac{1}{T_l} - \frac{1}{T_v} \quad (3.12)$$

while the driving force due to the chemical potential

$$X_\mu^v = -\frac{1}{T_l} \Delta\mu(T_l) = -\frac{1}{T_l} (\mu_l(T_l) - \mu_v(T_l)). \quad (3.13)$$

The linear relation between the driving forces and the heat and mass fluxes in the vapor can be written as

$$\nabla(1/T) = r_{qq}^v \vec{J}_q^v + r_{q\mu}^v \vec{J}, \quad (3.14a)$$

$$\frac{1}{T} \nabla\mu|_{T=const} = r_{\mu q}^v \vec{J}_q^v + r_{\mu\mu}^v \vec{J}, \quad (3.14b)$$

and similar expressions can be obtained for the liquid. The two main interface film resistivities, also called the film resistivities for the surface, are r_{qq}^v and $r_{\mu\mu}^v$. $r_{\mu q}^v$ and $r_{q\mu}^v$ are the cross interface film resistivities, which are equal due to the Onsager symmetry. The inversed quantities of the resistivities are referred to as conductivities. Kinetic theory has been used to derived thermodynamic forces in terms of the fluxes from which the resistivities can be found [44]

$$r_{qq}^{l,v}(T_s) = \frac{1.27640}{R(T_s)^2 c^8(T_s)} \sqrt{\frac{M}{3RT_s}}, \quad (3.15a)$$

$$r_{\mu\mu}^{l,v}(T_s) = r_{\mu q}^{l,v}(T_s) = \frac{0.54715}{T_s c^8(T_s)} \sqrt{\frac{M}{3RT_s}}, \quad (3.15b)$$

$$r_{\mu\mu}^{l,v}(T_s) = \frac{4.34161 R (\eta_c^{-1}(T_s) - 0.39856)}{c^8(T_s)} \sqrt{\frac{M}{3RT_s}}, \quad (3.15c)$$

where T_s is the temperature of the surface, M is the molar mass, R is the gas constant, $c^s(T_s)$ is the density of a vapor in coexistence with a liquid at the surface temperature and η_c is the condensation coefficient as described in the section earlier.

MD extensions of NET have also been formulated known as non-equilibrium molecular dynamics (NEMD), which e.g. have been used to verify the Onsager relation [46].

With the presented kinetic theory and the non-equilibrium thermodynamic models, one can now move towards a more quantum mechanical approach known as statistical rate theory which is described below. This section concludes this chapter.

3.3 Statistical rate theory

When studying liquid-vapor interfaces considerable temperature jumps for evaporating water surfaces were observed [22–25]. To understand this phenomenon, a new model was proposed using SRT [25]. This section aims to review the developed expression for the mass flux at the water-vapor interface. Throughout section 3.3 the material published in [25, 47] is used.

SRT concerns the concept of quantum mechanical transition probabilities applied to the theory of kinetics. For deriving the expression for the evaporation, consider a C-component system in which evaporation occurs in steady-state, illustrated in figure 3.3.

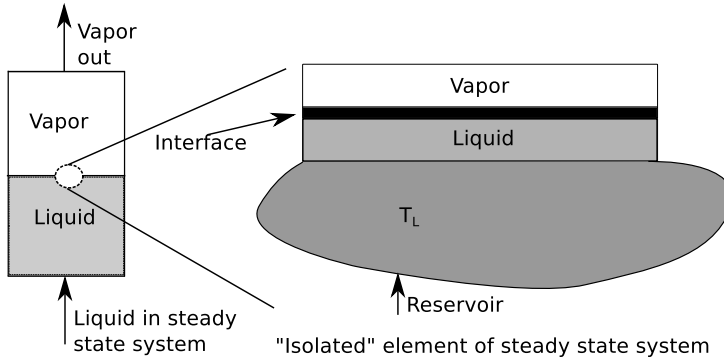


Fig. 3.3: A schematic of the steady-state system and the related isolated system, according to [25].

The temperature and pressure in the vapor are T_v and p_v , respectively and T_l , p_l for the liquid. The energy to maintain the liquid temperature is provided from the surroundings. Within the system, consider now a small "isolated" volume element in steady state also illustrated in figure 3.3. In the small volume element it is assumed that a given molecule is either in the liquid or gas

3.3. Statistical rate theory

phase. Furthermore, the phases are uniform towards the interface.

At a time instant t , T_l and T_v in the small volume are presumed to be the same as for the steady-state system and the number of molecules in the liquid and gas phases are given by N_l and N_v , respectively. The central approximation is that at t the evaporation rate in the small volume is the same as in the steady-state system. This enables to use an expression for the evaporation rate in the steady-state system.

Each small volume has a temperature and, thereby, a limited quantum mechanical energy range ΔE^α , where α is either l or v , can correspond to this temperature. Now, let the number of quantum mechanical states of the isolated system $\Omega(\lambda_j)$ be put in relation to the molecular distribution λ_j , which is within the energy range of the isolated system. With $u_\phi(\lambda_j)$ denoting one of these states the following applies:

$$1 \leq \phi \leq \Omega(\lambda_j), \quad (3.16)$$

which are viewed as unperturbed states where ϕ is an index. The molecular configuration of the system λ_j is

$$\lambda_j(N_l, N_v) : \quad (N_l^1, N_l^3, N_l^3, \dots, N_l^\eta, \dots, N_l^C), (N_v^1, N_v^3, N_v^3, \dots, N_v^\eta, \dots, N_v^C), \quad (3.17)$$

where the objective is to predict the rate at which a given component η transfers from the liquid to the vapor. There will be a virtual molecular distribution λ_k corresponding to the transfer of a molecule from the liquid to the vapor. The number of quantum mechanical states of the isolated system for this distribution is $\Omega(\lambda_k)$ and unperturbed states is $u_\Xi(\lambda_k)$. Thus

$$1 \leq \Xi \leq \Omega(\lambda_k), \quad (3.18)$$

with Ξ as index and

$$\lambda_k(N_l - 1, N_v + 1) : \quad (N_l^1, N_l^3, N_l^3, \dots, N_l^\eta - 1, \dots, N_l^C), (N_v^1, N_v^3, N_v^3, \dots, N_v^\eta + 1, \dots, N_v^C). \quad (3.19)$$

The probability per unit area for a transition from a state corresponding to λ_j to a state corresponding to λ_k can be obtained by

$$\tau[\lambda_j \rightarrow \lambda_k] = K[(\lambda_j), (\lambda_k)] \frac{\Omega(\lambda_k)}{\Omega(\lambda_j)}. \quad (3.20)$$

where

$$K[(\lambda_j), (\lambda_k)] = \frac{2\pi}{\hbar} \xi_j |V_{\phi\Xi}|^2. \quad (3.21)$$

K is the exchange rate, ξ_j is the microscopical density of states for the molecular configuration, λ_j and $V_{\phi\Xi}$ are the matrix elements for the operator \hat{V} which is responsible for the transition. At same t an opposite process will

happen by which a molecule transition to the molecular configuration λ_p is described. This probability is, similarly, given as

$$\tau[\lambda_j \rightarrow \lambda_p] = K[(\lambda_j), (\lambda_p)] \frac{\Omega(\lambda_p)}{\Omega(\lambda_j)}, \quad (3.22)$$

with

$$\lambda_p(N_l + 1, N_v - 1) : \quad (N_l^1, N_l^3, N_l^3, \dots, N_l^\eta + 1, \dots, N_l^C), (N_v^1, N_v^3, N_v^3, \dots, N_v^\eta - 1, \dots, N_v^C). \quad (3.23)$$

The evaporation process can now be written as

$$J_{lv} = \tau[\lambda_j \rightarrow \lambda_k] - \tau[\lambda_j \rightarrow \lambda_p], \quad (3.24)$$

which can be rewritten using the Boltzmann definition of entropy¹ to

$$J_{lv} = K[(\lambda_j), (\lambda_k)] e^{\frac{S(\lambda_k) - S(\lambda_j)}{k_B}} - K[(\lambda_j), (\lambda_p)] e^{\frac{S(\lambda_p) - S(\lambda_j)}{k_B}}. \quad (3.25)$$

Thus, from this equation a mass flux from liquid to vapor, i.e. the evaporation flux can be calculated. However, one needs to know the entropy change.

3.3.1 Calculation of entropy change

Since entropy is an extensive state variable the total change in entropy during a transition is given as the following sum of entropy changes for the liquid, vapor, and reservoir:

$$S(\lambda_k) - S(\lambda_j) = \sum_{i=l,v,R} (S^i(\lambda_k) - S^i(\lambda_j)), \quad (3.26)$$

where R denotes reservoir. Using the so-called Euler relation [48] the entropy change can be written as

$$\begin{aligned} S(\lambda_k) - S(\lambda_j) &= \left(\frac{H_l(\lambda_k)}{T_l} - \frac{H_l(\lambda_j)}{T_l} \right) + \left(\frac{H_v(\lambda_k)}{T_v} - \frac{H_v(\lambda_j)}{T_v} \right) + \left(\frac{\mu_l}{T_l} - \frac{\mu_v}{T_v} \right) \\ &\quad + \left(\frac{H_R(\lambda_k)}{T_l} - \frac{H_R(\lambda_j)}{T_l} \right) \\ &= \left(\frac{\mu_l}{T_l} - \frac{\mu_v}{T_v} \right) + \left(\frac{1}{T_v} - \frac{1}{T_l} \right) (H_v(\lambda_k) - H_v(\lambda_j)). \end{aligned} \quad (3.27)$$

The last rewriting can be done because any intensive state variable will remain unchanged during a transition. This is true because we consider isolated system with no net energy change. Thus,

$$(H_l(\lambda_k) - H_l(\lambda_j)) + (H_v(\lambda_k) - H_v(\lambda_j)) + (H_R(\lambda_k) - H_R(\lambda_j)) = 0. \quad (3.28)$$

¹The Boltzmann definition of entropy is $S(\lambda_d) = k_B \ln(\Omega(\lambda_d))$.

3.3. Statistical rate theory

Introducing the molecular specific enthalpy $h = H/N$, the enthalpy expression in equation (3.27) can be replaced by $h_v \Delta N_v$. The transition process involves only one molecule, leaving $\Delta N_v = 1$. Finally, the entropy change is given as

$$S(\lambda_k) - S(\lambda_j) = \left(\frac{\mu_l}{T_l} - \frac{\mu_v}{T_v} \right) + h_v \left(\frac{1}{T_v} - \frac{1}{T_l} \right). \quad (3.29)$$

The following equation is valid for the opposite process

$$S(\lambda_k) - S(\lambda_j) = - (S(\lambda_p) - S(\lambda_j)). \quad (3.30)$$

3.3.2 Equilibrium exchange rate

To find mass flux using equation (3.25) one also needs to know the molecular exchange rate K . In order to obtain an expression for K , consider a system in the limit of equilibrium where the entropy before and after a transition is unchanged. In that limit, equation (3.25) reduces to

$$J_{vl} = K[(\lambda_e), (\lambda_k)] - K[(\lambda_e), (\lambda_p)], \quad (3.31)$$

where λ_e is the molecular distribution at equilibrium and λ_k and λ_p are the molecular distributions on either side of the equilibrium, cf. equation (3.19) and (3.23), respectively. At equilibrium the net flux must be zero leading to

$$K[(\lambda_e), (\lambda_f)] = K[(\lambda_e), (\lambda_b)] = K_e, \quad (3.32)$$

indicating that $K[(\lambda_e), (\lambda_f)]$ is independent of the molecular configuration. Inspired by this, $K[(\lambda_j), (\lambda_k)]$ is generalized to apply to all near-equilibrium transitions. Thus, combining equation (3.29) and (3.30) with equation (3.25) yields the SRT expression for the rate of evaporation:

$$J_{lv} = K_e \left(e^{\frac{1}{k_B} \left(\left(\frac{\mu_l}{T_l} - \frac{\mu_v}{T_v} \right) + h_v \left(\frac{1}{T_v} - \frac{1}{T_l} \right) \right)} - e^{-\frac{1}{k_B} \left(\left(\frac{\mu_l}{T_l} - \frac{\mu_v}{T_v} \right) + h_v \left(\frac{1}{T_v} - \frac{1}{T_l} \right) \right)} \right). \quad (3.33)$$

K_e can be obtained using classical kinetic theory. At equilibrium the exchange rate between the liquid and vapor can be determined from the rate at which vapor molecules hit the water surface assuming that all vapor molecules colliding with the surface are transferred to the liquid. The equilibrium exchange rate can then be written as

$$K_e = \frac{p_l^e}{\sqrt{2\pi m k_B T^e}}, \quad (3.34)$$

where m is molecular mass and the notation e denotes equilibrium. Equation (3.34) can be seen to be the condensation flux from the Hertz-Knudsen formula in a per unit molecule version, c.f. equation (3.3). The equilibrium

vapor pressure can be found by equating the chemical potential for the liquid and vapor with the saturated condition as reference state. Hence

$$\mu_l(T_l, p_l^e) = \mu(T_l, p_{sat}(T_l)) + V_m(p_l^e - p_{sat}(T_l)), \quad (3.35)$$

with V_m as the molar specific volume of the liquid. The chemical potential for the vapor, with the same reference state, is

$$\mu_v(T_l, p_v^e) = \mu(T_l, p_{sat}(T_l)) + k_B T \ln \frac{p_v^e}{p_{sat}(T_l)}. \quad (3.36)$$

Combining equation (3.35) with (3.36) gives rise to

$$p_v^e = \eta p_{sat}(T_l), \quad (3.37)$$

where

$$\eta = e^{\frac{V_m}{V_v} \left(\frac{p_l^e}{p_{sat}(T_l)} - 1 \right)}, \quad (3.38)$$

with V_v to be the molar specific volume of the vapor. In most situations $V_v \gg V_m$ and $p_l^e \approx p_{sat}(T_l)$, leading to $\eta \approx 1$. K_e may now be expressed as

$$K_e = \frac{\eta p_{sat}(T_l)}{\sqrt{2\pi m k_B T}}. \quad (3.39)$$

The pressure discontinuity due to surface tension can be found by considering a liquid drop cut in the middle, where the two parts of the droplet acts on each other [49]. A mechanical equilibrium requires

$$\begin{aligned} (p_l - p_v) \pi r^2 &= 2\pi r \gamma \\ \Downarrow \\ (p_l - p_v) &= \frac{2\gamma}{r}, \end{aligned} \quad (3.40)$$

where r is the curvature radius and γ is surface tension. Finally, under the assumption of ideal gas [23, 25, 50] equation (3.29) can be written as

$$\begin{aligned} \frac{\Delta S}{k_B} &= 4 \left(1 - \frac{T_v}{T_l} \right) + \left(\frac{1}{T_v} - \frac{1}{T_l} \right) \sum_{l=1}^3 \left(\frac{\hbar \omega_l}{2k_B} + \frac{\hbar \omega_l}{k_B e^{\frac{\hbar \omega_l}{k_B T_v}} - k_B} \right) + \\ &\quad \frac{V_m}{k_B T_l} (p_l - p_{sat}(T_l)) + \ln \left[\left(\frac{T_v}{T_l} \right)^4 \left(\frac{p_{sat}(T_l)}{p_v} \right) \right] + \ln \left[\frac{q_{vib}(T_v)}{q_{vib}(T_l)} \right], \end{aligned} \quad (3.41)$$

where the vibrational partition function for the ideal polyatomic molecules may be expressed as

$$q_{vib}(T) = \prod_{l=1}^3 \frac{e^{-\frac{\hbar \omega_l}{2k_B T}}}{1 - e^{-\frac{\hbar \omega_l}{k_B T}}}. \quad (3.42)$$

3.3. Statistical rate theory

The vibrational frequencies of the covalent bonds of the water molecule are 1590 cm^{-1} , 3651 cm^{-1} and 3756 cm^{-1} [24].

As highlighted by Ward and Fang [25], the SRT expression for the mass transport at the interface is dependent on the instantaneous values of the local equilibrium in each phase: T_l , T_v , p_l and p_v and, thus, free of any fitting-parameters.

4. Lattice Boltzmann method

In the last couple of decades the lattice Boltzmann method has become a popular approach to simulate complex fluid flows [51, 52]. The method, among others, is an alternative tool for numeric fluid dynamics compared to, for example, classical CFD approaches. The method has been proven to be applicable in the fields ranging from fluid mechanics, biology and material science to relativistic and quantum transport [52–54]. Historically, the method originates from lattice gas automaton [55]. However, here it will be emphasized how the lattice Boltzmann equation (LBE) can be viewed as a simplified version of the Boltzmann equation (BE). As presented in the BE, the macroscopic dynamics is originated by dynamics of the atomic scale particles, in LBE, the macroscopic properties arise from the dynamics of fictive particles moving in a regular space-time lattice [53]. This approach significantly reduces the complexity associated with the velocity space.

This chapter provides a foundation of the LB method. It is shown that LBE equation can be derived from a discrete version of the BE and then the algorithm for doing LB simulations is presented. This will be followed by the discussion of the entropic LBE providing excellent numerical stability and some LBE boundary conditions will be presented. Finally, approaches to simulate multiphase flows with the LB method will be reviewed.

4.1 The lattice Boltzmann equation

Lets consider hypothetical moving particles described by a discrete set of velocities $\{\vec{c}_0, \vec{c}_1, \dots, \vec{c}_N\}$ so that the BE can be written as [56]

$$\frac{\partial f_i(\vec{r}, t)}{\partial t} + \vec{c}_i \cdot \nabla f_i(\vec{r}, t) = Q_i(f_i(\vec{r}, t)), \quad i = 0, \dots, N \quad (4.1)$$

where Q_i is the collision operator which represents the particle interaction and $f_i(\vec{r}, t)$ is the discrete one-particle probability distribution function with the notation $f_i(\vec{r}, t) = f(\vec{r}, t, \vec{c}_i)$. Same notation is used for the collision term Q_i , which drives the distributions f_i towards the equilibrium distribution f_i^{eq}

at a time τ . The local fluid density and momentum, the first two moments of f_i , are obtained in a similar manner as in the continuous case:

$$\rho = \sum_{i=0}^N f_i, \quad \rho \vec{u} = \sum_{i=0}^N \vec{c}_i f_i. \quad (4.2)$$

For the purpose of efficient simulations it is desirable to work with the time scale of free flights dt , for which $dt \gg \tau$ [56]. Integrating equation (4.1) over time leads to

$$\begin{aligned} f_i(\vec{r} + \vec{c}_i dt, t + dt) &= f_i(\vec{r}, t) + \int_0^{dt} Q_i(f_i(\vec{r} + \vec{c}_i ds, t + ds)) ds \\ &\approx f_i(\vec{r}, t) + \frac{dt}{2} (Q_i(f_i(\vec{r}, t)) + Q_i(f_i(\vec{r} + \vec{c}_i dt, t + dt))) + \mathcal{O}(dt^3) \end{aligned} \quad (4.3)$$

where the trapezoidal rule has been used [56], which gives rise to a second order accuracy $\mathcal{O}(dt^2)$. As seen, equation (4.3) represents an implicit system, meaning the "step" into the "future" dependence on the "future". To obtain an explicit scheme, where the point in the "future" only depends on points in the "past", the following modified distributions are introduced [57]:

$$\tilde{f}_i(\vec{r}, t) = f_i(\vec{r}, t) - \frac{dt}{2} Q_i(f_i(\vec{r}, t)). \quad (4.4)$$

These modified distributions are, strictly speaking, not distributions, since they are not bound to be non-negative functions. The collision term Q_i can be positive and in fact one of the Q_i 's must be positive because the mass conservation dictates $\sum_{i=0} Q_i = 0$. However, $\sum_{i=0} f_i = \sum_{i=0} \tilde{f}_i$ leads to $f_i^{eq} = \tilde{f}_i^{eq}$. Similar, for the fluid momentum $\sum_{i=0} \vec{c}_i f_i = \sum_{i=0} \vec{c}_i \tilde{f}_i$.

Before proceeding with the derivation of the LBE the collision operator should be addressed. It can be simplified to the quasi-linear form [58]

$$Q_i(f_i(\vec{r}, t)) = -\Omega_{ij}(\tilde{f}_j(\vec{r}, t) - \tilde{f}_j^{eq}(\vec{r}, t)), \quad (4.5)$$

where the scattering matrix Ω_{ij} is cyclic, meaning that Ω_{ij} only depends on $|i - j|$ and therefor symmetric. Furthermore, Ω_{ij} must be negative-definite. For an elaboration of these properties see [53]. Performing the relaxation of Ω_{ij} is known as the multiple-relaxation time (MRT) method. This approach offers some freedom to improve stability of the scheme [51]. However, due to the higher computational demands and the issues associated with developing the proper scattering matrix Ω_{ij} , the method will not be under the focus here. Instead the Bhatnagar–Gross–Krook (BGK) [53] approximation or, when applied to the LBE, the lattice Bhatnagar–Gross–Krook (LBGK) approximation will be used. The approximation allows the collision term to be written as

$$Q_i(\tilde{f}_i(\vec{r}, t)) = -\frac{\tilde{f}_i(\vec{r}, t) - \tilde{f}_i^{eq}(\vec{r}, t)}{\tau}, \quad (4.6)$$

4.1. The lattice Boltzmann equation

which greatly simplifies the relaxation process. Note, that for the LBGK approximation

$$Q_i(\bar{f}_i(\vec{r}, t)) = \left(1 + \frac{dt}{2\tau}\right) Q_i(f_i(\vec{r}, t)). \quad (4.7)$$

It should be stressed that the modified distributions are not necessarily physical distribution functions. However, they are often referred to as distributions or populations in the literature. Furthermore, the notation \bar{f}_i will be changed to f_i . However, the meaning of the populations f_i are not the same as above. The LBE with LBGK approximation can be written as

$$\begin{aligned} f_i(\vec{r} + \vec{c}_i dt, t + dt) &= f_i(\vec{r}, t) - \frac{dt}{\tau + dt/2} \left(f_i(\vec{r}, t) - f_i^{eq}(\vec{r}, t) \right) \\ &= f_i(\vec{r}, t) - \omega \left(f_i(\vec{r}, t) - f_i^{eq}(\vec{r}, t) \right), \end{aligned} \quad (4.8)$$

where the relaxation frequency $\omega = \frac{dt}{\tau + dt/2}$ is introduced. In the numerical scheme it is normal practice to set $dr = dt = 1$. The task is now to adjust the approximate equilibrium function f_i^e and ω so that equation (4.8) recovers the wanted target equations. To recover the incompressible NS equations, where $Ma \ll 1$, the four leading moments of the approximate equilibrium function f_i^e with the discrete velocity \vec{c}_i must be [51, 52]

$$\sum_{i=1} f_i^e = \rho, \quad (4.9a)$$

$$\sum_{i=1} f_i^e c_\alpha = \rho u_\alpha, \quad (4.9b)$$

$$\sum_{i=1} f_i^e c_\alpha c_\beta = \rho c_s^2 \delta_{\alpha\beta} + \rho u_\alpha u_\beta, \quad (4.9c)$$

$$\sum_{i=1} f_i^e c_\alpha c_\beta c_\gamma = \frac{\rho}{3} (u_\alpha \delta_{\beta\gamma} + u_\beta \delta_{\gamma\alpha} + u_\gamma \delta_{\alpha\beta}) + \rho u_\alpha u_\beta u_\gamma, \quad (4.9d)$$

where the subscripts α, β, γ correspond to vector coordinates, c_s is the speed of sound for the lattice and δ is the Kronecker delta function. The approximate equilibrium function f_i^e is an expansion of Maxwell-Boltzmann distribution in the limit where $Ma \ll 1$ and it can be shown to be

$$f_i^e = \rho w_i \left(\underbrace{1}_{0^{th} \text{ order}} + \underbrace{\frac{\vec{c}_i \cdot \vec{u}}{c_s^2}}_{1^{st} \text{ order}} + \underbrace{\frac{(\vec{c}_i \cdot \vec{u})^2}{2c_s^4} - \frac{u^2}{2c_s^2}}_{2^{nd} \text{ order}} \right) + \mathcal{O}(u^3) \quad (4.10)$$

in order to recover the NS from equation (4.8). w_i are the lattice specific weights. The NS equations are obtained by a multi-scale Chapman-Enskog expansion of equation (4.8) in time t and space \vec{r} . A detailed derivation can be

found in [59]. The kinematic viscosity ν is related to the relaxation frequency as

$$\nu = c_s^2 \left(\frac{1}{\omega} - \frac{1}{2} \right) dt, \quad (4.11)$$

with the relaxation frequency $\omega \in]0, 2[$. It must be noted, that the kinematic viscosity can be chosen independent of the time step dt . Since the NS are obtained for low Ma , it is important that the velocity, in lattice units $[L.U.]$, must be lower than 0.05 [53].

An elaboration of the lattice units will be given later. A final remark regarding the approximate equilibrium function f_i^e must be given. The number of terms included in the expansion determines which transport equations will be recovered. If only the 0th order contribution is considered the recovered transport equation will be a diffusion equation. However, if the 1'st order term is also considered the LBE will recover a convection-diffusion equation, both with the diffusion coefficient D given by [60, 61]

$$D = c_s^2 \left(\frac{1}{\omega} - \frac{1}{2} \right) dt. \quad (4.12)$$

And, finally, if the 2'nd order term is included, the recovered transport equation will be the NS equations.

Next, the lattice specific weights w_i and speed of sound c_s must be mentioned. To specify a given lattice, a common terminology is used to refer to the number of dimensions DX and then to the number of discrete velocities QXX [51]. For example, $D2Q9$ is a two-dimensional lattice with nine discrete velocities at each discretization node. Only the so-called product lattices, $D1Q3$, $D2Q9$ and $D3Q27$ lattice, will be introduced. $D1Q3$ and $D2Q9$ lattices are illustrated in figure 4.1. $D2Q9$ is an extrusion of $D1Q3$ and $D3Q27$ is an extrusion of $D2Q9$ lattice. The fictitious particles are bound to move in these lattices, for example, in the case of $D1Q3$ a particle can either move "left", stay at the node or move "right". All the lattices introduced here have a zero velocity vector $\vec{c}_0 = \vec{0}$.

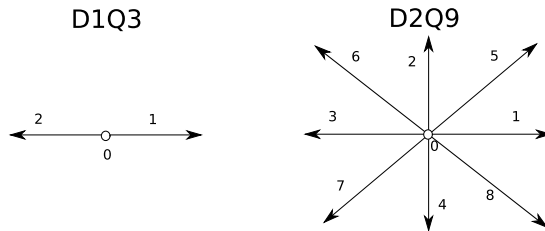


Fig. 4.1: Illustration of D1Q3 and D2Q9 lattices.

The lattice specific weights w_i or simply weights along with c_s for the different lattices which fulfill equations (4.9a)-(4.9d) and (4.10) are listed in table

4.1. The lattice Boltzmann equation

4.1. It must be mentioned that these lattices are not the only lattices that can be used to recover the NS equations. However, other lattices will not be described here.

Table 4.1: Lattice parameters for D1Q3, D2Q9, and D3Q27 lattices.

	c_s	w
D1Q3	$1/\sqrt{3}$	$w_i = \begin{cases} 2/3 & i = 0 \\ 1/6 & i = 1, 2 \end{cases}$
D2Q9	$1/\sqrt{3}$	$w_i = \begin{cases} 4/9 & i = 0 \\ 1/9 & i = 1 - 4 \\ 1/36 & i = 5 - 8 \end{cases}$
D3Q27	$1/\sqrt{3}$	$w_i = \begin{cases} 8/27 & i = 0 \\ 2/27 & i = 1 - 6 \\ 1/216 & i = 7 - 14 \\ 1/54 & i = 15 - 26 \end{cases}$

4.1.1 The choice of LB units

In order to apply any LBE to physical problems it must first be nondimensionalized. Since the discretization parameters dx and dt are coupled by the velocity limit in the LB framework any comparison of a physical system and a LB system must be carried through nondimensional quantities. This is done by identifying, for instance the characteristic density ρ' , length L' and time t' of the physical system. Examples on how to compare quantities is shown in table 4.2. Also, dimensionless numbers like Ma must be equal for both systems.

Table 4.2: Examples on how to compare different nondimensional quantities where the ' denotes physical units and absence of ' denotes lattice units. The nondimensional length is obtained by dividing the "physical length" where the ratio of the viscosity ν and velocity u where ν and u are in the same set of units. Other quantities are obtained in the similar way.

Time	Length	Velocity	Viscosity
$\frac{t}{L/u} = \frac{t'}{L'/u'}$ or $\frac{t}{L^2/\nu} = \frac{t'}{L'^2/\nu'}$	$\frac{L}{\nu/u} = \frac{L'}{\nu'/u'}$	$\frac{u}{\nu/L} = \frac{u'}{\nu'/L'}$	$\frac{\nu}{uL} = \frac{\nu'}{u'L'}$

4.1.2 The LB algorithm

One of the advantages of the LB scheme is its simplicity. The time steps are divided into two steps; streaming and colliding, with the latter also called relaxation. Apart from these two types of steps the boundary conditions

have to be applied. The algorithm can be implemented in a very efficient manner [53] and it is listed below.

1. Formulate the problem in lattice units.
2. Initialize the lattice with equilibrium populations based on the initial conditions.
3. Perform time stepping by streaming and colliding or vice versa.
 - Perform relaxation step at each lattice node.
 - Stream the appropriate populations to the neighboring lattice nodes.
 - Apply boundary conditions. This step is usually done right after the streaming step.
4. Post process the populations to obtain the macroscopic properties.

Several data structures can be used to perform efficient LB simulations. Various implementation strategies can be seen in [62].

4.2 Entropic lattice Boltzmann method

The LBGK model suffers from numerical instabilities which arise when the velocity profile and its gradients become too large for a given lattice. This limits the LBGK model to simulations of systems with relatively small Reynolds numbers [51]. The instability can be improved by the MRT model but it can not be completely removed. This problem has, however, been solved by the so-called entropic lattice Boltzmann (ELB) method, ensuring explicit unconditional stability for single phase flows.

The ELB method includes a discrete form of the H-theorem constraining the evolution distribution functions so they stay non-negative at every grid point at each time step [63–67]. A discrete form of the H-function can be identified as

$$H = \sum_{i=0} f_i \ln \frac{f_i}{w_i}, \quad (4.13)$$

which can be proven to be a convex function of the populations. In the ELB method it is enforced that the H-function does not increase. This is ensured in the collision process. The ELB method is a generalization of the LB method and the ELBE is given as [67]

$$f_i(\vec{r} + \vec{c}_i, t + 1) = f_i(\vec{r}, t) - \alpha\beta \left(f_i(\vec{r}, t) - f_i^{eq}(\vec{r}, t) \right), \quad (4.14)$$

where the β coefficient is connected with the kinematic viscosity through

$$\nu = c_s^2 \left(\frac{1}{2\beta} - \frac{1}{2} \right), \quad \beta \in]0, 1[. \quad (4.15)$$

4.3. Boundary conditions

The entropy balance is maintained at each node for each time step through the α parameter. It is the non-trivial root of the entropy balance between the current state and the so-called mirrored state:

$$H(f) = H(f + \alpha(f^{eq} - f)). \quad (4.16)$$

Hence, in the ELB method the collision procedure is slightly changed:

- Perform relaxation step at each lattice node.
 1. Calculate the H-function for the current state.
 2. Calculate the α parameter from equation (4.16). This is usually in a numerically manner.

Another important feature of the entropy inclusion is the physical justification of f^{eq} . By extremization of the functional δH_f with the Lagrange multipliers $\mu(\vec{r}, t)$ and $\beta_\alpha(\vec{r}, t)$ given by

$$\delta H_f = \delta \sum_{i=0} [h_i(f_i) - \mu f_i - \beta_\alpha f_i c_{i\alpha}] = 0, \quad h_i(f_i) = f_i \ln(f_i/w_i), \quad (4.17)$$

subjected to collision constraints for the mass and momentum conservation, the f_i^{eq} function can be found. With Lagrange multipliers obtained from the first and second moments $\{\rho, \rho \vec{u}\} = \sum_i \{1, \vec{c}_i\} \{f_i^{eq}\}$ the following formula is obtained:

$$f_i^{eq} = \rho w_i \prod_{\alpha}^D (2 - B) \left(\frac{2u_\alpha + B}{1 - u_\alpha} \right)^{c_{i\alpha}}, \quad (4.18)$$

where D is the number of dimensions and $B = \sqrt{1 + 3u_\alpha^2}$ [51]. By expanding equation (4.18) until the third order equation (4.18) becomes equal to equation (4.10), justifying the general choice of the equilibrium function in LB approach.

4.3 Boundary conditions

A very important part of any numerical scheme are the boundary conditions. The accuracy, stability and implementation details are of great importance. Here, a number of the popular approaches will be reviewed. For illustration purposes, a boundary node for the D2Q9 lattice with the unknown distribution functions as dashed arrows is shown in figure 4.2.

Periodic boundary conditions is simple to apply. Distributions leaving the domain are simply copied to the appropriate node at the other end of the domain [53].

A wide used boundary condition is the no-slip boundary which in the LB method can be obtained by the so-called **bounce-back** rules. Two versions of

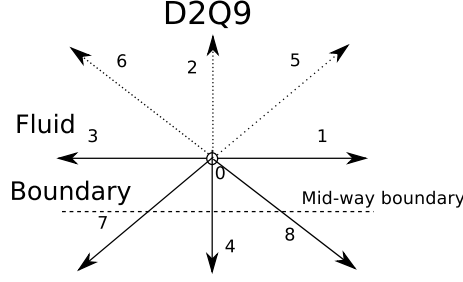


Fig. 4.2: Illustration of the D2Q9 lattice at a boundary node, where the dashed arrows are the unknown populations.

the rule exists; the on-grid and mid-grid bounce-back [53]. It has to do with the position of the wall relative to the node. The on-grid boundary means that the physical boundary lies on the grid line, corresponding to the boundary illustrated in figure 4.2. It is implemented by reversing each population in the opposite direction after which the collision step is done. This is, then, followed by the streaming step. The mid-way bounce-back is a bit harder to implement but it provides better accuracy [68]. As the name suggests, the location of the wall becomes mid-way into the boundary nodes illustrated in figure 4.2. It is implemented by keeping the populations that would leave the domain at the node and copy the populations to the opposite direction. Hence,

$$f_i^{bb} = f_{-i}. \quad (4.19)$$

The so-called **Zou-He boundary** conditions can be used to set the velocity and density and, therefore, also pressure at the boundary node [69]. They are easy to implement: the unknown populations are obtained locally and have second order accuracy [70]. The Zou-He boundaries are used at the streaming step. The derivation of the boundaries can be found in [69].

To introduce the Zou-He boundary conditions consider the node in figure 4.2 as a node with either the velocity \vec{u} specified or the ρ density specified. The unknown populations are f_2 , f_5 and f_6 . The formulas, according to Zou and He, for the missing populations are listed below:

- **Velocity boundary** according to Zou and He [69]:

$$\begin{aligned} f_2 &= f_4 + \frac{2}{3}\rho u_y \\ f_5 &= f_7 - \frac{1}{2}(f_1 - f_3) + \frac{1}{2}\rho u_x + \frac{1}{6}\rho u_y \\ f_6 &= f_8 + \frac{1}{2}(f_1 - f_3) - \frac{1}{2}\rho u_x + \frac{1}{6}\rho u_y \\ \rho &= \frac{1}{1-u_y}[f_0 + f_1 + f_3 + 2(f_4 + f_7 + f_8)] \end{aligned}$$

- **Density boundary**, where $u_x = 0$, according to Zou and He [69]:

$$\begin{aligned} f_2 &= f_4 + \frac{2}{3}\rho u_y \\ f_5 &= f_7 - \frac{1}{2}(f_1 - f_3) + \frac{1}{6}\rho u_y \end{aligned}$$

4.4. Multiphase flow

$$f_6 = f_8 + \frac{1}{2}(f_1 - f_3) + \frac{1}{6}\rho u_y$$

$$u_y = 1 - \frac{f_0 + f_1 + f_3 + 2(f_4 + f_7 + f_8)}{\rho}$$

Another approach to set the on-grid boundaries, which is appropriate for high Reynolds numbers, is the Tamm – Mott-Smith (TMS) boundary conditions [71, 72]. Here target densities ρ_{tgt} and velocities \vec{u}_{tgt} are specified. It is implemented at the streaming step by dividing the populations into an equilibrium part and a non-equilibrium part:

$$f_i \rightarrow f_i^{eq}(\rho_{tgt}, \vec{u}_{tgt}) + f_i^{neq}. \quad (4.20)$$

If the population is missing the non-equilibrium part is given as

$$f_i^{neq} = f_i^{eq}(\rho_{tgt}, \vec{u}_{tgt}) - f_i^{eq}(\rho, \vec{u}), \quad (4.21)$$

while for the non-missing populations the non-equilibrium part is given as

$$f_i^{neq} = f_i - f_i^{eq}(\rho, \vec{u}). \quad (4.22)$$

All the mentioned boundary handling are based on regular boundaries. If, however, curved boundaries are addressed various extrapolation schemes has been developed [73]. Recently, schemes for moving boundaries [74] and out-flow based on Grad's distribution approximation [75] has been developed. These, however, are beyond the scope of this chapter.

4.4 Multiphase flow

In order to simulate physical phenomena like condensation, approaches to model flows of multiple phases are necessary. For the condensation issue the phases would, thus, be the liquid and its vapor. One of the advantages of the LB method is in the possibilities of multiphase modeling. There exists a number of approaches but it is hardly possible to overview all multiphase methods. For more details about them look in [51, 52, 76]. Here, the pseudo-potential method [77, 78], free surface method [79, 80], and the newly developed entropic multiphase model [81] will be presented due to their importance for the current work.

4.4.1 Shan-Chen pseudo-potential method

To include non-linear interactions between particles the following force between nearest neighbors is suggested according to Shan and Chen [77, 78]:

$$\vec{F} = -G\psi[\rho(\vec{r} + \vec{c}_i dt, t)] \sum_{i=0} w_i \psi[\rho(\vec{r} + \vec{c}_i dt, t)] \vec{c}_i. \quad (4.23)$$

where G is the interaction strength and ψ is the interaction potential given as

$$\psi(\rho) = \psi_0 e^{-\rho_0/\rho}, \quad (4.24)$$

where ψ_0 and ρ_0 are arbitrary constants. ψ must be monotonically increasing and bounded. In general, a popular method for introducing forcing in the LB scheme is the exact difference method [82]. This method is also described in the attached paper B.

A general issue with pseudo-potential method is that the surface between the phases becomes diffuse and spurious velocities occur at the interface. However, one of the advantages is that no explicit surface handling is necessary. Another issue with the original Shan-Chen model is that it is only possible to model the phases with small density ratios. This was, however, solved by introducing an interaction potential, which is based on a non-ideal equation-of-state (EOS). With this a density ratio of 1000:1 can be achieved [83]. For a recent critical review of the pseudo-potential method see [84].

4.4.2 Free surface framework

In the free surface framework the grid points are labeled to be either a "gas" node, "interface" node or a "liquid" node [79, 80]. Often, the gas phase is never addressed, thus, simplifying the simulations. At the interface nodes the populations which should stream from the gas nodes are reconstructed, while the streaming from the interface and liquid nodes is unchanged. The collision step is also unchanged.

The surface tracking can be done in two ways: either by a level set method or by tracking the mass. The mass tracking algorithm is described in paper B attached to this thesis. The level set method introduces a function Φ where $\Phi > 0$ for the gas phase and $\Phi < 0$ for the liquid phase. The value of Φ at a grid point is the signed distance from the node center to the closest interface point. In the liquid Φ is advected with the velocity profile, while the velocity profile in the gas phase needs to be extrapolated. This extrapolation can be considered to be computational costly.

The level set method enables a smooth and simple surface representation while e.g. mass conservation requires implementation extensions. The mass tracking is simple and efficient in its implementation and under this algorithm the mass is conserved. However, it can give rise to surface artifacts and the surface curvature estimations can be considered to be costly. Because of the inherent mass conservation the mass tracking algorithm was chosen in paper B.

The free surface approach is still subject to research and recently a new boundary handling for the free surface has been proposed [85] which is proven to provide second order spatial accuracy.

4.4. Multiphase flow

4.4.3 Entropic multiphase approach

The novel thermodynamically consistent multiphase lattice Boltzmann model [81] also includes a forcing scheme but based on the free-energy functional. This implies Korteweg's stress, which gives rise to the following pressure tensor:

$$\mathbf{P} = \left(p - \kappa \rho \nabla^2 \rho - \frac{\kappa}{2} |\nabla \rho|^2 \right) \mathbf{I} + \kappa (\nabla \rho) \otimes (\nabla \rho), \quad (4.25)$$

where \mathbf{I} is the unit tensor, κ is the surface tension coefficient, and p is the pressure obtained from the EOS. The force associated with Korteweg's stress is given as

$$\vec{F} = \nabla \cdot \left(\rho c_s^2 \mathbf{I} - \mathbf{P} \right). \quad (4.26)$$

In [81] a polynomial EOS is suggested. Besides being thermodynamically consistent it is also possible to simulate physical systems, like lamella formations in droplet collisions. This has not been possible before.

5. The reliability concept

Three previous chapters over-viewed main physics concepts which are used in the current work to model humidity and temperature as well as address such phenomena as water condensation and evaporation. However, the end goal of the project is in improvement of reliability of electronics exposed to environmental factors. Therefore, it is now time to introduce main concepts of reliability and link them to the physical quantities which will be modeled and experimentally measured.

5.1 Failure rate

The reliability of an item is a characteristic, which expresses the probability that the item performs the required function under a given set of conditions for a stated period of time [6]. Hence, for any numerical assessment of reliability to be meaningful, the required function, operation conditions, and duration must be stated. A failure, thus, occurs when the item stops performing the required function in the duration time. This can, for example, happen if the item has degraded.

The failure rate $\lambda(t)$ and its dependence on time t is an important concept in reliability analysis. The failure rate of a large population of statistically identical and independent items typically follows a so-called bathtub curve [6], which is illustrated in figure 5.1.

As indicated in figure 5.1 the bathtub curve is divided into three regions; the early failures, constant failure rate, and wear out periods. The characteristics of each period are specified below:

- **The early failure period**, also referred to as the infant mortality period, is related to poor production or installation. The rate of these failures has maximum at the starting point of the device operation and then gradually decreases.
- **The period of constant failure rate** is characterized, as the name sug-

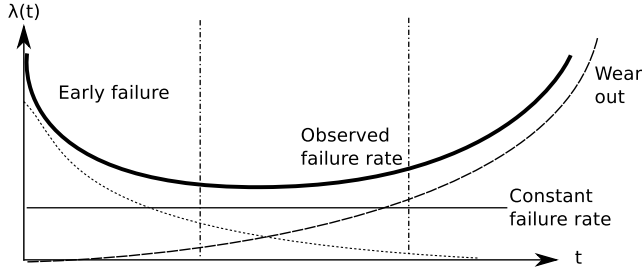


Fig. 5.1: Schematic of the bathtub curve divided into the early failure, constant failure and wear-out periods.

gests, by a failure rate independent of time. In this period the failures occur due to lack of robustness.

- **In the wear out period** the items fail due to aging, wear-out and/or fatigue. The failure rate will, therefore, increase with time.

The bathtub curve is the sum of these three failure periods.

5.2 Probability of failure

The reliability model presented here is focused on the constant failure rate period.

To evaluate the probability of a failure P_f the limit-state function needs to be constructed where P_f , thus, is the probability of exceeding the limited state of the item also called the failure criterion [86]. The limit-state indicates the margin between the load and resistance of the system. It is defined as

$$g(X) = R(X) - L(X), \quad (5.1)$$

where R is the resistance and L is the load of the system. R and L are dependent on random variables X . The reason for this is to include statistical uncertainties in, for example, consumer usage of system and/or variations in production parameters. The probability of failure is given by

$$P_f = P[g(X) < 0] = \int \dots \int f_X(X_1, \dots, X_N) dX_1 \dots dX_N, \quad (5.2)$$

where f_X is the join probability density. The failure region is where $g(X) < 0$, while the safe region is defined by $g(X) > 0$. The condition $g(X) = 0$ defines the failure surface which describes the failure mode. These regions are illustrated in figure 5.2 with two random variables X_1 and X_2 .

The limit-state function represents the physics of the failure mode and there are several approaches to solve $g(X) = 0$. The first order reliability method

5.3. Humidity-related reliability

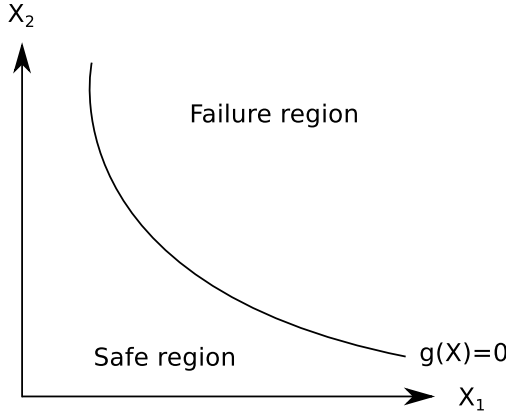


Fig. 5.2: Illustration of the safe and failure regions separated by the failure surface $g(X) = 0$ for two independent random variables.

(FORM) or second order reliability method (SORM) involve transforming the failure function $g(X)$ into a U -space function $g(U)$. Here, the random variables $U_i \sim N(0,1)$ are independent normalized Gaussian distributed variables [86]. The failure function will, then, be approximated by a first or second order expansion. However, this approach relies on the load and resistance represented by analytical formulas. If it is not possible to formulate the function analytically, the probability of failure can be estimated with crude Monte Carlo simulations. With this approach, R and L are sampled with N trials and P_f can be approximated by

$$P_f \approx \frac{N_f}{N}, \quad (5.3)$$

where N_f is the number of trials for which $g(X) < 0$ out of the N trials. The sampling procedure is continued until the wanted accuracy is achieved. This approach is quite general but later it will be shown how it can be used for the climatic reliability issues.

5.3 Humidity-related reliability

In electronics, moisture can significantly affect reliability of PCB. The relative humidity (RH) is, thus, an important stress factor to consider. RH represents a ratio of water vapor in air and it is very much dependent on temperature [87].

High values of RH lead to water condensation and therefore put a system in danger due to possible short circuits and corrosion. Corrosion can also occur when introducing the PCB to a gaseous phase and can, thereby, be hazardous

for electronic systems [8]. Most corrosion mechanisms are such that below a certain RH level nothing happens but when the RH level rises above that limit the corrosion will begin, see e.g. [88]. Therefore, RH value at the location of electronics can be used as a failure criterion because the system will eventually fail if exposed to a high enough RH. Overall, in order to predict humidity-related reliability it is key to have insights in the water vapor and temperature profiles in the system.

6. Experimental setup and modeling methods

This chapter aims to introduce the experimental setup and procedures as well as the modeling approaches used to fulfill the goals of the current project.

6.1 Overview of the simulations and experimental studies

The results described in this thesis are divided into three main parts and presented in the chapters 7-9.

In the first block, the aim is to carry out climatic modeling in enclosures with power electronics to predict temperature and humidity distributions and evolutions. The AquaRIUM setup, which is described below, is used for the verification of the simulations. The starting point is a simulation of induced thermal gradients related to redistribution of humidity in a container having the same configuration as AquaRIUM and comparison with the experimental results obtained by this setup. As a next step, the complexity of a model is increased by adding inside the container a volume with water which can freely evaporate (freely exposed water surface). Finally, natural convection inside the setup is investigated. This situation corresponds to so-called "breathing modes" of an enclosure when water vapor can migrate through small openings in the wall due to the natural convection. To develop models describing these cases the theory presented in chapters 2 and 3 is extensively used.

The second main part concerns a lattice Boltzmann method which is used for modeling of water condensation. Unfortunately, experimental verification of these simulations requires rather sophisticated and complex setup. Therefore, another way is chosen. The results of modeling are verified by comparison with the classic Nusselt condensation model which is widely used for condensation problems and well proved. Thus, combining the lat-

tice Boltzmann approach with the model using equations of gas kinetics and statistical rate theory, which constitute the previous block, allows for simulating of rather complex situations for the humidity evolution which can include evaporation and condensation phenomena.

The final part provides a step to utilize the developed models as tools for reliability assessment of power electronics in enclosures with the relative humidity as the stressing factor.

Details about the experimental setup as well as methodological approaches and key steps of the simulations used to obtain the above mentioned blocks of results are described below.

6.2 Experimental equipment

The experimental setup, called AquaRIUM, consists of a cylindrical tube (with length of 20 cm and radius of 5.5 cm) made of Pyrex glass attached with one side to an aluminum plate and tightened with rubber gaskets (see figure 6.1). The plate has an electrical feedthrough for connection of a temperature and humidity sensor. At the backside of the plate a Peltier element is mounted, thus, allowing to vary temperature using a programmable power supply. The temperature range for this work is 20–60°C. At the other end of the cylinder an aluminum end-cap can be mounted making it possible to close the setup and vary the temperature and humidity inside.

This simple system is designed to verify the models and simulations on humidity and temperature evolution in closed volumes. It is also possible to make openings of controllable size and configuration in the end-cap in order to study thermodiffusion and convection phenomena as provided in paper C. In some of the experiments, which are described in the next chapter and paper A, the end-cap was substituted by a napkin allowing diffusion but blocking convection. One can also put inside a vessel with water. A schematic picture of this setup configuration is shown in figure 6.2.

The configuration used to study enclosure breathing, presented in paper C and section 7.3 is shown in figure 6.3. AquaRIUM is positioned vertically enabling 2D axis symmetric model and, thus, reducing the simulation complexity.

The sensors used for the experiments cover the temperature range from -40°C to 100°C with uncertainty $\pm 1^\circ\text{C}$. RH can be measured from 0% to 100% with a maximum uncertainty of $\pm 5\%$.

The setup is placed in a clean room with stable temperature of $21 \pm 0.5^\circ\text{C}$ and RH of 49%–51% allowing good control of the variable climatic parameters outside AquaRIUM. Prior to the experiments, readings of the sensors placed in the setup were compared with that of another sensor located outside. If the difference was greater than 5%, the sensors were calibrated.

6.2. Experimental equipment

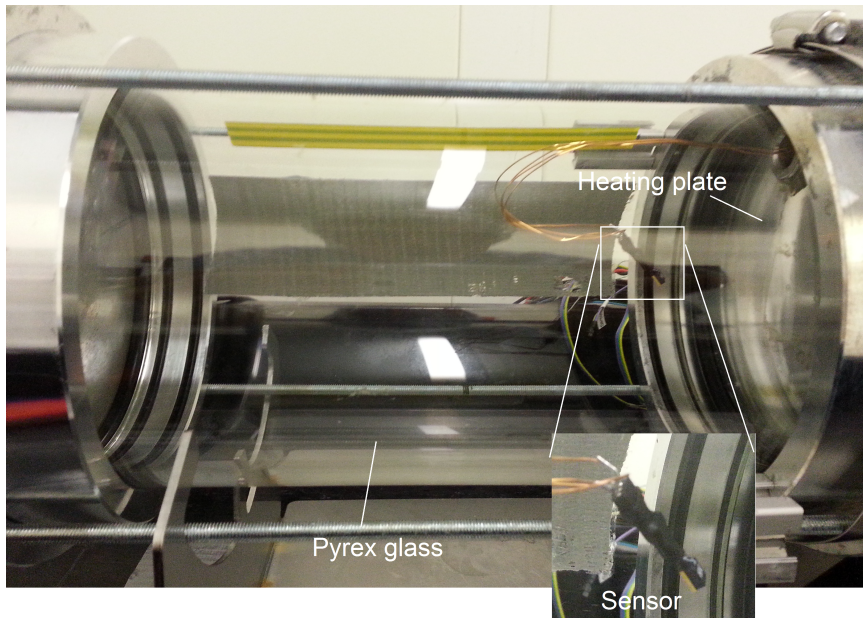


Fig. 6.1: Photograph of the AQUARIUM.

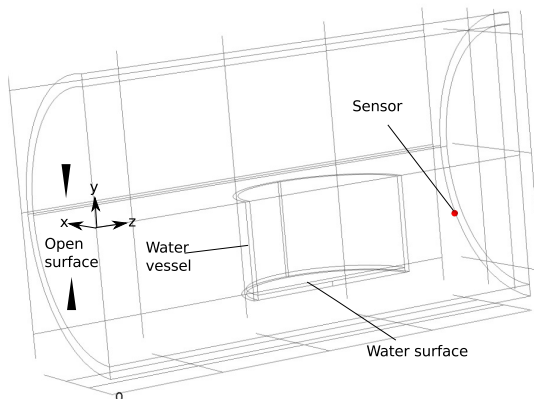


Fig. 6.2: Schematic of the AQUARIUM configuration used for investigating humidity distributions affected by freely exposed surfaces.

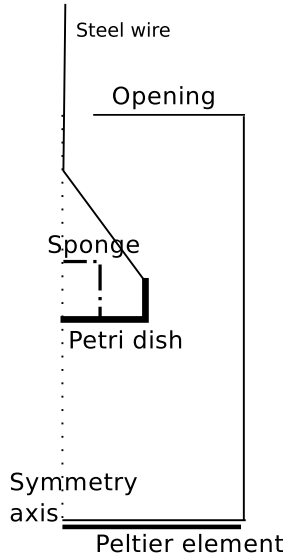


Fig. 6.3: Schematic of the AquaRIUM configuration used for investigating breathing modes.

6.3 Modeling approaches

This section aims to present the modeling approach for the various simulations done for the thesis. First, it is described how air movement and moisture transport are modeled using NS and continuity equations. Also, it is illustrated how temperature can be included with another continuity equation and how the natural convection can be modeled. These concepts relies on the theory described in chapter 2 and they are the foundation for the results in chapter 7 and papers A and C.

Next, in section 6.3.2, it is described how the free surface entropic lattice simulations are set up in order to obtain the results presented in chapter 8 and paper B. These simulations are based on the theory presented in chapter 4. The finite volume approach used for the results shown in chapter 9 and paper D is presented in section 6.3.3

6.3.1 Transport of water vapor as a diluted species in air

In order to get appropriate comparison of the simulated and experimental results, the modeling is carried out for the geometrical configuration identical of that for AquaRIUM. The modeling was performed with the finite element (FEM) software COMSOL Multiphysics [89]. The CFD, non-isothermal flow and chemical species transport modules are used. Every solution obtained is tested for mesh-independence and the meshes are generated using COMSOL.

6.3. Modeling approaches

The air movement is modeled using the following NS equation for slightly compressible fluids [90]:

$$\rho \left[\frac{\partial \vec{u}}{\partial t} + (\nabla \vec{u}) \cdot \vec{u} \right] + \nabla p = \nabla \cdot \tau + \vec{f} \quad (6.1)$$

where p is the pressure, \vec{u} is the velocity, ρ is the density, and \vec{f} is the body force due to gravity. The viscous stress tensor τ is given as

$$\tau = \mu [\nabla \vec{u} + (\nabla \vec{u})^T] - \frac{2}{3} \mu (\nabla \cdot \vec{u}) \mathbf{I} \quad (6.2)$$

where $\mu = \nu \rho$ is the dynamic viscosity, ν is the kinematic viscosity and \mathbf{I} is the identity tensor. T denotes a transposition. The velocity profile follows the continuity equation

$$\frac{\partial \rho}{\partial t} + \nabla \cdot (\rho \vec{u}) = 0. \quad (6.3)$$

The transport of water vapor is simulated with a convection-diffusion equation:

$$\frac{\partial c}{\partial t} + \nabla \cdot (-D_c \nabla c + c \vec{u}) = 0. \quad (6.4)$$

where c is the concentration and D_c is the diffusion coefficient. This coefficient has been determined experimentally, for water vapor in air, in the temperature range 9 - 177°C and at atmospheric pressure as [91]

$$D_c = 1.87 \cdot 10^{-6} \cdot T^{2.072} \left[\frac{m^2}{s} \right], \quad (6.5)$$

with T in Kelvin. The model for the dynamic viscosity, the thermal conductivity and the heat capacity at constant pressure of humid air proposed in [92] is used. The dynamic viscosity is given as

$$\mu_m = \sum_{i=1}^2 \frac{X_i \mu_i}{\sum_{j=1}^2 X_j \Phi_{ij}}, \quad (6.6)$$

where X_i is the mole fraction of air or water vapor (X_a for air and X_v for water vapor). The dynamic viscosity for air μ_a and water vapor μ_v are both obtained from

$$\mu_i = \mu_0 \left(\frac{T}{T_0} \right)^{n_\mu}, \quad (6.7)$$

where the corresponding values of μ_0 , n_μ and T_0 for air and water vapor are shown in table 6.1. Lastly,

$$\Phi_{ij} = \frac{1}{\sqrt{8}} \left(1 + \frac{M_i}{M_j} \right)^{-1/2} \left[1 + \sqrt{\frac{\mu_i}{\mu_j}} \left(\frac{M_j}{M_i} \right)^{1/4} \right]^2, \quad (6.8)$$

Table 6.1: Parameters used for viscosity calculation.

	$\mu_0 \left[\frac{\text{Ns}}{\text{m}^2} \right]$	$T_0 [\text{K}]$	n_μ
μ_a	$1.716 \cdot 10^{-5}$	273	0.666
μ_v	$1.12 \cdot 10^{-5}$	350	1.15

where M_i is the molar mas of the i 'th component. The thermal conductivity is, similarly, given as

$$k_m = \frac{\sum_{i=1}^2 X_i k_i}{\sum_{j=1}^2 X_j \Phi_{ij}}, \quad (6.9)$$

where the corresponding equation for Φ_{ij} is used. The thermal conductivity for air k_a and water vapor k_v are both obtained from

$$k_i = k_0 \left(\frac{T}{T_0} \right)^{n_k}, \quad (6.10)$$

where the corresponding values of k_0 , n_k and T_0 for air and water vapor are shown in table 6.2.

Table 6.2: Parameters used for thermal conductivity calculation.

	$k_0 \left[\frac{\text{W}}{\text{mK}} \right]$	$T_0 [\text{K}]$	n_k
k_a	0.0241	273	0.81
k_v	0.0181	300	1.35

The heat capacity at constant pressure is given as

$$C_{p,m} = Y_a C_{p,a} + Y_v C_{p,v}, \quad (6.11)$$

where Y_i is the mass fraction of the i 'th gas and each component is given as the following polynomial expression:

$$C_{p,i} = \frac{1}{M_i} (a_i + b_i T^2 + c_i R^2 + d_i^3). \quad (6.12)$$

The coefficients are provided in table 6.3. As mentioned, it is common prac-

Table 6.3: Coefficients used for the heat capacity calculation.

	$M_i \left[\frac{\text{kg}}{\text{kmol}} \right]$	a	b	c	d
$C_{p,a}$	28.97	28.11	$0.1967 \cdot 10^{-2}$	$0.4802 \cdot 10^{-5}$	$-1.966 \cdot 10^{-9}$
$C_{p,v}$	18.015	32.24	$0.1923 \cdot 10^{-2}$	$1.055 \cdot 10^{-5}$	$-3.595 \cdot 10^{-9}$

6.3. Modeling approaches

tice in the field of CFD to consider both air and water vapor as monoatomic gases and air as a one-component gas [14, 29]. The water vapor is modeled as an ideal gas and the vapor pressure is given by

$$p_v = cRT, \quad (6.13)$$

where R is the gas constant. RH can be found as

$$\Phi = \frac{p_v}{p_{sat}}, \quad (6.14)$$

where the saturated vapor pressure p_{sat} is given by equation (I.5) in the Appendix.

6.3.1.1 Coupling convection with temperature

Temperature modeling is carried out taking into account a convection-diffusion for the energy [17]:

$$\rho C_p \frac{\partial T}{\partial t} + \rho C_p \vec{u} \cdot \nabla T = \nabla \cdot (k \nabla T), \quad (6.15)$$

where T is the temperature, C_p is the heat capacity at constant pressure and k is the thermal conductivity. The natural convection inside the AquaRIUM generated by the pressure gradients, which are caused by the temperature gradients, are simulated by the Boussinesq approximation [17]. It suggests to expand ρ using the mean temperature $\bar{T} = \frac{1}{2}(T_{high} + T_{low})$:

$$\rho \approx \bar{\rho} - \bar{\rho} \bar{\beta} (T - \bar{T}), \quad (6.16)$$

where $\bar{\beta}$ is the coefficient of volume expansion evaluated at \bar{T} . Hence, the buoyancy force is given as

$$\vec{f} = \bar{\rho} \vec{g} - \bar{\rho} \bar{\beta} (T - \bar{T}) \vec{g} \quad (6.17)$$

where \vec{g} is the acceleration due to gravity.

The full coupling between the air movement and the temperature field is achieved by allowing temperature dependent coefficients, like diffusivity and viscosity, in combination with the Boussinesq approximation.

6.3.2 Free surface lattice Boltzmann modeling of condensation

The free surface LB approach is described in detail in paper B and only the extended equations will be presented in this section. The method in paper B is a further development of the earlier suggested approach described in [79].

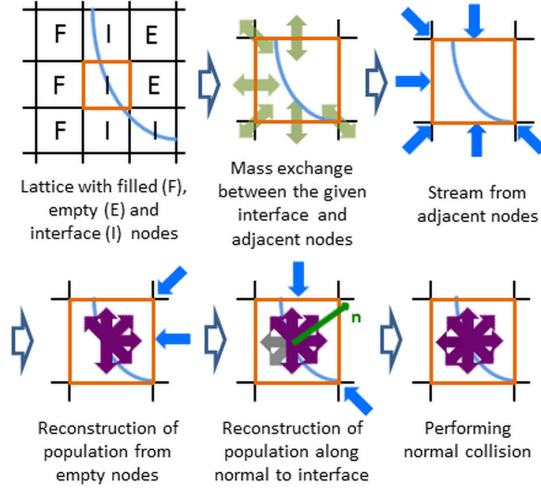


Fig. 6.4: The procedure used for the surface handling.

The main idea behind the free surface modeling used here, is to track the mass movement. The computational grid is divided into three node types; fluid (F), interface (I) or empty (E). The process for the surface handling is illustrated in figure 6.4.

In the free surface model the gas phase is assumed to have a negligible effect on the fluid flow in the film. Therefore, surface tension and shear stress at the liquid–vapor interface are discarded. Moreover, the contact angle at the top of the film have been shown to have a negligible effect when considering film condensation [93] which justifies the simplification. The new extension of the procedure is the introduction of mass transfer between the vapor and the liquid at the interface. It is, thus, possible to model condensation and evaporation at liquid–vapor interfaces with the free surface LB method.

In the model the empty nodes are never addressed. At fluid nodes the streaming step and, therefore, also the mass update are unchanged. For interface nodes the mass update is done according to

$$m(\vec{x}, t + dt) = m(\vec{x}, t) + \sum_{i=1}^{n_d} \Delta m_i^k(\vec{x}, t + dt) + A J dt, \quad (6.18)$$

where $k \in \{I, F\}$, x is the node coordinate, t is time, dt is the time step and J is the magnitude of the condensation flux. A is the area of the surface at the given node. This area, which for 2D simulations correspond to a line, is found by assuming that the area of the interface can be approximated by a right-angled triangle. Δm_i is the mass streaming from the neighboring nodes. The condensation flux couples the energy equation to the mass flux

6.3. Modeling approaches

at the interface. The energy conservation at the surface implies

$$k_l \vec{\nabla} T|_{interface} = k_g \vec{\nabla} T|_{interface} - \vec{J} \Delta h_{vap}, \quad (6.19)$$

with k_g to be the thermal conductivity of the gas and Δh_{vap} as the latent heat of condensation. The gradients are approximated with the finite difference method.

The temperature is modeled as a passive scalar and simulated using a second lattice given as [94]

$$g_i(\vec{x} + \vec{c}_i dt, t + dt) = g_i(\vec{x}, t) + 2\beta_T (g_i^{eq}(T, \vec{u}) - g_i(\vec{x}, t)), \quad (6.20)$$

where the thermal diffusivity

$$D_T = c_s^2 \left(\frac{1}{2\beta_T} - \frac{1}{2} \right) dt. \quad (6.21)$$

The temperature is obtained from $T = \sum_{i=1}^{n_d} g_i$ and the equilibrium function g_i^{eq} is

$$g_i^{eq}(T, \vec{u}) = TW_i \left(1 + \frac{\vec{c}_i \cdot \vec{u}}{c_s^2} \right). \quad (6.22)$$

As shown in section 8.2, the source of numerical instability does not originate from the temperature field which is why the LBGK relaxation is sufficient.

The fluid flow is simulated according to the entropic LB framework described in section 4.2, where the entropy evaluation is used to increase numerical stability. The main source for numerical instability is found to be the interface, which will be highlighted in the section below.

6.3.3 Finite volume modeling of diffusion

In paper D the finite volume (FV) approach is used to model water vapor concentration profiles in enclosures. This approach is chosen because it inherently conserves the simulated property [14]. FV method will now be briefly presented for modeling of diffusion.

The diffusion equation for the concentration c reads

$$\frac{\partial c}{\partial t} = \nabla \cdot (D_c \nabla c), \quad (6.23)$$

which equals to zero for steady state. As in any numerical scheme, the starting point in FV is the discretization of the computational domain. The concept of the FV method is to consider a control volume, as illustrated in figure 6.5, in which the flux of the property that enters the control volume must also leave the control volume. That is of course true if there is no source or sink of the property in the control volume.

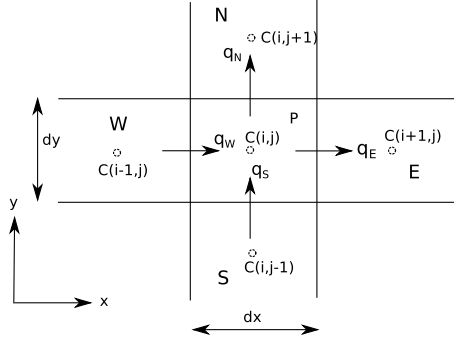


Fig. 6.5: Schematic of the FV discretization of the computational domain.

The flux accountant for control volume cell P , shown in figure 6.5, for the steady-state case is given as

$$q_W - q_E + q_S - q_N = 0, \quad (6.24)$$

where q_W is the flux of c streaming from the "west" cell W to the cell P and q_E is the flux of c leaving P towards "east" cell E . Similarly fluxes q_S and q_N are defined. These fluxes can be approximated in many ways. Here, the central difference method is used, which has a second order accuracy [14].

Using this approach the flux at the west interface can, for example, be written as

$$q_W = D_c A_W \left. \frac{\partial c}{\partial x} \right|_W, \quad (6.25)$$

where A_W is the area of the interface. For 2D case shown in figure 6.5 $A_w = dy$. Using the central difference the gradient is now approximated as

$$\left. \frac{\partial c}{\partial x} \right|_W \approx \frac{c(i, j) - c(i-1, j)}{dx}. \quad (6.26)$$

In the similar way all the fluxes can be calculated with the concentration at the node points:

$$\begin{aligned} q_W &= D_c dy \frac{c(i, j) - c(i-1, j)}{dx}, & q_E &= D_c dy \frac{c(i+1, j) - c(i, j)}{dx}, \\ q_S &= D_c dx \frac{c(i, j) - c(i, j-1)}{dy}, & q_N &= D_c dx \frac{c(i, j+1) - c(i, j)}{dy}. \end{aligned}$$

To obey equation (6.24) the successive-over-relaxation (SOR) method is used because of an easy implementation compared to convergence rate. For a detail discussion of various iteration procedures, see [14]. As in any iteration

6.3. Modeling approaches

procedure an initial guess for the approximate solution is provided. At iteration k the SOR method gives rise to

$$c^k = \omega \bar{c}^k + (1 - \omega)c^{k-1}, \quad (6.27)$$

where ω is the relaxation factor and \bar{c}^k is the concentration obtained by a Gauss-Seidel (GS) iteration. The GS method provides the guess \bar{c}^k based on the current information in the computational domain and is therefore a mixture of already updated call and cells from the previous iteration. This is in contrast to the Jacobi procedure, where all the next iterations are based on the previous iterations [14].

This concludes a numerical framework allowing for modeling of water vapor distributions in simple enclosures.

7. Humidity and temperature evolution in AquaRIUM

7.1 Investigation of thermodiffusion of water vapor in air

As a first step towards complex models, it is investigated whether temperature gradients typical for power electronic enclosures would give rise to any significant thermodiffusion of water vapor in the air. To study this, it is tested if any thermodiffusion of water vapor in air would be measurable in the AquaRIUM and also if the developed CFD model would be in agreement with the experimental data.

Before conducting the experiments the setup was disassembled and heated up to 100°C for 30 min. This was done in order to remove water absorbed at the inner surfaces of the AquaRIUM. After the heating treatment the setup was assembled under clean-room conditions and sealed in order to be airtight. An experiment was conducted by placing a sensor relatively close to the heating plate inside the AquaRIUM. The plate with the Peltier element was gradually heated from 20°C to 60°C over a period of 80 min.

In the model, the pressure diffusion is discarded because $\Delta T/T \gg \Delta p/p$. The initial measurements in the setup are used as homogeneous initial conditions for the simulation. The diffusion is modeled according to equation (2.63) with $\nabla \ln p = 0$ and the material properties are considered in the way described in section 6.3. A homogeneous water vapor distribution corresponding to the initially measured RH is assumed as the initial condition for the simulations. A model output of the water vapor concentration profile with natural convection indicated by arrows is shown in figure 7.1. It is found that according to the model, some movement of the water vapor due to the thermal gradients is present.

However, the evolution of water vapor concentration obtained by the simulations is found to be different from that experimentally measured. The

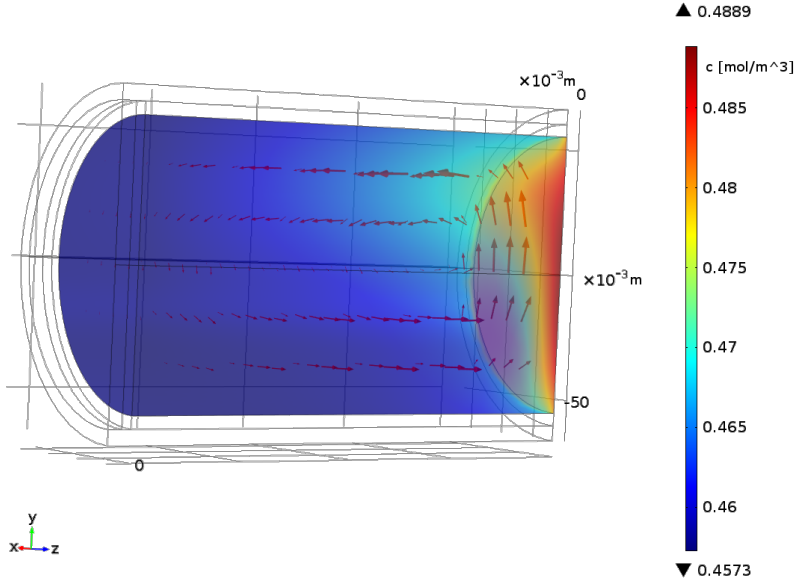


Fig. 7.1: Snapshot of the simulated water vapor concentration in the AquaRIUM 80 min after start of the heating. Color scale shows water vapor concentration.

measurements are done at different locations in the AquaRIUM. In figure 7.2 one can see the dependence for one of them, in particular for the case when the sensor is positioned close to the main axis of the cylinder and about 4 cm from the heating plate. The experiments show much higher increase of water concentration with time of heating (from 20 to 60°C) compared to the simulations. Most probably such a difference is related to vapor outgasing from the rubber gaskets and also from the inner walls of the cylinder despite the pre-baking. Sensors at other positions shows very similar tendencies. Contrary to the vapor concentration, the simulated transient development in temperature shows fairly good agreement with the measurements (see figure 7.3). The deviation is within five percents. To test if moisture release from the gaskets and other surfaces during the heating is the real reason for the observed increase in water vapor concentration the temperature and vapor concentration are logged during the heat up and cool down. The cool down is carried out from 60°C to 20°C over a period of 80 min right after the heating. Since the release of water vapor occurs on a faster time scale than re-absorption of the moisture there must be more moisture in the air after such heating/cooling cycles. The vapor concentration outside the AquaRIUM is also monitored to ensure that no moisture diffuses through the gaskets inside the setup. The results of measurements can be seen in figure 7.4

7.1. Investigation of thermodiffusion of water vapor in air

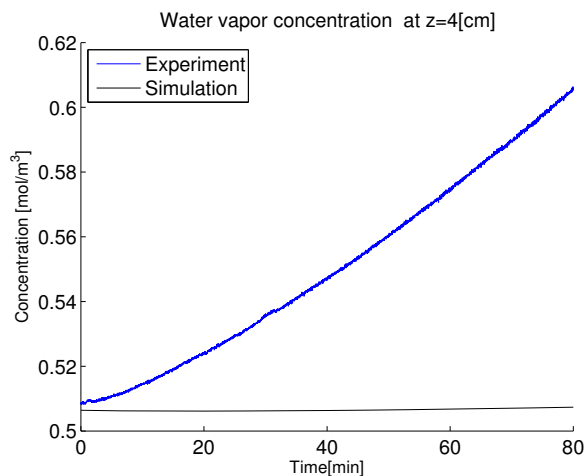


Fig. 7.2: Comparisons between modeled and measured water vapor concentration as a function of time.

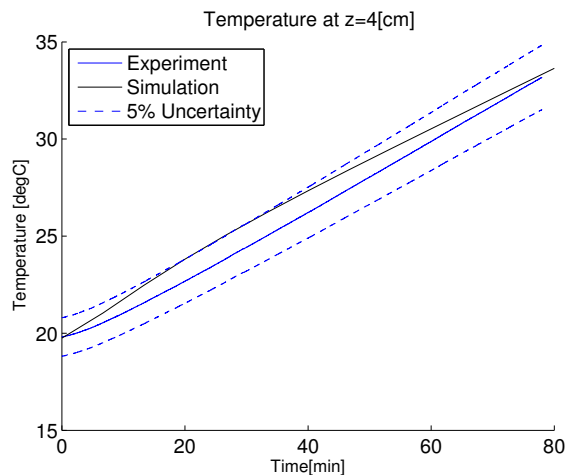


Fig. 7.3: Comparisons between modeled and measured temperature as a function of time.

showing the temperature and water vapor concentration evolution over the time in AquaRIUM. For comparison, the water vapor concentration just outside the setup is also presented demonstrating that there is not correlation with the evolution inside thus ensuring no outward diffusing moisture. It can be seen that the vapor concentration is increased by almost 10% during the heating step and then steadily decrease under the cooling. Thus, in practice the effect of thermodiffusion can be neglected because other mechanisms like water vapor outgassing from walls and other parts inside an enclosure will be completely dominating over the humidity evolution due to diffusion.

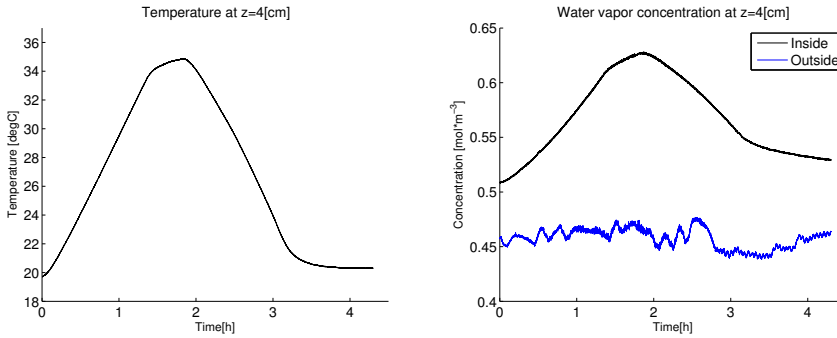


Fig. 7.4: Comparisons between modeled and measured temperature (left) and water vapor concentration (right) as a function of time.

7.2 Humidity distributions affected by presence of liquid water

The material presented in this section can be found in more detail in paper A.

This study concerns modeling of humidity distributions affected by freely exposed water surfaces. The motivation for the study originates from power electronic enclosures introduced in harsh environments which may exhibit moisture diffusion through the packaging. Due to temperature variations, the moisture might condensate and small water pools can form at the bottom of the enclosure. Completely hermetic enclosures can be expensive and it is therefore of interest to design enclosure which can withstand situations where water condensation occurs. Methods for predicting the local humidity distribution are of interest because they may act as design tools for packaging. This tool may, thus, be used to design cabinets exposed to such stress factor as humidity.

Experimentally, a water vessel is introduced into the AquaRIUM and the time

7.2. Humidity distributions affected by presence of liquid water

evolution of the RH at various locations is logged. The sensor positions are shown in figure 7.5. The opening is closed by a napkin after brining the vessel inside.

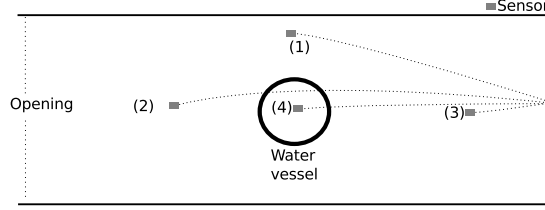


Fig. 7.5: Schematic top view of the experimental setup.

The release of water vapor from the water surface is modeled by SRT (see chapter 3 for details) under the assumption that the temperature differences between the vapor and liquid can be discarded. Under this assumption the SRT expressions, equations (3.41) and (3.33), reduce to

$$J_{SRT} = 2K_e \sinh \frac{\Delta S}{k_B}, \quad (7.1)$$

with

$$\frac{\Delta S}{k_B} = \ln \left(\frac{p_{sat}(T_l)}{p_v} \right) + \frac{V_m}{k_B T_l} (p_l - p_{sat}(T_l)). \quad (7.2)$$

The transient description of the flux of vapor released from the liquid water is obtained using a number of sequent steady-state time steps.

Two water vessel of different sizes are used and the measured RH time evolutions at the four locations can be seen in figure 7.6.

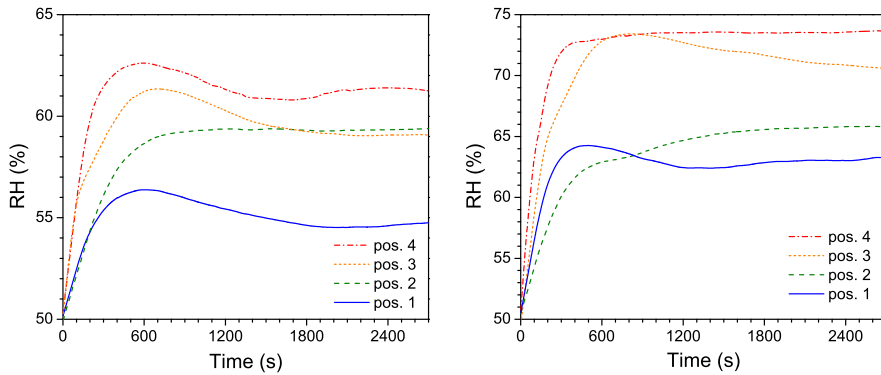


Fig. 7.6: Change of RH with time for different sensor positions in the setup with the small vessel (left) and the large vessel (right).

It is seen that bumps are occurring roughly 600s into the experiments after

which the levels become stationary. In the first model the only transport mechanism considered is diffusion. The comparisons between the measurements and the diffusion model can be seen in 7.7.

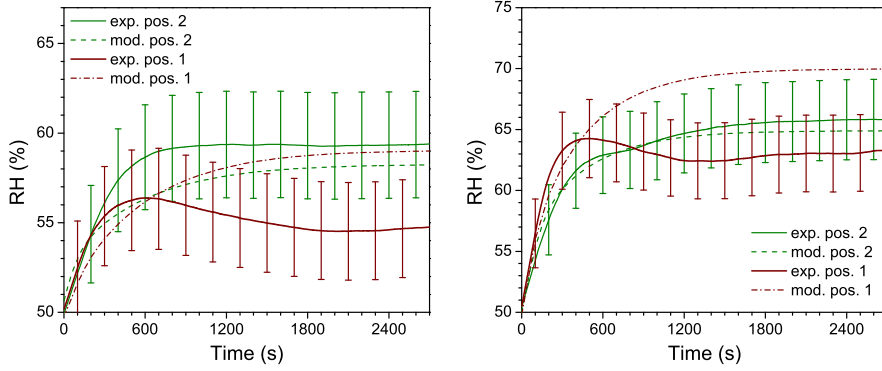


Fig. 7.7: Comparisons of the modeled and measure RH with time for sensor position 1 and 2. (left) comparisons for the small vessel and (right) the large vessel.

From figure 7.7 it is clear that sheer diffusion does not fully capture the time evolution of the RH distribution. The model, thus, needs to include convection. The airflow from the surroundings will inducing an airflow inside the setup, which needs to be taken into account. This is done with a downwards velocity boundary condition \vec{u}_0 at the opening of the AquaRIUM. It is found that when $u_0 \sim 1 \text{ cm/s}$ the model coincided with the experiments independent of water vessel size or sensor location. No direct measurement of \vec{u}_0 was possible but it is indirectly inferred by comparing the model with experiments. From the model it is found that a small velocity at the opening of the AquaRIUM lowers the overall RH level. Increasing the boundary velocity further, gives rise to bumps in the time evolution of the RH. However, the simulated bumps are at a larger time scale than the experimentally observed. It is, thus, found that the bumps in the RH curves can only be qualitatively explained by air disturbances from the introduction of the water vessel at the beginning of each experiment. Experimentally, the convection at the opening is limited by a linen napkin (Valusorb from Berkshire) attached at the opening after the introduction of the water vessel. It must, however, be expected that a small amount of air disturbances from the surroundings will enter AquaRIUM, justifying the velocity boundary condition.

A snapshot of the modeled humidity profile with the large vessel after 4000s. can be seen in figure 7.8 and as shown below the model agrees very well with experiments when including convection.

The developed model also allows to calculate the flux of evaporating water. Experimentally, the flux was calculated from the measurements of water

7.2. Humidity distributions affected by presence of liquid water

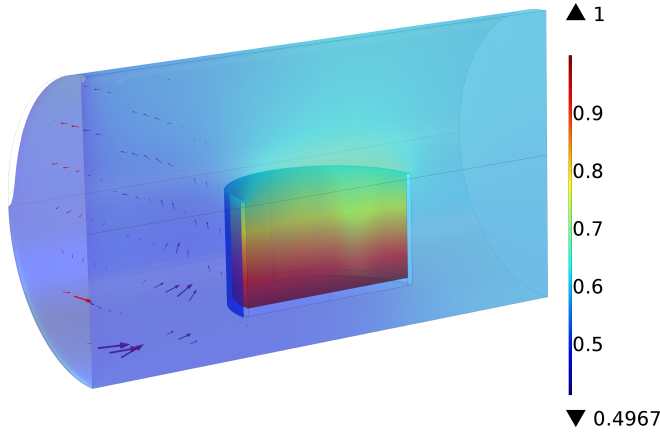


Fig. 7.8: Simulated RH after 4000 s with $u_0 = 1\text{ cm/s}$ for the case of the setup with the large water vessel. Color scale shows RH and the arrows indicate air flow.

weight decrease in a vessel over times between 21-24 hours. The measured fluxes and those modeled are shown in table 7.1.

Table 7.1: Calculated fluxes and experimentally measured fluxes.

	Calculated flux	Measured flux
Small vessel	$1.17 \cdot 10^{-4} \frac{\text{mol}}{\text{s} \cdot \text{m}^2}$	$(3.15 \pm 0.25) \cdot 10^{-4} \frac{\text{mol}}{\text{s} \cdot \text{m}^2}$
Large vessel	$0.89 \cdot 10^{-4} \frac{\text{mol}}{\text{s} \cdot \text{m}^2}$	$(2.32 \pm 0.1) \cdot 10^{-4} \frac{\text{mol}}{\text{s} \cdot \text{m}^2}$
Flux ratio	1.31	1.36 ± 0.05

As seen, there is a difference between the modeled and the measured fluxes. However, the experimental and simulated values demonstrate the same order of magnitude and the simulated and measured ratio values (flux for small vessel versus one for large vessel) become the same within the standard deviations interval. Taking into account that the fluxes are extremely small, one can conclude about good agreement between the simulations and the experiments since the order of magnitude of the fluxes are the same. It must be noticed that in both model and experiment the flux is greater for the small vessel. This fact relates to the change in the configuration of the setup. The larger vessel takes up more space in the cylinder, which changes the distribution of the surrounding humidity and the flux will thereby be slightly reduced.

As stated in paper A a set of experiments is conducted where the water vessel is filled with a plastic pipe from outside of the AquaRIUM instead of introducing the entire vessel. This procedure is used to minimize air disturbances inside the setup. The comparisons between the model and experiments are

shown in figure 7.9. Sensor position (1) (beside the vessel) and (3) (behind the vessel) is chosen for the figure because the largest bumps are observed at these locations. It can be seen, that no bumps occur when the liquid water is introduced by a pipe. The model is in very well agreement with the final RH level but also agrees with the time evolution of the RH. The origin of the bumps are, thereby, concluded to be due to air disturbances associated with the movement of the water vessel in the beginning of the experiment.

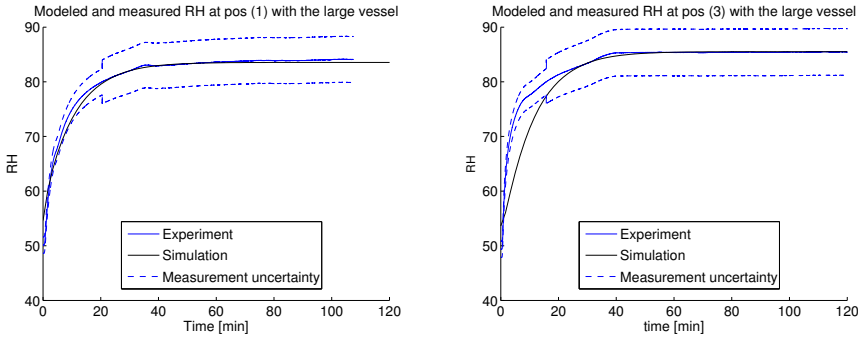


Fig. 7.9: Comparisons between modeled and measured RH at pos (1) and (3) with the water introduced by a pipe as a function of time.

A modeling approach for predicting the local humidity distribution affected by exposed water surfaces is, hereby, presented. Also, according to this study, the temperature differences at the interface due to evaporation can be neglected at this spacial scale and in this temperature regime. A further study could, however, be conducted where the effect of including the temperature difference at the interface is investigated.

7.3 Natural convection in the AquaRIUM

The material presented in this section is based on paper C.

As mentioned earlier, a transport mechanism for moisture can be natural convection. This can happen when the operating electronics in an enclosure heats the local environment. This gives rise to pressure gradients due to the thermal gradients. The pressure gradients enables convective movement of the air. Since most enclosures are not completely hermetic, air can move through the openings, thus, also transporting moisture. Transport of air from and into an enclosure due the heating by the operating electronics is often referred to as breathing.

Here it is investigated whether breathing effects of AquaRIUM can be modeled with the Boussinesq approximation. The study concerns how to compare an experimentally measured mass flux at the opening of the AquaRIUM with

7.3. Natural convection in the AquaRIUM

a modeled flux. Both fluxes are averaged over a so-called heat profile which is applied by the Peltier element. Heating profiles will be explained later. Experimentally the mass flux is estimated by placing a cylindrical wet sponge into the AquaRIUM, waiting until the air in the setup is saturated with humidity and weighing the sponge. Then a given heating profile is applied and the sponge is weighed again. The sponge is weighed by attaching one end of the steel wire to a scale and the other end is attached to the Petri dish where the sponge lies. See figure 6.3 for better understanding of the experimental configuration. In this study several opening radii are used.

Two heating profiles are applied in this study. Both of them are shown in figure 7.10. The first heating profile mimics a real world heating situation from an electronic device. However, to get a more controlled system the second profile is introduced.

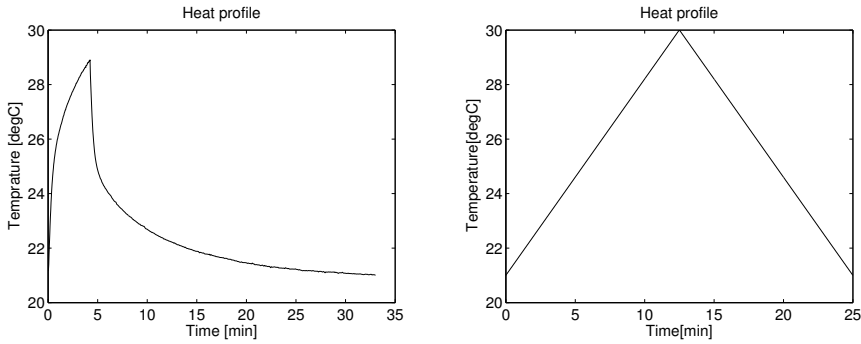


Fig. 7.10: (Left) The first heating profile as a function of time. (Right) The second heating profile.

The 2D axis symmetric model is set up with COMSOL multiphysics with the buoyancy force as explained in section 6.3. At the sponge location, a relative humidity of 100% is used and at the opening the relative humidity is set to 50%. The heating profiles are loaded into the software and applied at the bottom of the system as a boundary condition.

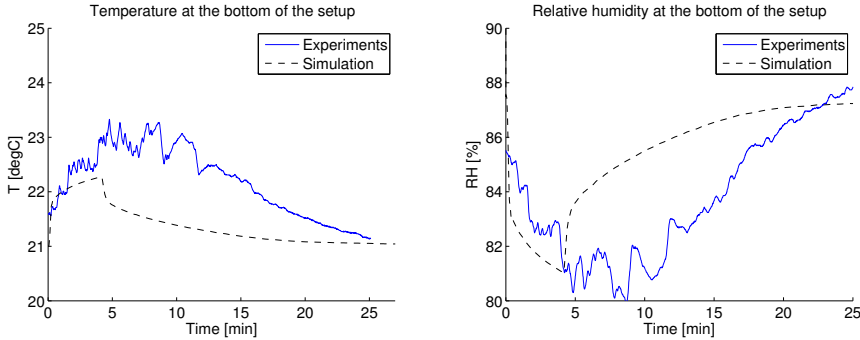
The average modeled and measured vapor dissipation for the first heating profile are shown in table 7.2. It is seen that the modeled and measured vapor dissipations are within the same order of magnitude. However, it is also noticed that simulated and experimental values start significantly deviate for the increasing opening radii. This difference between the model and experiments for the opening with radius 2 cm is believed to be due to convective disturbances from the test setup surrounding.

Comparing temperature and RH evolutions between the model and experiments also shows some deviation. This is demonstrated in figure 7.11 where the temperatures and RHs are compared at the bottom of AquaRIUM.

From the figure it is clear that the temperature response is faster in the model

Table 7.2: Calculated and measured dissipation of vapor for first heating profile.

Opening radius	Modeled dissipation	Measured dissipation
0.5 [cm]	0.0031[mol]	0.0083 ± 0.0190 [mol]
1 [cm]	0.0033[mol]	0.0087 ± 0.0021 [mol]
2 [cm]	0.0037[mol]	0.3110 ± 0.0196 [mol]

**Fig. 7.11:** Comparisons between the model and measurements for the temperature (left) and the RH (right) as a function of time.

than as seen in the measurements. Also, the maximum temperature is underestimated in the model. This is observed for all comparisons done between the model and measurements. An explanation for the deviation could be that the Boussinesq approximation does not capture the full effect of the natural convection. More convection inside the setup yields higher heat fluxes at the bottom because it will lower the temperature of the air just above the Peltier element. This will give rise to a more smeared temperature peak. Another reason for the underestimated temperature in the model can be air disturbances from the surroundings of the experimental setup. This air disturbance will introduce unintended air movements inside the AquaRIUM and, as explained above, gives rise to higher heat fluxes at the bottom of the setup. To test this assumption, experiments with smaller opening radii are conducted. Additionally, the second, more controlled, heating profile is used.

The modeled and measured average dissipations of vapor for the second series of experiments are shown in table 7.3 demonstrating much better agreement compared to the first heating profile. Thus, it is convincing that the deviations between the simulations and experiments are most probably related to uncontrolled air disturbances outside the setup.

To further eliminate air disturbances inside the AquaRIUM a 10 cm long glass tube with an inner radius of 0.2 cm is attached on top of the opening as a final set of experiments. As seen in table 7.4 the very good agreement between the simulation and the experiments is achieved. This further confirms that the

7.3. Natural convection in the AquaRIUM

Table 7.3: Calculated and measured dissipation of vapor for the second heating profile.

Opening radius	Modeled dissipation	Measured dissipation
0.25 [cm]	0.0021[mol]	0.00150 ± 0.00067 [mol]

deviations between the model and experiments are due to air disturbances caused by air movement outside the setup.

Table 7.4: Calculated and measured dissipation of vapor for the linear heat profile in the third series of experiments with a 10 cm long glass tube mounted on top of the AquaRIUM.

Opening radius	Modeled dissipation	Measured dissipation
0.2 [cm]	$1.07 \cdot 10^{-4}$ [mol]	$1.500 \cdot 10^{-4} \pm 6.7 \cdot 10^{-5}$ [mol]

In this section it is, thus, demonstrated how natural convection or breathing in enclosures can be modeled with the Boussinesq approximation. It is illustrated how to model air streams going from an enclosure to its surrounding. Furthermore, an experimental procedure is described to measure the water vapor release due to a heat-up from operating electronics.

8. Free surface entropic lattice Boltzmann method

This chapter describes the developed free surface entropic lattice Boltzmann (FSELB) method and the results obtained on modeling of thin water layer, so-called film condensation. In order to benchmark the FSELB model, a short introduction into the film condensation topic is given in the beginning of the chapter. Generally, the material of this chapter is presented along with paper B.

8.1 Fundamentals of film condensation

As mentioned, condensation of water can occur in power electronic enclosures for example due to "breathing modes", one of which is described in the previous chapter. Another widely occurring case is exposure of the electronic packaging to a so-called cold spot, lowering the local temperature inside the enclosure and leading to a condensation. Accurate models for predicting condensation is, thus, of interest in order to design robust packaging against humidity.

Wilhelm Nusselt pioneered the field in 1919 by developing analytic expressions for, among others, the velocity profile and the heat transfer in a condensing film flowing downwards a vertical wall [95]. The so-called Nusselt model is derived in detail in appendix I.2. The system that Nusselt considered and also that is considered here, is shown in figure I.2.

In such a system, condensing film flows are characterized by the film Reynolds number

$$Re_f = \frac{4\dot{m}_{z=L}}{\mu_l}, \quad (8.1)$$

where $\dot{m}_{z=L}$ is the mass flow at the bottom of the film with the length L and μ_l is the dynamic viscosity of the liquid condensate. The Nusselt model has been experimentally verified for $Re_f \lesssim 33$ [96]. At $Re_f > 33$ the film becomes more wave-like and velocity profile starts to deviate from a laminar flow

because of a build-up of inertia in the film. For film flows where $Re_f > 33$ empirical models were developed [97, 98]. However, at the laminar regime, where the Nusselt model applies, the thickness of the film is given as

$$\delta(z) = \left[\frac{4k_l\mu_l(T_d - T_0)z}{\Delta h_{vap}\rho_l(\rho_l - \rho_g)g} \right]^{1/4}, \quad (8.2)$$

with k_l to be the thermal conductivity of the liquid, T_0 to be the wall temperature, T_d to be the temperature at the interface between the gas and liquid phases, Δh_{vap} to be the latent heat of condensation, ρ_l to be the density of the liquid, ρ_g to be the density of the gas, and g to be the acceleration due to gravity. The velocity profile v is given as

$$v = \frac{(\rho_l - \rho_g)g}{\mu_l} \left[y\delta - \frac{y^2}{2} \right] \quad (8.3)$$

and the mass flow rate \dot{m} is, according to Nusselt, given as

$$\dot{m} = \rho_l \frac{(\rho_l - \rho_g)g}{3\mu_l} \delta^3. \quad (8.4)$$

The local heat transfer coefficient h is given as $h = k_l/\delta$ which leads to the average heat transfer coefficient as following:

$$\bar{h} = \frac{4}{3} \frac{1}{4^{1/4}} \left[\frac{k_l^3 \Delta h_{vap} \rho_l (\rho_l - \rho_g) g}{\mu_l (T_d - T_0) L} \right]^{1/4} \approx 0.943 \left[\frac{k_l^3 \Delta h_{vap} \rho_l (\rho_l - \rho_g) g}{\mu_l (T_d - T_0) L} \right]^{1/4}. \quad (8.5)$$

The non-dimensional Nusselt formula of the averaged heat flux:

$$H_f = \frac{\bar{h}}{k_l} \left[\frac{\mu_l^2}{\rho_l (\rho_l - \rho_g) g} \right]^{1/3} = 1.47 Re_f^{-1/3}. \quad (8.6)$$

The film flow and heat transfer of steady film condensation on hydrophilic surfaces can be characterized by the following two dimensionless numbers:

$$Pr = \frac{\nu}{D_T}, \quad Ja = \frac{c_p(T_d - T_0)}{\Delta h_{vap}}, \quad (8.7)$$

which is the Prandtl and Jakob number, respectively, with c_p to be the specific heat at constant pressure. The Prandtl number is a material constant and the Jakob number is the ratio of the sensible heat of the film and the latent heat of the vapor. Thus, for a fixed Pr the film thickness will increase with the Jakob number since the energy flux at the interface increases.

8.2 Simulation results

As mentioned in section 6.3.2, the developed FSELB model includes the mass flux at vapor-air interfaces, allowing for evaporation and condensation simulations. This section demonstrates how the FSELB can be used for film condensation modeling.

The numerical set up of the simulations can be found in detail in paper B. To illustrate that a range of materials can be modeled, two simulations with $Pr = 7$ and $Ja = 0.185$, and $Pr = 0.8$ and $Ja = 0.4$ are done and compared with the Nusselt model. Earlier developed LB condensation models only apply where $Pr \sim 1$ [93]. Thus, FSELB shows an obvious advantage. The film thickness modeled by the developed FSELB method and the classic Nusselt model are compared in figure 8.1. It is seen that the results for the simulation of thickness for the condensing films are very much consistent.

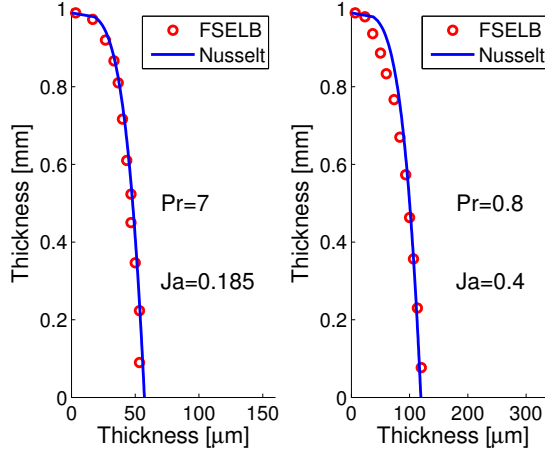


Fig. 8.1: Comparisons of film thickness predicted by FSELB simulation and Nusselt formula.

The z-components of the velocities at L modeled by the two models are shown in figure 8.2 along with the film Reynolds numbers. It can be seen that both models agree well for low length values. However, the velocities predicted by the FSELB model are found to be smaller than those calculated by the Nusselt model and this difference increases with the velocity rise. Actually, this is expected behavior because the FSELB method takes into consideration the effects of inertia forces which lowers the velocity.

Similarly, the dimensionless temperature $\theta = \frac{T-T_0}{T_0-T_d}$ profile at L is shown in figure 8.3. Both models predict a linear profile and they are in good agreement.

To prove that the temperature and velocity profiles simulated by the Nusselt

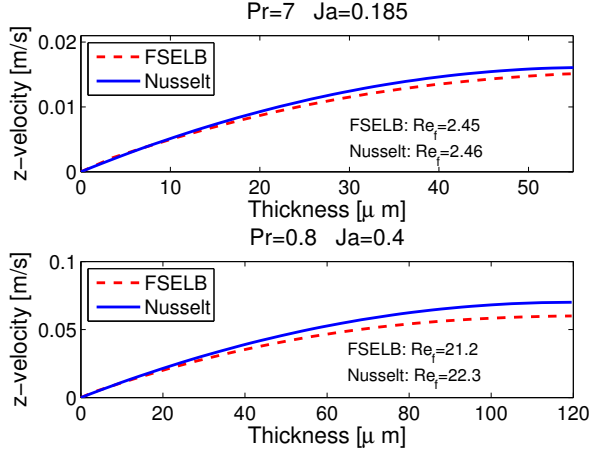


Fig. 8.2: Comparisons of z-components of the velocity predicted by FSELB simulation and Nusselt formula.

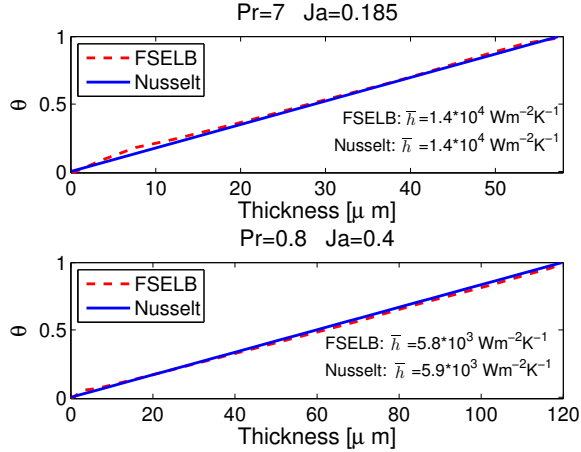


Fig. 8.3: Comparisons of dimensionless temperature profiles predicted by FSELB simulation and Nusselt formula.

8.2. Simulation results

and the FSELB models are in agreement, contour plots for the two simulations are made. These plots are shown in figure 8.4 and 8.5. Again, the FSELB model agrees with the Nusselt model.

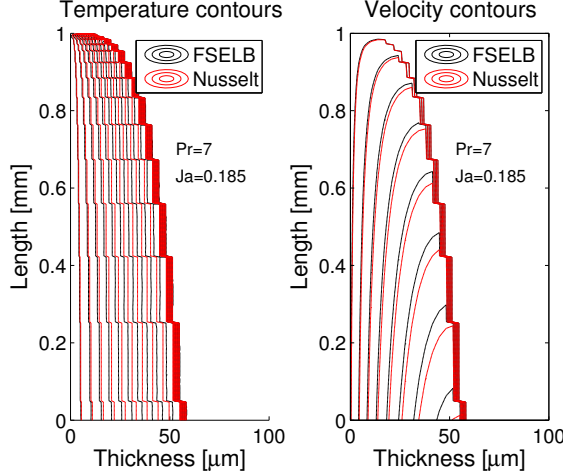


Fig. 8.4: Comparisons of temperature and velocity contour profiles predicted by FSELB simulation and Nusselt formula with $Pr = 7$ and $Ja = 0.185$.

Besides being able to simulate film condensation for a wide range of materials, the developed FSELB model allows to simulate film flows beyond the laminar regime. With enough resolution the wave-like behavior of the film can be simulated. To illustrate this two simulations were conducted with same input parameters and initial conditions but with different resolutions, namely 600×600 and 3000×3000 grids. The simulations are carried out with $Pr = 0.5$, $Ja = 2.5$ and $L = 200\text{mm}$. A snapshot of both fluid fractions $\epsilon = m/\rho$ where $Re_f = 94.65$ can be found in figure 8.6. It is seen that the film becomes wave-like when simulated with high enough resolution. To verify the FSELB model beyond the laminar regime it is compared with the empirical models [97, 98]. The comparisons of the non-dimensional averaged heat versus film Reynolds number are shown in figure 8.7. It can be seen, that the simulations using FSELB model show a reasonable agreement with the two empirical models for the range of used film Reynolds numbers.

Finally, the entropic realization of the free surface framework must be justified. It serves as a stability mechanism. A snapshot of the α -profile of a condensation film flow where $L = 1.5\text{mm}$, $Pr = 0.8$ and $Ja = 2.4$ is shown in figure 8.8. To visualize the film, the fluid fraction ϵ is also shown in figure 8.8. This simulation was proven to be unstable with the standard LBGK but it is stable using the entropic model. It is seen, that the entropic estimations are activated at this snapshot mainly in two places at the surface. Furthermore,

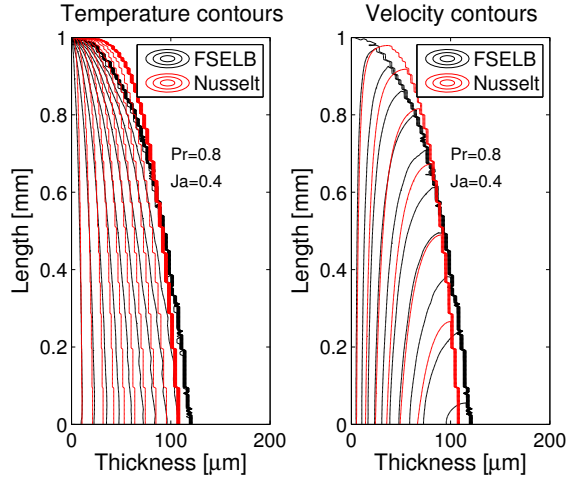


Fig. 8.5: Comparisons of temperature and velocity contour profiles predicted by FSELB simulation and Nusselt formula with $Pr = 0.8$ and $Ja = 0.4$.

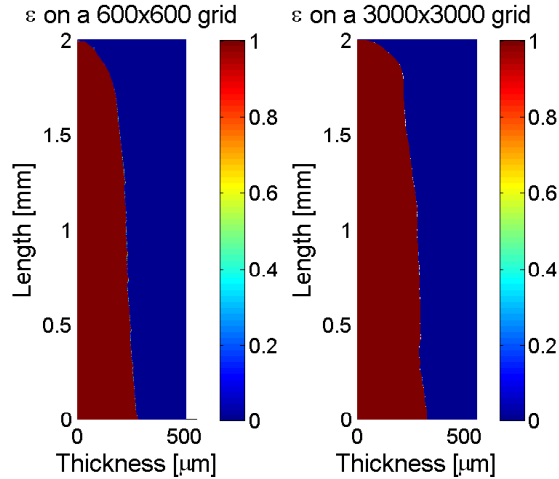


Fig. 8.6: Comparison of fluid fraction ϵ profiles at a snapshot where $Re_f = 94.65$. The simulations are carried out with two different resolutions shown in the panels.

8.2. Simulation results

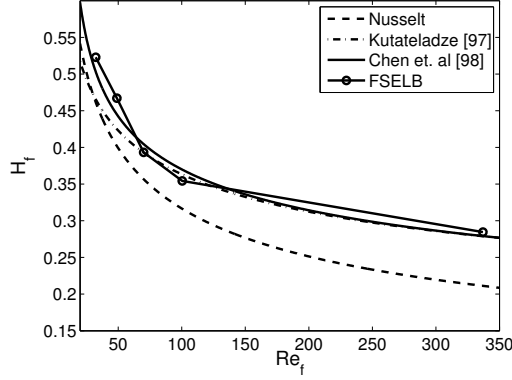


Fig. 8.7: Comparison of non-dimensional averaged heat fluxes predicted by the various models for the given range of film Reynolds numbers.

the α values cover a range of 1.8 - 2.05. This range signifies the need for the entropic stabilization.

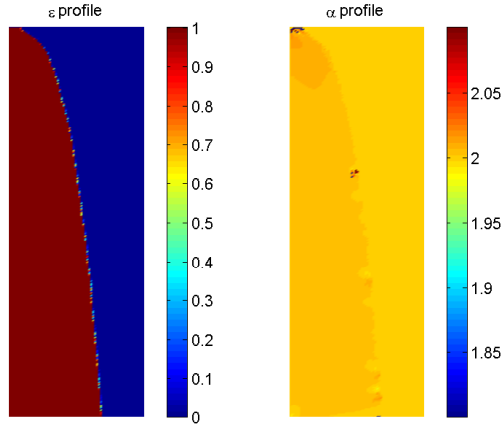


Fig. 8.8: A snapshot of the fluid fraction ϵ and α -profile of a condensation film flow where $L = 1.5mm$, $Pr = 0.8$ and $Ja = 2.4$.

Thus, by this work the free surface LB framework has been extended with the entropic LB method yielding new FSELB method demonstrating greater numerical stability. Furthermore, it is demonstrated how the free surface framework can be extended for the evaporation-condensation problem. The developed FSELB model displays good agreement with empirical and analytic models for film condensation, both for laminar flows and also beyond

the laminar regime. Thus, the model can be used for prediction of water condensation on the wall of enclosures for electronics adding one more powerful tool into the set of instruments for climatic simulations.

9. Humidity-related reliability assessment

Throughout the thesis various climatic scenarios for electronic enclosures have been considered. This chapter aims to illustrate how these different scenarios and the developed modeling approaches can contribute into prediction of reliability. The material presented here is based on paper D. A model enclosure with a simple geometry is suggested for the simulations and it is shown in figure 9.1. This geometry represents a box with an opening and with a small water pool formed at bottom for example due to condensation. This water can evaporate giving rise to a high humidity inside the enclosure but moisture can also move out/in through the opening.

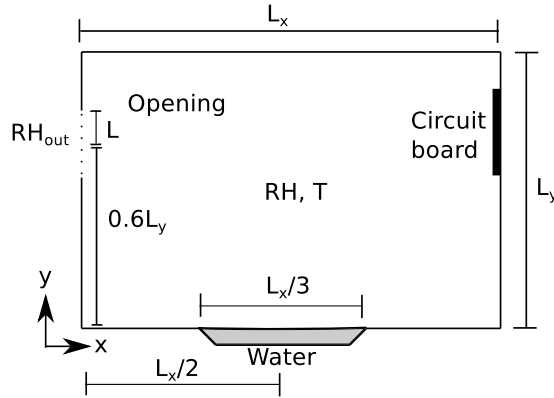


Fig. 9.1: Schematic of the model enclosure.

The study is limited to steady-state analysis where the only transport mechanism considered is diffusion. The water vapor profile is simulated by the finite volume method described in section 6.3.3. This analysis is carried out for the simple geometry in order to keep the focus on the reliability assessment method.

As mentioned earlier, most corrosion mechanisms are such that when the RH level rises above a limit the corrosion will begin and the electronics will eventually fail. Therefore, the failing criterion is put to be a certain RH level RH_f at the circuit board location.

Similar to the approach presented in section 7.2 the temperature gradients are neglected. Equation (7.1) is used to model the magnitude of the water vapor flux from the water surface in the direction orthogonal to it. Due to variations in production or usage of the item, certain quantities have uncertainties when estimating if the failing criterion is reached. Here, these quantities are the half-width of the opening L , temperature T and RH at the opening RH_{out} . The parameters for the stochastic variables are shown in figure 9.1.

Table 9.1: Simulation parameters for stochastic variables.

Variable	Distribution	Mean	Std. dev.
L	Log Normal	$0.013500[L_x]$	$1.35 \cdot 10^{-6} [L_x]$
T	Normal	303 [K]	10 [K]
RH_{out}	Normal	0.60	0.02

At the walls of the enclosure no-flux boundary conditions are applied. For the opening the following concentration boundary condition is used:

$$c_0 = RH_{out} \frac{p_{sat}}{RT}. \quad (9.1)$$

The iteration approach is an over relaxed Gauss-Seidel scheme with a relaxation factor of $\omega = 1.9$ [14]. The water vapor flux at the water-air interface is calculated using the Newton-Raphson method. As explained in chapter 5, the probability of failure P_f can be well-approximated by Monte Carlo sampling of the random variables. For this framework, equation (5.3) is used to evaluate P_f .

The computational domain is discretized using 100 control volumes of equal size in each direction. Every length in the x -direction is normalized to L_x and likewise for the y -direction. Finally, the convergence criterion for the diffusion problem is set so that on average the change in the water vapor concentration at the control volumes is $\Delta c < 10^{-4} \text{ mol} \cdot \text{m}^{-3}$.

A RH profile generated by the sampling procedure, for a case with the stochastic inputs sampled to be $T = 300\text{K}$, $RH_{out} = 0.62$ and $L = 0.0133L_x$ is shown in figure 9.2. As expected, the RH is highest just above the water surface and lowest at the opening.

Histograms of the sampled values of T , RH_{out} and L for the simulation with $RH_f = 0.9$ show sufficiently good agreement with the associated probability density functions (PDF). The histograms can be found in paper D. In other words, the sampling procedure has generated enough data for the histograms to recover the associated PDFs.

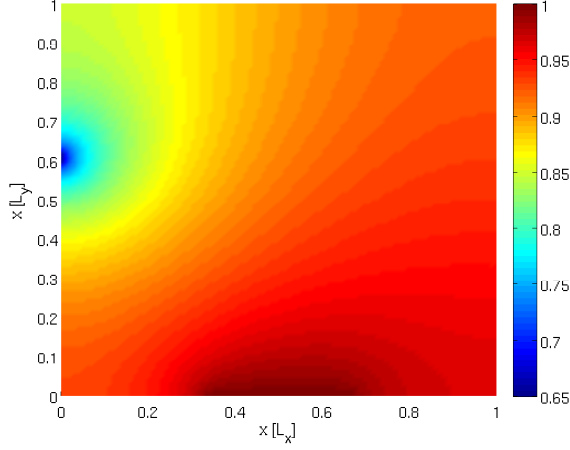


Fig. 9.2: Simulated RH profile in the enclosure with $T = 300K$, $RH_{out} = 0.62$ and $L = 0.0133L_x$. Color bar on the right shows RH.

The probability of failure is modeled with a convergence match of 10^{-5} . The P_f s for three different failing criteria RH_f are given in table 9.2. The table shows how the choice of the failing criterion directly affects P_f . It is seen how by increasing RH_f from 0.90 to 0.95 the P_f significantly decreases, as expected.

Table 9.2: Simulated failure probabilities.

Failing criterion	P_f
$RH_f=0.90$	1.000
$RH_f=0.95$	0.320
$RH_f=0.98$	0.044

Thus, the above mentioned approach shows how the earlier developed SRT-based model can be utilized for humidity-related reliability assessment when combined with a Monte Carlo setup. The method can be extended to take convection into account and can be applied to more complex geometries of enclosures as well as various locations of the circuit board inside it. The most critical point for practical use of the method is to define failing criterion for particular type of PCB. This can be done only through experimental tests.

10. Conclusions

The main motivation for the current research project was to address humidity-related reliability issues which are relevant for packaging of power electronics. In order to achieve this goal models and simulation approaches predicting local humidity and temperature distributions as well as time-evolutions are developed. The approaches are verified either through experiments or by comparison with other well-proved models. The main obtained results can be separated into three large blocks.

In the first block, the main approach to model moisture movement is based on classical equations of computational fluid dynamics, where the conserving transport equations are solved numerically. The novelty of this work lies in the development of methods allowing to combine liquid water and water vapor in the same simulation domain. It is demonstrated how the release of water vapor from freely exposed water surfaces can be simulated with a new simplified expression based on statical rate theory. The model is experimentally verified using a simple setup. It is noticed that the developed model quantifies contributions of moisture diffusion and convection into the final distribution.

Additionally to the SRT-based theory, it is also investigated how natural convection in an enclosure with electronics can be model with the Boussinesq approximation. The simulation approach was developed to mimic relatively simple geometry of the experimental setup that allowed testing applicability of the method. The moisture released from the setup through an opening due to water evaporation inside the enclosure is modeled and good agreement with experimental measurements is obtained.

In the second block, it is shown how film condensation of water can be modeled with a new free surface lattice Boltzmann approach. Novelty of this methodology is in including the mass transfer at the liquid-vapor interface into the free surface lattice Boltzmann framework, which allows to elaborate the evaporation-condensation issues. The extended free surface method is verified by means of another well-proved classical analytic model. Moreover, the developed approach shows excellent agreement with empirical models at flow regimes where the classical analytical model do not apply. Finally, an

entropic realization of the free surface lattice Boltzmann framework is conducted to enhance the numerical stability without grid refinements. This allows film condensation modeling for a wide range of materials.

Finally, as the last block, a reliability assessment method which can be used for power electronics with humidity as the stressing factor is developed. The assessment is strictly based on modeling utilizing physics background, i.e. earlier developed approaches for prediction of humidity distribution using fluid and gas dynamics. To our best knowledge, such approach was never applied to evaluate reliability of electronics in relation to environmental factors. The reliability model itself is based on a Monte Carlo sampling approach from which the probability of failure can be found using known failure criteria.

Thus, the main achieved results demonstrate how to physically model temperature and humidity distributions involving such natural phenomena as diffusion, convection, evaporation and condensation. These models can serve as basis for the development of more practically-oriented tools to improve the design for the packaging of electronics towards higher reliability.

I. Appendix

This appendix serves as support for the theoretical considerations. The material, presented here, is self-contained.

I.1 Clausius–Clapeyron relation

To introduced the saturated vapor pressure the Clausius–Clapeyron relation will be derived. Throughout section I.1 reference [99] is used.

I.1.1 Origin of water vapor

At an exposed water surface water molecules will escape the water surface into the surrounding gas. This can happen for two reasons. Either a gas molecule hits the surface and knocks a molecule off the surface or a water molecule inside the liquid moves with a direction and sufficient energy to break through the surface. If this evaporation process is taking place in a closed chamber some of the earlier escaped water molecules will eventually return to the water, where they either will be reflected by the surface or absorbed. As time passes the system will establish an equilibrium, when the number of water molecules absorbed by the surface is equal to the number of molecules leaving the water surface.

Water molecules in a gaseous phase are well described by the ideal gas law, which is given by

$$p = \frac{nRT}{V}, \quad (\text{I.1})$$

where p is pressure, n is the amount of moles, R is the gas constant, T is the temperature and V is volume. The amount of water molecules in the gas is, thus, determined by a vapor pressure p_v . Likewise, the amount of water molecules in the gas phase, when the liquid is in equilibrium with its vapor, is described by a saturated vapor pressure p_{sat} . The saturated vapor pressure of a given substance will increase with temperature because a given

molecule will be more likely to escape the water surface. This dependency will be discussed in the section below.

I.1.2 Phase transition and stability

Consider a closed chamber of constant volume containing a liquid. It turns out that in order to describe this phase stability, the simplest approach is to consider the derivative of the pressure with respect to temperature of the phase boundaries instead of the actual phase boundary location in a p-T diagram. A system in equilibrium is characterized by a uniformly distributed chemical potential μ . Now, consider a process taking place at the phase boundary where the temperature and pressure is increased by infinitesimally small amounts in such a way that the system remains in equilibrium. Since the chemical potential, in such a process, at a given starting point on the phase boundary (a) is equal to a given finishing point (b), the change in the chemical potentials of the two phases are equal. Thus, $d\mu_l = d\mu_g$. The process is sketched in figure I.1.

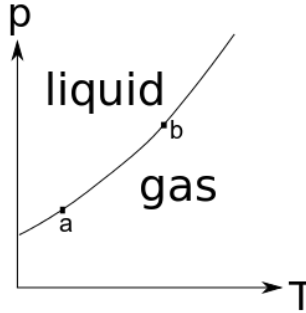


Fig. I.1: Gas-liquid boundary in a p-T diagram.

It can be shown that $d\mu = -S_m dT + V_m dp$, where S_m and V_m are the molar entropy and volume, respectively¹. Equating the chemical potentials gives rise to

$$\begin{aligned}
 V_{l,m} dp_{sat} - S_{l,m} dT &= V_{g,m} dp_{sat} - S_{g,m} dT \\
 \Downarrow \\
 \frac{dp_{sat}}{dT} &= \frac{S_{l,m} - S_{g,m}}{V_{l,m} - V_{g,m}} = \frac{\Delta_{tr} S}{\Delta_{tr} V},
 \end{aligned} \tag{I.2}$$

where the notation Δ_{trs} denotes the change in the quantity due to the phase transition. Equation (I.2) is known as the Claperyon relation and applies to any phase equilibrium of a pure substance.

¹The change in entropy is $ds = \frac{dq}{T}$, where q is the heat energy.

I.1. Clausius–Clapeyron relation

The entropy of evaporation for a given temperature T is $\Delta_{vap}H/T$, where $\Delta_{vap}H$ is the enthalpy of evaporation. The molar volume of a gas is much greater than that of a liquid which gives rise to $\Delta_{tr}V = V_m(g) - V_m(l) \approx V_m(g)$. Combining this with equation (I.1) leads to

$$\begin{aligned} \frac{dp_{sat}}{dT} &= \frac{\Delta_{vap}H}{T \frac{RT}{p}} \\ \Downarrow & \quad \frac{dx}{x} = d \ln x \\ \frac{d \ln p_{sat}}{dT} &= \frac{\Delta_{vap}H}{RT^2}, \end{aligned} \quad (I.3)$$

which is referred to as the Clausius-Clapeyron relation. If the considered temperature range is relatively small, it can be assumed that the enthalpy of evaporation can be treated as independent of temperature. Separating the variables in the Clausius-Clapeyron relation enables

$$\begin{aligned} \int_{\ln p_{sat}^*}^{\ln p_{sat}} d \ln p_{sat} &= \frac{\Delta_{vap}H}{R} \int_{T^*}^T \frac{dT}{T^2} = \frac{\Delta_{vap}H}{R} \left(\frac{1}{T} - \frac{1}{T^*} \right) \\ \Downarrow & \\ p_{sat} &= p_{sat}^* e^{\chi}, \quad \chi = \frac{\Delta_{vap}H}{R} \left(\frac{1}{T^*} - \frac{1}{T} \right). \end{aligned} \quad (I.4)$$

p_{sat}^* is the saturated vapor pressure at a temperature T^* and likewise for p and T . p_{sat}^* and T^* can be thought of as a measurable reference point that describes the order of magnitude in which equation (I.4) holds. The saturated vapor pressure above water at room temperature is [87]

$$p_{sat} = 2.53 \cdot 10^{11} e^{\frac{2.501 \cdot 10^6}{T} / 461.5} \text{Pa}, \quad (I.5)$$

with T in Kelvin. It can be noted, that equation (I.4) only holds for temperatures below the critical temperature T_c , because above this temperature this phase boundary does not exist.

I.2 Nusselt film condensation

Since, the developed free surface entropic lattice Boltzmann model is compared to Nusselt's film condensation model, his model will now be reviewed. Condensation of a pure vapor on a vertical solid surface is a complicated heat transfer process because it involves two fluid phases: the vapor and the condensate. The vapor over the condensate will move towards the condensing surface due to a small pressure gradient near the liquid surface generated by the surface tension. Vapor molecules may strike the liquid surface either to be reflected or penetrate the surface and give up their latent heat of condensation. Whilst the heat migrates through the condensate to the cooling wall the condensate is drawn down by the gravity. [17]

Condensation may occur in two different ways. If the liquid wets the surface, the condensate will form a continuous film, but if the condensate does not wet the surface, the condensate will form droplets. The former is known as 'film condensation' and the latter is referred to as 'dropwise condensation'. Besides the physical condensate formation, the heat transfer of these condensation types is also different. Dropwise condensation yields significantly higher heat transfer rates because of the smaller amount of condensate to resist the heat transfer. However, it is more difficult to maintain which is why most condenser designs are based on film condensation. The film condensation process is illustrated in figure I.2. [17]

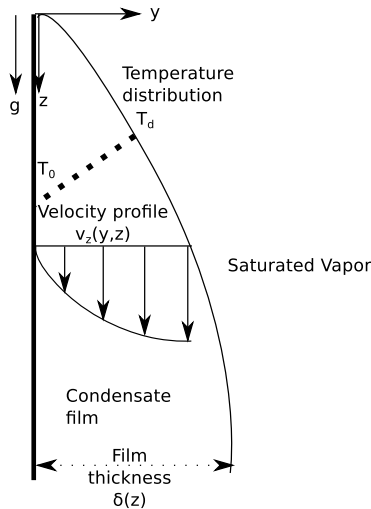


Fig. I.2: Film condensation on a vertical surface.

Nusselt (1916) presented a condensation model by considering laminar condensation on an isothermal, vertical flat surface with the following assump-

I.2. Nusselt film condensation

tions for the system [100]:

- Laminar, steady flow.
- Constant wall temperature.
- Pure, still, saturated vapor.
- Zero shear stress at the film surface.
- Constant fluid properties.
- Liquid inertia can be neglected.
- Linear temperature distribution across the condensate.

For this analysis it is desired to know the local heat transfer coefficient, average heat transfer coefficient and condensing mass flow as a function of the film length.

The Navier-Stokes (momentum conservation equation) in the z -direction for the liquid is given as

$$\underbrace{u \frac{\partial u}{\partial z}}_{=0} + \underbrace{v \frac{\partial u}{\partial y}}_{=0} = \frac{1}{\rho_l} \left(-\frac{dp}{dz} + \mu_l \frac{\partial^2 u}{\partial y^2} + \rho_l g \right) = 0, \quad (\text{I.6})$$

where u and v is the velocity component along the z - and y -axis, respectively, ρ_l is the liquid density, p is pressure, μ_l is the dynamic viscosity and g is the acceleration due to gravity. The first term on the left-hand-side of equation (I.6) is zero because the flow obeys the continuity equation and the second term is zero since there is not a flow in the y -direction. Since the vapor is stagnant the following applies:

$$0 = -\frac{dp}{dz} + \rho_g g \quad (\text{I.7})$$

with ρ_g to be the density of the vapor. Combining equation (I.6) with (I.7) gives rise to

$$\frac{\partial^2 u}{\partial y^2} = -\frac{(\rho_l - \rho_g)g}{\mu_l}. \quad (\text{I.8})$$

This differential equation can be solved by simple integration

$$\begin{aligned} \frac{\partial u}{\partial y} &= -\frac{(\rho_l - \rho_g)g}{\mu_l} y + c_1 \\ \Downarrow \\ u(y) &= -\frac{(\rho_l - \rho_g)g}{\mu_l} \frac{y^2}{2} + c_1 y + c_2. \end{aligned} \quad (\text{I.9})$$

with c_1 and c_2 to be integration constants found from the boundary conditions. Since $u = 0$ at $y = 0$ and $\frac{\partial u}{\partial y} = 0$ at $y = \delta$, where δ is the film thickness, one can show that

$$u(y) = \frac{(\rho_l - \rho_g)g}{\mu_l} \left[y\delta - \frac{y^2}{2} \right]. \quad (\text{I.10})$$

Hence, the condensing mass flow rate (in units of depth B) will be

$$\dot{m} = \rho_l \int_0^\delta u(y) dy = \rho_l \frac{(\rho_l - \rho_g)g}{3\mu_l} \delta^3, \quad d\dot{m} = \rho_l \frac{(\rho_l - \rho_g)g}{2\mu_l} \delta^2 d\delta. \quad (\text{I.11})$$

Now, consider a slice on the film condensate, illustrated in figure I.3.

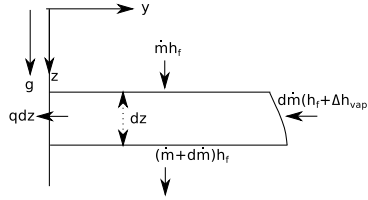


Fig. I.3: Energy flow terms for a slice of the condensate film.

The energy balance, while neglecting sub-cooling, requires that

$$\begin{aligned} (\text{Rate at which enthalpy leaves slice}) &= (\text{Rate at which enthalpy enters slice}) \\ &= \text{Rate of heat transfer to slice} \\ &\Downarrow \\ (\dot{m} + d\dot{m}) h_f - \dot{m} h_f - d\dot{m} (h_f + \Delta h_{vap}) &= -k_l \left. \frac{\partial T}{\partial y} \right|_{y=0} dz \\ &\Downarrow \\ -d\dot{m} \Delta h_{vap} &= -k_l \frac{T_d - T_0}{\delta} dz, \end{aligned} \quad (\text{I.12})$$

where Δh_{vap} is the latent heat of condensation, h_f is the enthalpy per mass and k_l is the thermal conductivity for the liquid. Using equation (I.11) it is possible to rewrite the above equation to

$$\begin{aligned} \delta^3 d\delta &= k_l \mu_l \frac{T_d - T_0}{\Delta h_{vap} \rho_l (\rho_l - \rho_g) g} dz \\ &\Downarrow \\ \frac{\delta^4}{4} &= k_l \mu_l \frac{T_d - T_0}{\Delta h_{vap} \rho_l (\rho_l - \rho_g) g} z + c_1 \end{aligned} \quad (\text{I.13})$$

where the integration constant $c_1 = 0$ since $\delta = 0$, at $z = 0$. Hence, the film thickness is given as

$$\delta = \left[\frac{4k_l \mu_l (T_d - T_0) z}{\Delta h_{vap} \rho_l (\rho_l - \rho_g) g} \right]^{1/4}. \quad (\text{I.14})$$

I.2. Nusselt film condensation

It is now possible to obtain the local heat transfer coefficient h as it is defined as

$$h = \frac{\text{Heat flux at the wall}}{T_d - T_0} = \frac{k \frac{T_d - T_0}{\delta}}{T_d - T_0} = \frac{k}{\delta} = \left[\frac{k_l^3 \Delta h_{vap} \rho_l (\rho_l - \rho_g) g}{4 \mu_l (T_d - T_0) z} \right]^{1/4}. \quad (\text{I.15})$$

Thus, the average heat transfer coefficient is

$$\bar{h} = \frac{1}{L} \int_0^L \left[\frac{k_l^3 \Delta h_{vap} \rho_l (\rho_l - \rho_g) g}{4 \mu_l (T_d - T_0) z} \right]^{1/4} dz = \underbrace{\frac{4}{3} \frac{1}{4^{1/4}}}_{\approx 0.943} \left[\frac{k_l^3 \Delta h_{vap} \rho_l (\rho_l - \rho_g) g}{\mu_l (T_d - T_0) L} \right]^{1/4}. \quad (\text{I.16})$$

Notice, that $\bar{h}(z = L) = \frac{4}{3} h(z = L)$. From the above analysis two important questions can be answered: [100]

1. Average heat flux for a plate of length $L = \bar{h}(T_d - T_0) \left[\frac{\text{W}}{\text{m}^2} \right]$.
2. Average condensation flux for a plate of length $L = \frac{\bar{h}(T_d - T_0)}{\Delta h_{vap}} \left[\frac{\text{kg}}{\text{m}^2 \text{s}} \right]$.

Since the above analysis utilizes a laminar film without any waves or ripples the formula is only valid for film Reynolds numbers $Re_L \leq 33$, where

$$Re_L = \frac{4 \dot{m}(z = L)}{\mu_l}. \quad (\text{I.17})$$

These interfacial waves will cause mixing which will enhance the heat transfer significantly. However, a number of empirical formulas have been suggested. [100]

References

References

- [1] Mauro Ciappa. Selected failure mechanisms of modern power modules. *Microelectronics Reliability*, 42(4–5):653 – 667, 2002.
- [2] W. Kanert. Active cycling reliability of power devices: Expectations and limitations. *Microelectronics Reliability*, 52(9–10):2336 – 2341, 2012.
- [3] J.M. Guerrero, F. Blaabjerg, T. Zhelev, K. Hemmes, E. Monmasson, S. Jemei, M.P. Comech, R. Granadino, and J.I. Frau. Distributed generation: Toward a new energy paradigm. *IEEE Industrial Electronics Magazine*, 4(1):52 – 64, March 2010.
- [4] R.O. Nielsen, J. Due, and S. Munk-Nielsen. Innovative measuring system for wear-out indication of high power igbt modules. In *Energy Conversion Congress and Exposition (ECCE): Proceedings, Sept. 17-22, 2011, Phoenix, AZ, USA*, pages 1785–1790. IEEE, 2011.
- [5] Hua Lu, Chris Bailey, and Chunyan Yin. Design for reliability of power electronics modules. *Microelectronics Reliability*, 49(9–11):1250 – 1255, 2009.
- [6] A. Birolini. *Reliability Engineering: Theory and Practice*. Springer, 2010.
- [7] Matthias Ralf Werner and Wolfgang R Fahrner. Review on materials, microsensors, systems and devices for high-temperature and harsh-environment applications. *IEEE Transactions on Industrial Electronics*, 48(2):249–257, 2001.
- [8] Rajan Ambat. Climatic reliability of electronic devices and components. *SMT Magazine*, (April):12–28, 2014.
- [9] Vadimas Verdingovas, Morten Stendahl Jellesen, and Rajan Ambat. Solder flux residues and humidity-related failures in electronics: Relative

- effects of weak organic acids used in no-clean flux systems. *Journal of Electronic Materials*, 44(4):1116–1127, 2015.
- [10] J.W. McPherson. *Reliability Physics and Engineering: Time-To-Failure Modeling*. Springer, 2013.
 - [11] S. Chapman and T.G. Cowling. *The Mathematical Theory of Non-uniform Gases: An Account of the Kinetic Theory of Viscosity, Thermal Conduction and Diffusion in Gases*. Cambridge University Press, 1970.
 - [12] G.M. Kremer. *An Introduction to the Boltzmann Equation and Transport Processes in Gases*. Interaction of Mechanics and Mathematics. Springer, 2010.
 - [13] Alexander Gorban and Ilya Karlin. Hilbert’s 6th problem: Exact and approximate hydrodynamic manifolds for kinetic equations. *Bulletin of the American Mathematical Society*, 51(2):187–246, 2014.
 - [14] H.K. Versteeg and W. Malalasekera. *An Introduction to Computational Fluid Dynamics: The Finite Volume Method*. Pearson Education Limited, 2007.
 - [15] F. A. Schwertz and Jeanne E. Brow. Diffusivity of water vapor in some common gases. *The Journal of Chemical Physics*, 19(5):640–646, 1951.
 - [16] R. Cunningham. *Diffusion in Gases and Porous Media*. Springer, 1980.
 - [17] R.B. Bird, W.E. Stewart, and E.N. Lightfoot. *Transport Phenomena*. Wiley, 2007.
 - [18] J. Crank. *The Mathematics of Diffusion*. Clarendon Press, 1979.
 - [19] T.L. Hudson and O. Aharonson. *Growth, Diffusion, and Loss of Subsurface Ice on Mars: Experiments and Models*. PhD thesis. California Institute of Technology, 2008.
 - [20] R.W. Schrage. *A Theoretical Study of Interphase Mass Transfer*. University Microfilms, 1986.
 - [21] C. Shen. *Rarefied Gas Dynamics: Fundamentals, Simulations and Micro Flows*. Heat and Mass Transfer. Springer, 2005.
 - [22] G. Fang and C. A. Ward. Temperature measured close to the interface of an evaporating liquid. *Phys. Rev. E*, 59:417–428, Jan 1999.
 - [23] G. Fang and C. A. Ward. Examination of the statistical rate theory expression for liquid evaporation rates. *Phys. Rev. E*, 59:441–453, Jan 1999.

References

- [24] C. A. Ward and D. Stanga. Interfacial conditions during evaporation or condensation of water. *Phys. Rev. E*, 64:051509, Oct 2001.
- [25] C. A. Ward and G. Fang. Expression for predicting liquid evaporation flux: Statistical rate theory approach. *Phys. Rev. E*, 59:429–440, Jan 1999.
- [26] Kausik S. Das, Brendan D. MacDonald, and C. A. Ward. Stability of evaporating water when heated through the vapor and the liquid phases. *Phys. Rev. E*, 81:036318, Mar 2010.
- [27] H. Hertz. Ueber die verdunstung der flüssigkeiten, insbesondere des quecksilbers, im luftleeren raume. *Annalen der Physik*, 253(10):177–193, 1882.
- [28] Martin Knudsen. Die maximale verdampfungsgeschwindigkeit des quecksilbers. *Annalen der Physik*, 352(13):697–708, 1915.
- [29] Maurice Bond and Henning Struchtrup. Mean evaporation and condensation coefficients based on energy dependent condensation probability. *Phys. Rev. E*, 70:061605, Dec 2004.
- [30] Jonathan Barrett and Charles Clement. Kinetic evaporation and condensation rates and their coefficients. *Journal of Colloid and Interface Science*, 150(2):352 – 364, 1992.
- [31] R. Marek and J. Straub. Analysis of the evaporation coefficient and the condensation coefficient of water. *International Journal of Heat and Mass Transfer*, 44(1):39 – 53, 2001.
- [32] I.W. Eames, N.J. Marr, and H. Sabir. The evaporation coefficient of water: a review. *International Journal of Heat and Mass Transfer*, 40(12):2963 – 2973, 1997.
- [33] R.Ya. Kucherov and L.E. Rikenglaz. The problem of measuring the condensation coefficient. *Doklady Akademii Nauk SSSR (Phys. Chem. Section)*, 133:735–737, 1960.
- [34] D.A. Labuntsov and A.P. Kryukov. Analysis of intensive evaporation and condensation. *International Journal of Heat and Mass Transfer*, 22(7):989 – 1002, 1979.
- [35] Amal Lotfi, Jadran Vrabec, and Johann Fischer. Evaporation from a free liquid surface. *International Journal of Heat and Mass Transfer*, 73(0):303 – 317, 2014.
- [36] Bruce C Garrett, Gregory K Schenter, and Akihiro Morita. Molecular simulations of the transport of molecules across the liquid/vapor interface of water. *Chemical reviews*, 106(4):1355–1374, 2006.

- [37] Tatsuya Ishiyama, Shigeo Fujikawa, Thomas Kurz, and Werner Lauterborn. Nonequilibrium kinetic boundary condition at the vapor-liquid interface of argon. *Phys. Rev. E*, 88:042406, 2013.
- [38] Tatsuya Ishiyama, Takeru Yano, and Shigeo Fujikawa. Kinetic boundary condition at a vapor-liquid interface. *Phys. Rev. Lett.*, 95:084504, 2005.
- [39] Takaharu Tsuruta, Hiroyuki Tanaka, and Takashi Masuoka. Condensation/evaporation coefficient and velocity distributions at liquid-vapor interface. *International Journal of Heat and Mass Transfer*, 42(22):4107 – 4116, 1999.
- [40] D Bedeaux. Nonequilibrium thermodynamics and statistical physics of surfaces. *Adv. Chem. Phys.*, 64(47):C109, 1986.
- [41] G. Lebon and D. Jou. *Understanding Non-equilibrium Thermodynamics: Foundations, Applications, Frontiers*. Springer, 2008.
- [42] S. Kjelstrup and D. Bedeaux. *Non-equilibrium Thermodynamics of Heterogeneous Systems*. World Scientific, 2008.
- [43] Lars Onsager. Reciprocal relations in irreversible processes. i. *Phys. Rev.*, 37:405–426, Feb 1931.
- [44] D. Bedeaux, L.J.F. Hermans, and T. Yttrhus. Slow evaporation and condensation. *Physica A: Statistical Mechanics and its Applications*, 169(2):263 – 280, 1990.
- [45] D. Bedeaux and S. Kjelstrup. Transfer coefficients for evaporation. *Physica A: Statistical Mechanics and its Applications*, 270(3–4):413 – 426, 1999.
- [46] J. Xu, S. Kjelstrup, D. Bedeaux, A. Røsjorde, and L. Rekvig. Verification of onsager’s reciprocal relations for evaporation and condensation using non-equilibrium molecular dynamics. *Journal of Colloid and Interface Science*, 299(1):452 – 463, 2006.
- [47] Atam Kapoor and Janet AW Elliott. Nonideal statistical rate theory formulation to predict evaporation rates from equations of state. *The Journal of Physical Chemistry B*, 112(47):15005–15013, 2008.
- [48] H.B. Callen. *Thermodynamics and an Introduction to Thermostatistics*. Wiley, 1985.
- [49] F.W. Sears and G.L. Salinger. *Thermodynamics, Kinetic Theory, and Statistical Thermodynamics*. Addison-Wesley Publishing Company, 1975.
- [50] T.L. Hill. *An Introduction to Statistical Thermodynamics*. Dover Publications, 1960.

References

- [51] Cyrus K Aidun and Jonathan R Clausen. Lattice-boltzmann method for complex flows. *Annual review of fluid mechanics*, 42:439–472, 2010.
- [52] Sauro Succi. Lattice boltzmann 2038. *EPL (Europhysics Letters)*, 109(5):50001–50007, 2015.
- [53] S. Succi. *The Lattice Boltzmann Equation: For Fluid Dynamics and Beyond*. Clarendon Press, 2001.
- [54] Succi, S. Lattice boltzmann across scales: from turbulence to dna translocation. *Eur. Phys. J. B*, 64(3), 2008.
- [55] U. Frisch, B. Hasslacher, and Y. Pomeau. Lattice-gas automata for the navier-stokes equation. *Phys. Rev. Lett.*, 56:1505–1508, Apr 1986.
- [56] Xiaoyi He, Xiaowen Shan, and Gary D. Doolen. Discrete boltzmann equation model for nonideal gases. *Phys. Rev. E*, 57, Jan 1998.
- [57] Xiaoyi He, Shiyi Chen, and Gary D. Doolen. A novel thermal model for the lattice boltzmann method in incompressible limit. *Journal of Computational Physics*, 146(1):282 – 300, 1998.
- [58] FJ Higuera and J Jimenez. Boltzmann approach to lattice gas simulations. *EPL (Europhysics Letters)*, 9(7):663, 1989.
- [59] Chen Peng. *The Lattice Boltzmann method for fluid dynamics: Theory and applications*. M. Math, Department of Mathematics, Ecole Polytechnique Federale de Lausanne, 2011.
- [60] A.A. Mohamad. *Lattice Boltzmann Method: Fundamentals and Engineering Applications with Computer Codes*. Springer, 2011.
- [61] M.C. Sukop and D.T. Thorne. *Lattice Boltzmann Modeling: An Introduction for Geoscientists and Engineers*. Springer, 2007.
- [62] Gerhard Wellein, Thomas Zeiser, Georg Hager, and Stefan Donath. On the single processor performance of simple lattice boltzmann kernels. *Computers & Fluids*, 35(8):910–919, 2006.
- [63] IV Karlin, A Ferrante, and HC Öttinger. Perfect entropy functions of the lattice boltzmann method. *EPL (Europhysics Letters)*, 47(2):182, 1999.
- [64] Shyam S. Chikatamarla and Iliya V. Karlin. Entropy and galilean invariance of lattice boltzmann theories. *Phys. Rev. Lett.*, 97:190601, Nov 2006.
- [65] S Ansumali, IV Karlin, and HC Öttinger. Minimal entropic kinetic models for hydrodynamics. *EPL (Europhysics Letters)*, 63(6):798, 2003.

- [66] Santosh Ansumali and Iliya V. Karlin. Stabilization of the lattice boltzmann method by the H theorem: A numerical test. *Phys. Rev. E*, 62:7999–8003, Dec 2000.
- [67] S. S. Chikatamarla, S. Ansumali, and I. V. Karlin. Entropic lattice boltzmann models for hydrodynamics in three dimensions. *Phys. Rev. Lett.*, 97:010201, Jul 2006.
- [68] Shiyi Chen and Gary D Doolen. Lattice boltzmann method for fluid flows. *Annual review of fluid mechanics*, 30(1):329–364, 1998.
- [69] Qisu Zou and Xiaoyi He. On pressure and velocity boundary conditions for the lattice Boltzmann BGK model. *Phys. Fluids*, 9:1591–1598, 1997.
- [70] Jonas Latt, Bastien Chopard, Orestis Malaspinas, Michel Deville, and Andreas Michler. Straight velocity boundaries in the lattice boltzmann method. *Phys. Rev. E*, 77:056703, May 2008.
- [71] I. V. Karlin, D. Sichau, and S. S. Chikatamarla. Consistent two-population lattice boltzmann model for thermal flows. *Phys. Rev. E*, 88:063310, Dec 2013.
- [72] S.S. Chikatamarla and I.V. Karlin. Entropic lattice boltzmann method for turbulent flow simulations: Boundary conditions. *Physica A: Statistical Mechanics and its Applications*, 392(9):1925 – 1930, 2013.
- [73] Zhaoli Guo, Chuguang Zheng, and Baochang Shi. An extrapolation method for boundary conditions in lattice Boltzmann method. *Phys. Fluids*, 14:2007–2010, 2002.
- [74] B. Dorschner, S.S. Chikatamarla, F. Bösch, and I.V. Karlin. Grad’s approximation for moving and stationary walls in entropic lattice boltzmann simulations. *Journal of Computational Physics*, 295(0):340 – 354, 2015.
- [75] SS Chikatamarla, SKIV Ansumali, and IV Karlin. Grad’s approximation for missing data in lattice boltzmann simulations. *EPL (Europhysics Letters)*, 74(2):215, 2006.
- [76] R Robert Nourgaliev, Truc-Nam Dinh, TG Theofanous, and D Joseph. The lattice boltzmann equation method: theoretical interpretation, numerics and implications. *International Journal of Multiphase Flow*, 29(1):117–169, 2003.
- [77] Xiaowen Shan and Hudong Chen. Lattice boltzmann model for simulating flows with multiple phases and components. *Phys. Rev. E*, 47:1815–1819, Mar 1993.

References

- [78] Xiaowen Shan and Hudong Chen. Simulation of nonideal gases and liquid-gas phase transitions by the lattice boltzmann equation. *Phys. Rev. E*, 49:2941–2948, Apr 1994.
- [79] Nils Thürey, C Körner, and U Rüde. Interactive free surface fluids with the lattice boltzmann method. *Technical Report 05-4. University of Erlangen-Nuremberg, Germany*, 2005.
- [80] U Rüde and N Thürey. Free surface lattice-boltzmann fluid simulations with and without level sets. In *Vision, Modeling, and Visualization 2004: Proceedings, Nov. 16-18, 2004, Stanford, USA*, page 199. IOS Press, 2004.
- [81] A. Mazloomi M, S. S. Chikatamarla, and I. V. Karlin. Entropic lattice boltzmann method for multiphase flows. *Phys. Rev. Lett.*, 114:174502, May 2015.
- [82] AL Kupershtokh. New method of incorporating a body force term into the lattice boltzmann equation. In *5th International EHD Workshop: Proceedings, Aug. 30-31, 2004, Poitiers, France*, pages 241 – 246, 2004.
- [83] Peng Yuan and Laura Schaefer. Equations of state in a lattice boltzmann model. *Physics of Fluids (1994-present)*, 18(4):042101, 2006.
- [84] Li Chen, Qinjun Kang, Yutong Mu, Ya-Ling He, and Wen-Quan Tao. A critical review of the pseudopotential multiphase lattice boltzmann model: Methods and applications. *International Journal of Heat and Mass Transfer*, 76(0):210 – 236, 2014.
- [85] Simon Bogner, Regina Ammer, and Ulrich Rüde. Boundary conditions for free interfaces with the lattice boltzmann method. *Journal of Computational Physics*, 297:1 – 12, 2015.
- [86] S.K. Choi, R. Grandhi, and R.A. Canfield. *Reliability-based Structural Design*. Springer, 2006.
- [87] Mark G Lawrence. The relationship between relative humidity and the dewpoint temperature in moist air: A simple conversion and applications. *Bulletin of the American Meteorological Society*, 86(2):225–233, 2005.
- [88] Vadimas Verdingovas, Morten Stendahl Jellesen, and Rajan Ambat. Solder flux residues and humidity-related failures in electronics: Relative effects of weak organic acids used in no-clean flux systems. *Journal of Electronic Materials*, 44(4):1116–1127, 2015.
- [89] COMSOL Multiphysics: Version 4.3b. *User’s guide*. Comsol, 2013.
- [90] H. Bruus. *Theoretical Microfluidics*. Oxford Master Series in Physics. OUP Oxford, 2008.

- [91] TR Marrero and Edward Allen Mason. Gaseous diffusion coefficients. *Journal of Physical and Chemical Reference Data*, 1(1):3–118, 1972.
- [92] Jiehei Zhang, Ajaykumar Gupta, and John Baker. Effect of relative humidity on the prediction of natural convection heat transfer coefficients. *Heat transfer engineering*, 28(4):335–342, 2007.
- [93] Xiuliang Liu and Ping Cheng. Lattice boltzmann simulation of steady laminar film condensation on a vertical hydrophilic subcooled flat plate. *International Journal of Heat and Mass Transfer*, 62:507–514, 2013.
- [94] Xiaoyi He, Shiyi Chen, and Gary D Doolen. A novel thermal model for the lattice boltzmann method in incompressible limit. *Journal of Computational Physics*, 146(1):282–300, 1998.
- [95] Wilhelm Nusselt. Die oberflächenkondensation des wasserdampfes the surface condensation of water. *Zetschr. Ver. Deutch. Ing.*, 60:541–546, 1916.
- [96] V Ya Shkadov. Wave flow regimes of a thin layer of viscous fluid subject to gravity. *Fluid Dynamics*, 2(1):29–34, 1967.
- [97] SS Kutateladze. Semi-empirical theory of film condensation of pure vapours. *International Journal of Heat and Mass Transfer*, 25(5):653–660, 1982.
- [98] SL Chen, FM Gerner, and CL Tien. General film condensation correlations. *Experimental Heat Transfer An International Journal*, 1(2):93–107, 1987.
- [99] P. Atkins and J. de Paula. *Physical Chemistry*. W. H. Freeman, 2006.
- [100] S.M. Ghiaasiaan. *Two-Phase Flow, Boiling, and Condensation: In Conventional and Miniature Systems*. Cambridge University Press, 2007.

Acknowledgments

There are several people whom I will like to thank. During this project there have been regular meetings with people from the companies associated with the Center of Reliable Power Electronics (CORPE), a humidity focus group. In particular I will thank Lars Rimestad, Thorkild Kvistgaard, John Jacobsen and Jens Peter Krog from Grundfos and Kirsten Stentoft-Hansen, Knud Bakbo Kruse, Dietmar Weiss, Peter de Place Rikken and Jørn Landkildehus from Danfoss. I am grateful for all the fruitful discussions with the member of this group and the initial help for starting up the project. I will also like to thank the company Grundfos for providing the experimental setup, called AquaRIUM, and the all help regarding the equipment for the experiments.

I will like to thank all my colleagues at the Department of Physics and Nanotechnology. Especially, I am grateful for help from my colleagues also associated with the CORPE project. I will, thus, thank Kjeld Pedersen for the help starting the project, Kristian Bonderup Pedersen and Dennis Achton Nielsen for fruitful discussions and Peter Kjær Kristensen for help and guidance with any experiment issues.

I will like to express deep gratitude to Prof. Ilya Karlin and his group at ETH for the hospitably and guidance during my research stay in Zürich. It was a very rewarding stay and it was all because of you guys. Also, I am grateful for the lattice Boltzmann lecture material and the possibility of using it to prepare the thesis.

I would also like to thank my supervisor Vladimir Popok for help and guidance in the field of research which was new for both of us. Last, but not least, I would like to thank my wife Ditte for her ever lasting support.

Finally, without financial support this project would never come to be. I, therefore, gratefully acknowledge the support from the CORPE funded the Innovation Foundation Denmark. I will also thank the Augustinus foundation, Oticon Foundation and the support from "Christian og Otilia Brorsons Rejselegat" in relation to my exchange stay in Switzerland.

Publications

Paper A

Humidity distribution affected by freely exposed
water surfaces: Simulations and experimental
verification

Morten A. Hygum, Vladimir N. Popok

The paper has been published in the
Physical Review E Vol. 90, 013023, 2014.

© 2014 APS

The layout has been revised.

Humidity distribution affected by freely exposed water surfaces: Simulations and experimental verification

M. A. Hygum^{*} and V. N. Popok*Department of Physics and Nanotechnology, Aalborg University, Skjernvej 4a, 9220 Aalborg East, Denmark
(Received 27 March 2014; published 28 July 2014)*

Accurate models for the water vapor flux at a water-air interface are required in various scientific, reliability and civil engineering aspects. Here, a study of humidity distribution in a container with air and freely exposed water is presented. A model predicting a spatial distribution and time evolution of relative humidity based on statistical rate theory and computational fluid dynamics is developed. In our approach we use short-term steady-state steps to simulate the slowly evolving evaporation in the system. Experiments demonstrate considerably good agreement with the computer modeling and allow one to distinguish the most important parameters for the model.

DOI: [10.1103/PhysRevE.90.013023](https://doi.org/10.1103/PhysRevE.90.013023)

PACS number(s): 47.10.Fg, 05.70.Fh, 47.11.Fg

I. INTRODUCTION

One of the significant issues addressed by civil and reliability engineering is the problem of climatic simulations which very often includes the aspects of relative humidity (RH) of air affected by the presence of water. In particular, for electronic reliability engineering it is of importance to predict the humidity inside various enclosures. Some electronics operate outdoors and thus experience daily changes of temperature and humidity. It is hardly possible and quite expensive to make the boxes or cabinets completely hermetic. Therefore, changes in temperature and humidity can lead to water condensation and evaporation cycles which are dangerous for the electronics and can cause failures. Hence, the systems of interest here are containers in which a freely exposed water surface will give rise to an increase in the relative humidity of the air. The evaporation of water from the surface is thus not due to a boiling process but a desorption of the water molecules as a result of the interaction with gas molecules.

The adsorption and desorption processes of water molecules at water-air interfaces involve stochastic collisions of molecules in the gas and liquid phases, and therefore correspond to a rather complex problem.

There are three main approaches in order to deal with this problem. One of them is molecular dynamics (MD). An overview of this approach can be seen, e.g., in [1]. Another one, based on kinetic theory, is to solve the Boltzmann transport equation and obtain the velocity distribution function describing the system of interest. See [2,3] for a description of simulations based on kinetic theory. The third way is modeling based on irreversible thermodynamics where the basic principles of energy balance and a positive production of entropy at the interface are in use.

The MD approach attacks the problem at its fundamentals, i.e., molecules of different energies collide with water molecules at the surface. It has been used to investigate the mass fluxes at gas-liquid interfaces (see, e.g., [4] and [5]). It is computationally demanding, and therefore only fits to simulations of systems at the microscopic scale. However, MD simulations have been used to investigate the energy dependence of the condensation and evaporation coefficients [6].

These dependencies have been adapted to develop models for interfaces which are used as boundary conditions for direct simulation Monte Carlo methods [7].

Attempts to address the problem of water-air interfaces based on a macroscopic perspective have also been made. The Navier-Stokes and continuity equations are solved with particular source terms that take the vapor-liquid interfaces into account (see, e.g., [8]).

About two decades ago, Fang, Ward, and Stanga [9–11] showed that an air-water interface at steady-state evaporation and condensation conditions exhibits a relatively large temperature jump, on the order of a few degrees K. This result was in disagreement with the kinetic theory of evaporation and condensation. They developed an expression based on statistical rate theory (SRT) for the mass flux at a gas-liquid interface [10]. This development brought the model in good agreement with the temperature discontinuity and introduced a strong tool for computationally nonheavy simulations. Another advantage of SRT is in the absence of fitting parameters which makes the modeling more reliable.

In this paper a model which is based on the SRT approach suggested in [9–11] is developed. In contrast to the original usage of the expression we apply the model to slowly evolving dynamic systems using a number of sequent steady-state steps. By this approach, we are testing applicability of the model because to our best knowledge SRT expressions have not yet been used in computational fluid dynamics (CFD).

The developed model is utilized to predict the spatial RH distribution at room temperature in a container with liquid water. We verify the model experimentally and show the importance of taking convection processes into account.

II. THEORETICAL BASE FOR MODELING

This section presents some key equations important for understanding the developed model. The transport of water vapor can be modeled as movement of a diluted species in air. This is governed by the continuity equation [12]

$$\frac{\partial c(\vec{r}, t)}{\partial t} + \vec{\nabla} \cdot \vec{J}(\vec{r}, t) = Z(\vec{r}, t), \quad (1)$$

where c is the concentration of water vapor, \vec{r} is the position, and t is the time. \vec{J} is the vapor flux and Z is the source term which represents the water surface. The flux term can be

^{*}mah@nano.aau.dk

divided into diffusive and convective parts [12]:

$$\vec{J}(\vec{r}, t) = -D_c \vec{\nabla} c(\vec{r}, t) + c(\vec{r}, t) \vec{u}(\vec{r}, t), \quad (2)$$

with D_c to be the diffusion coefficient and \vec{u} to be an Eulerian velocity field. Air is modeled as a slightly compressible fluid. The momentum conservation equation is given as

$$\rho \left[\frac{\partial \vec{u}}{\partial t} + (\vec{\nabla} \vec{u}) \cdot \vec{u} \right] = -\vec{\nabla} p + \vec{\nabla} \cdot \tau + \vec{f}, \quad (3)$$

where p is the pressure, ρ is the density, and \vec{f} is the body force due to gravity. It is worth mentioning that in some studies the nonlinear velocity term in Eq. (3) can be neglected, thus simplifying the calculations. However, as can be seen in Sec. III, in our case the flow gives rise to Reynolds numbers $Re \sim 30$. Moreover, we investigate how the flow evolves to the steady state. These conditions do not allow one to disregard this term completely [12]. The viscous stress tensor is

$$\tau = \nu [\vec{\nabla} u + (\vec{\nabla} u)^T] - \frac{2}{3} \nu (\vec{\nabla} \cdot \vec{u}) \mathbf{I} \quad (4)$$

with \mathbf{I} to be the identity matrix and ν to be the dynamic viscosity [12]. The conservation of mass is governed by

$$\frac{\partial \rho}{\partial t} + \vec{\nabla} \cdot (\rho \vec{u}) = 0. \quad (5)$$

The calculation of the source term Z in Eq. (1) is based on the expression provided in [10]. Three central assumptions are made in order to derive the expression. The authors assume that the system of interest is at steady state and that the energy to maintain the temperature in the liquid is provided by the surroundings. It is also assumed that the condensation and evaporation coefficients are equal to unity. The following expression for the magnitude of molecular flux orthogonal to the water surface was developed [10]:

$$J_{\text{SRT}} = K_e \left[\exp\left(\frac{\Delta S}{k_B}\right) - \exp\left(-\frac{\Delta S}{k_B}\right) \right]. \quad (6)$$

The first term is responsible for the evaporation and the second one for the condensation. The interfacial entropy change was shown to be

$$\Delta S = \left(\frac{\mu_l}{T_l} - \frac{\mu_v}{T_v} \right) + h_v \left(\frac{1}{T_v} - \frac{1}{T_l} \right), \quad (7)$$

where μ is the chemical potential, h is the enthalpy per molecule, and T is the temperature; all at the interface. The subscripts “ l ” and “ v ” denote liquid and vapor, respectively. The exchange rate K_e represents the rate at which molecules interact with the surface. It can be obtained by solving the Boltzmann transport equation for a system of a semi-infinite surface at steady state. An elaboration of this theory can be found in [13,14] and the exchange rate is given by

$$K_e = \frac{p_{v,e}}{\sqrt{2\pi m k_B T_l}}, \quad (8)$$

where m is the molecular mass and $p_{v,e}$ is the vapor pressure at equilibrium. This pressure can be rewritten using a particular reference for the chemical potential where it is the same for the molecules in the vapor and liquid phase [10]:

$$\mu_l(T_l, p_{\text{sat}}(T_l)) = \mu_v(T_l, p_{\text{sat}}(T_l)) = \mu(T_l, p_{\text{sat}}(T_l)). \quad (9)$$

In this reference frame and under the assumption that the water is incompressible, the chemical potential can be given as

$$\mu_l(T_l, p_{l,e}) = \mu(T_l, p_{\text{sat}}(T_l)) + V_l(p_{l,e} - p_{\text{sat}}(T_l)), \quad (10)$$

with V_l to be the molar specific volume of the liquid. The chemical potential for the vapor, with the same reference state, is

$$\mu_v(T_v, p_{v,e}) = \mu(T_l, p_{\text{sat}}(T_l)) + RT \ln \frac{p_{v,e}}{p_{\text{sat}}(T_l)}, \quad (11)$$

where the vapor has been assumed to be ideal [10]. At equilibrium, the chemical potential on the left-hand side of Eqs. (10) and (11) are the same, which then gives rise to

$$p_{v,e} = \eta p_{\text{sat}}(T_l), \quad (12)$$

where

$$\eta = e^{(V_l/V_v)[(p_{l,e}/p_{\text{sat}}(T_l))-1]}, \quad (13)$$

with V_v to be the molar specific volume of the vapor. It should be noticed that $V_v \gg V_l$ leading to $\eta \approx 1$ because $p_{l,e} \approx p_{\text{sat}}$. p_l and p_v are connected by the Young-Laplace equation [12]:

$$p_l = p_v + \gamma \left(\frac{1}{r_1} + \frac{1}{r_2} \right), \quad (14)$$

where γ is the surface tension and r_1 and r_2 are the radii of curvature. As shown in [10] the entropy change can be given as

$$\begin{aligned} \Delta S = k_B & \left\{ 4 \left(1 - \frac{T_v}{T_l} \right) + \left(\frac{1}{T_v} - \frac{1}{T_l} \right) \right. \\ & \times \sum_{l=1}^3 \left(\frac{\hbar \omega_l}{2k_B} + \frac{\hbar \omega_l}{k_B e^{\hbar \omega_l / k_B T_v} - k_B} \right) \\ & + \ln \left[\left(\frac{T_v}{T_l} \right)^4 \left(\frac{p_{\text{sat}}(T_l)}{p_v} \right) \right] \\ & \left. + \ln \left[\frac{q_{\text{vib}}(T_v)}{q_{\text{vib}}(T_l)} \right] + \frac{V_l}{k_B T_l} [p_l - p_{\text{sat}}(T_l)] \right\}, \quad (15) \end{aligned}$$

where the vibrational partition function for the ideal polyatomic molecules, which in this case is water, may be expressed as

$$q_{\text{vib}}(T) = \prod_{l=1}^3 \frac{e^{-\hbar \omega_l / 2k_B T}}{1 - e^{-\hbar \omega_l / k_B T}}. \quad (16)$$

The vibrational frequencies of the covalent bonds ω_l of a water molecule are 1590, 3651, and 3756 cm^{-1} [11].

III. SIMULATIONS

The simulations are carried out for the exact same geometry as the experimental setup has. This geometry is shown in Fig. 1 representing a cylinder with a water vessel (also of cylindrical shape) placed inside it. More details on the experimental setup can be found in the next section. To simulate RH inside the setup, the following issues are taken into account. The water surface of interest is relatively flat. Therefore, the curvature radii used in Eq. (14) are assumed to be so large that the pressure difference across the interface can be neglected.

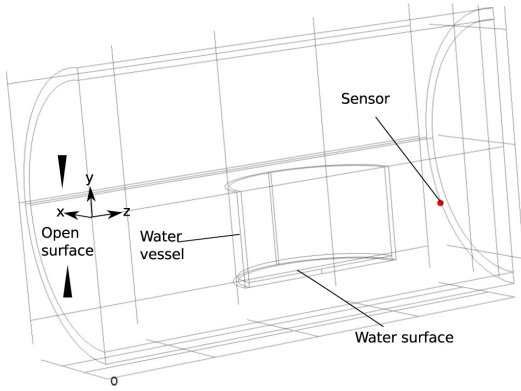


FIG. 1. (Color online) Schematic of the geometric model input.

Furthermore, the water level in the vessel is modeled to be constant due to the low evaporation rate on the time scales typically used in the simulations. This assumption follows from the experimental results described below. The water vapor is regarded as a diluted gas in air. The water surface represents a water vapor source, where a flux perpendicular to the surface is governed by Eq. (6). It was shown in [2] that steady-state evaporation from a planar water surface causes the temperature change only in the layer thinner than 1 cm above the water surface. Since the scale of our experimental setup is much larger, the temperature is assumed to be constant, $T = 293$ K. These simplifications significantly reduce the complexity of Eqs. (12) and (13). Furthermore, it enables Eq. (15) to be rewritten as

$$\frac{\Delta S}{k_B} = \ln \left(\frac{p_{\text{sat}}(T_l)}{p_v} \right) + \frac{V_l}{k_B T_l} [p_l - p_{\text{sat}}(T_l)]. \quad (17)$$

By comparison of the current equation with (15) it becomes obvious that the complexity is significantly reduced.

Water evaporation and change of RH in the cylinder is a dynamic but slowly evolving process. Therefore, we apply the so-called transient approach in which we divide the whole process into short time steps in which we consider the conditions to be the steady state. Thus, Eq. (6) can be applied for each time step. The transient solving procedure is then done by adaptive time stepping where the relative convergence tolerance is set to 10^{-4} .

All simulations were carried out using the finite element software COMSOL MULTIPHYSICS. RH given by

$$\theta = \frac{p_v}{p_{\text{sat}}} \quad (18)$$

has been modeled assuming the water vapor to be an ideal gas, hence

$$p_v = cRT, \quad (19)$$

where R is the ideal gas constant. The vapor concentration c follows Eq. (1) and $D_c = 2.4 \times 10^{-5} \frac{\text{m}^2}{\text{s}}$ at room temperature and atmospheric pressure according to [15]. The saturated water vapor pressure $p_{\text{sat}}(T) = 2.45$ kPa at $T = 293$ K [16].

TABLE I. Parameters used for viscosity calculation.

	$v_0 (\frac{\text{Ns}}{\text{m}^2})$	$T_0 (\text{K})$	n_v
v_a	1.716×10^{-5}	273	0.666
v_v	1.12×10^{-5}	350	1.15

The dynamic viscosity of humid air was obtained from [17] as

$$v_m = \sum_{i=1}^2 \frac{X_i v_i}{\sum_{j=1}^2 X_j \Phi_{ij}}, \quad (20)$$

where X_i is the mole fraction of air or water vapor (X_a for air and X_v for water vapor). The dynamic viscosity for air v_a and water vapor v_v are both obtained from

$$v_i = v_0 \left(\frac{T}{T_0} \right)^{n_v}, \quad (21)$$

where the corresponding values of v_0 and T_0 for air and water vapor are shown in Table I. Lastly,

$$\Phi_{ij} = \frac{1}{\sqrt{8}} \left(1 + \frac{M_i}{M_j} \right)^{-1/2} \left[1 + \sqrt{\frac{v_i}{v_j}} \left(\frac{M_j}{M_i} \right)^{1/4} \right]^2, \quad (22)$$

where M_i is the molar mass of the i th component.

To mimic RH at the open end of the cylinder the following concentration boundary is applied:

$$c_0 = 5.02 \frac{\text{mol}}{\text{m}^3}, \quad (23)$$

which corresponds to a relative humidity of 50% at $T = 293$ K. This is the case when the humidity evolution is considered through the sheer diffusion.

However, one can suspect that the setup is not completely free of convection. Possible convection at the boundary is introduced as a downward flow with the velocity:

$$\vec{u}_0 = -u_0 \frac{m}{s} \hat{y}, \quad (24)$$

where the choice of the constant u_0 will be elaborated in Sec. V. The water vapor flux at the water surface is obtained by combining Eqs. (6), (8), and (17).

The simulation is carried out using the CFD and chemical species transport modules within COMSOL with an adaptive time stepper. With the boundary conditions used for the

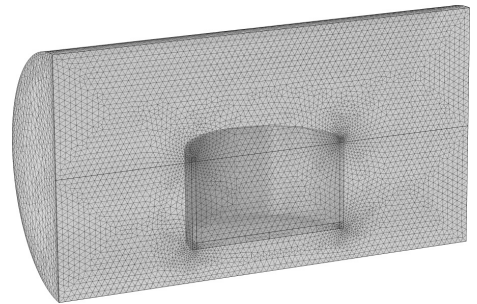


FIG. 2. Mesh used for the simulation of the setup containing the large water vessel.

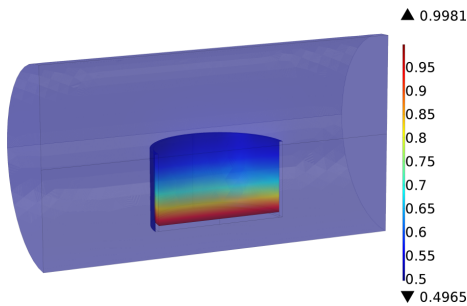


FIG. 3. (Color online) Initial profile of the relative humidity for the simulation with a large water vessel. Color scale shows RH.

velocity in this study, Reynolds number is found to be $Re \sim 30$, thus corresponding to a laminar flow regime. Due to the symmetry, only half of the cylindrical setup is modeled as shown in Fig. 1. The velocity profile is obtained by solving Eq. (3) together with (4) and (5). For the pressure-velocity coupling a so-called projection method is used [18,19]. The continuity equation for the water vapor (1) is combined with Eqs. (2), (6), and (17) and iteratively solved at every time step.

The mesh was generated using COMSOL. For the simulation of the setup with the large vessel a total number of 631 940 elements is used. The mesh is shown in Fig. 2. For the simulation with the small water vessel the total number of elements is reduced to 494 643. The reason for the larger number of elements used in the simulation for the large vessel is to have the same mesh density at the evaporation areas for the large and small vessels.

An initial RH profile with still standing air is shown in Fig. 3.

IV. EXPERIMENT

The setup consists of a cylindrical tube made of Pyrex glass attached to an aluminum plate and tightened with rubber gaskets. The plate has an electrical feedthrough for connection of a temperature and humidity sensor. The cylinder is 20 cm long and has a radius of 5.5 cm. A schematic of the setup can be seen in Fig. 4.

The setup is placed in a clean room with well controlled surrounding temperature of 293 ± 0.5 K and RH of 49%–51%. A sensor is placed inside the setup to control the temperature and humidity. The sensor is Sensirion SHT75 which covers the temperature range from 233 to 373 K and the RH range from 0% to 100% with a maximum uncertainty of $\pm 5\%$.

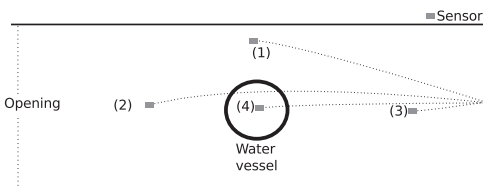


FIG. 4. Schematic top view of the experimental setup.

Prior to the experiments, readings of the sensor placed in the setup were compared with that of another sensor located outside. If the difference was greater than 5%, the sensor inside the setup was calibrated using the standard procedure recommended by the manufacturer.

Two kinds of experiments were conducted. The first series is referred to as flux experiments. A glass vessel with 10 ml of milli-Q water ($T = 273$ K) was put in the middle of the cylinder and the open side was tightly covered by a linen napkin to block convection. This napkin (Valusorb from Berkshire) is made of nonwoven polyester and cellulose and it has a structure with linear bundles of curled fibers. It is proven to be highly permeable to humid air but it should efficiently block convection due to the fact that the gaps in the napkin are on the micrometer scale. The amount of water evaporated from a vessel for a given time was measured by weighing the vessel before and after the experiment. Then the flux of evaporation was calculated.

The second series was carried out by placing a vessel of milli-Q water in the middle of the cylinder, tightly covering the open side by a linen napkin and monitoring the RH inside the setup until the steady state was reached. Again, the water temperature was 293 K. The spatial distribution of RH inside the setup was mapped by repeating such experiments with the humidity sensor placed at various locations.

Throughout both experimental series two water vessels were used. The large vessel has an inner radius of 3.5 cm and the small vessel has an inner radius of 2 cm.

RH was measured at 9 different positions inside the setup. In this paper we present the results for only four of them to avoid overloading with the similar experimental data and to focus on the most typical obtained dependencies. These positions can be seen in Fig. 4: (1) beside the vessel, (2) in front of vessel, (3) behind the vessel, and (4) above the vessel.

V. RESULTS AND DISCUSSION

A. Flux measurements and modeling

The measured fluxes and those modeled with the sheer diffusion are shown in Table II. The data presented in the experimental column are mean values obtained from three experiments with different times of evaporation which varied between 21 and 24 hours. As can be seen, the modeled values are smaller than the mean measured ones. However, the order of magnitude is the same. Taking into account that the fluxes are extremely small, one can conclude about good

TABLE II. Calculated fluxes using the approximation of sheer diffusion and experimentally measured fluxes. The fluxes have been calculated using Eq. (6), combined with Eqs. (8) and (17). Flux ratios between the small and large vessels are given for both model and experiment. The area ratio between the vessels is $A = 0.33$.

	Calculated flux	Measured flux
Small vessel	$1.05 \times 10^{-4} \frac{\text{mol}}{\text{s m}^2}$	$(3.15 \pm 0.25) \times 10^{-4} \frac{\text{mol}}{\text{s m}^2}$
Large vessel	$0.67 \times 10^{-4} \frac{\text{mol}}{\text{s m}^2}$	$(2.32 \pm 0.1) \times 10^{-4} \frac{\text{mol}}{\text{s m}^2}$
Flux ratio	1.57	1.36 ± 0.05

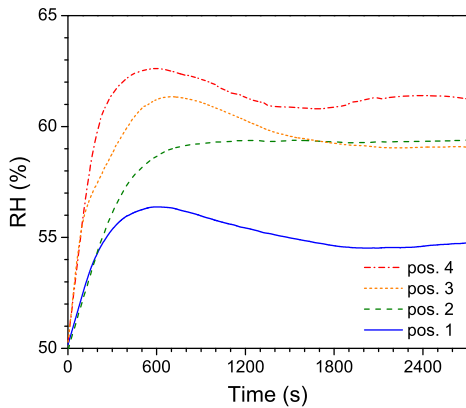


FIG. 5. (Color online) Change of RH with time for different sensor positions in the setup with the small vessel.

agreement between the simulations and the experiments. It is worth noting that in both model and experiment the flux is greater for the small vessel. This fact is related to the change in the configuration of the setup. The larger vessel takes up more space in the cylinder that changes the distribution of the surrounding water vapor and thus the flux is slightly reduced.

B. RH spatial distribution and time evolution

The measured changes of RH as a function of time are shown in Figs. 5 and 6 for the cases of small and large vessels, respectively. All the measurements reveal that RH reaches steady state after approximately 1800–2400 s. It is noticed that small bumps occur on the curves with maxima at around 500–600 s for both cases and sensor positions (1) and (3). These short-term increases of RH will be discussed later.

As a first step, simulations have been done with diffusion as the only transport mechanism, and a snapshot of a typical

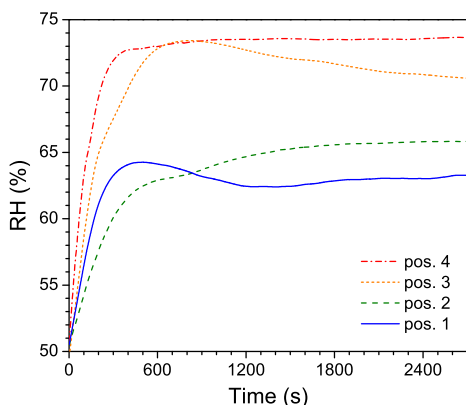


FIG. 6. (Color online) Change of RH with time for different sensor positions in the setup with the large vessel.

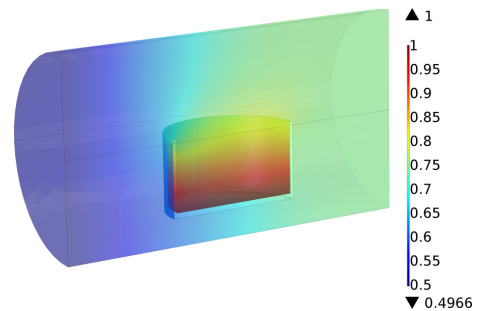


FIG. 7. (Color online) Simulated RH after 4000 s for the case of shear diffusion with a large water vessel. Color scale shows RH.

RH profile 4000 s after putting the vessel with water into the setup is shown in Fig. 7. The time corresponds to steady state of RH in the entire cylinder. The snapshot shows that the humidity is highest just above the vessel. It is lower closer to the cylinder end wall and it is lowest near the open side covered by the napkin. These tendencies qualitatively agree with the experimental measurements. Comparisons between the measured and modeled RH on the time scale are shown in Figs. 8 and 9, where the error bars indicate the maximum measurement uncertainty provided by the sensor manufacturer. The comparison reveals that in the case of the small vessel the model gives a reasonable prediction of RH evolution for position (2): The simulated curve is within the error bars of the measurements. However, RH values are overestimated by the simulations on the long time scale for position (1). It is also clear that the model does not predict the appearance of the short-term increase of the RH, so-called bumps, at the initial stage of the experiment. Very similar tendencies are found in the case of the large vessel (see Fig. 9). For the nonshown sensor positions (3) and (4) the model also demonstrates

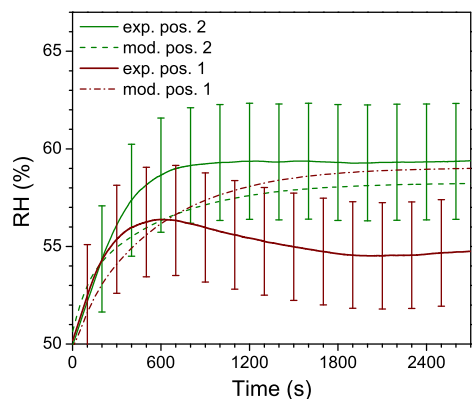


FIG. 8. (Color online) Experimental and modeled dependencies of RH on time for the setup with the small vessel and sensor positions (1) and (2). For the experimental curves, deviations due to the uncertainty of the sensor are shown as vertical bars.

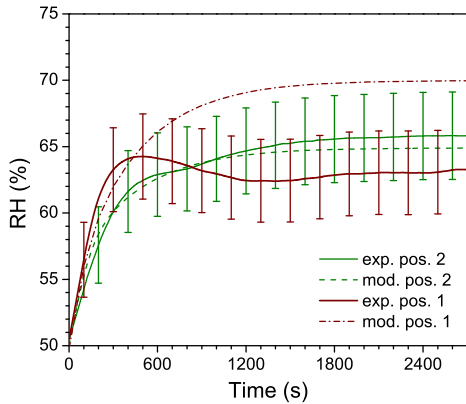


FIG. 9. (Color online) Experimental and modeled dependencies of RH on time for the setup with the large vessel and sensor positions (1) and (2). For the experimental curves, deviations due to the uncertainty of the sensor are shown as vertical bars.

only partial agreement with the experiment. Thus, one can conclude that the first simple model qualitatively predicts the RH distribution and time evolution in the setup but it probably misses some important phenomenon, which can be a convection term.

C. The role of convection

To test the role of convection and to improve the model, a boundary condition expressed by Eq. (24) is used. As an example, RH evolution is modeled for sensor position (1) and small vessel. For this case a few different values of u_0 were applied in Eq. (24) in order to investigate how convection affects the shape of the curves. The simulated evolutions of RH for three values of u_0 are presented in Fig. 10 for sensor position (2).

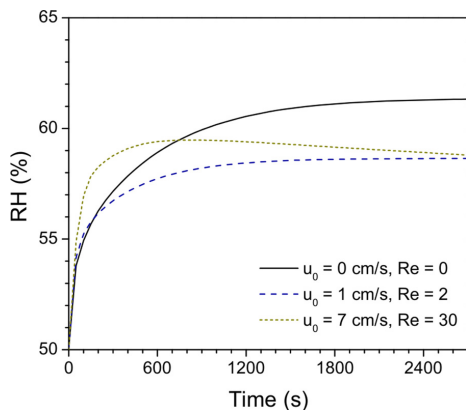


FIG. 10. (Color online) Modeled dependencies of RH on time for the cases of no convection ($u_0 = 0$ cm/s) and small convection velocities shown in the panel. The modeling is carried out for the setup with the small vessel at sensor position (2).

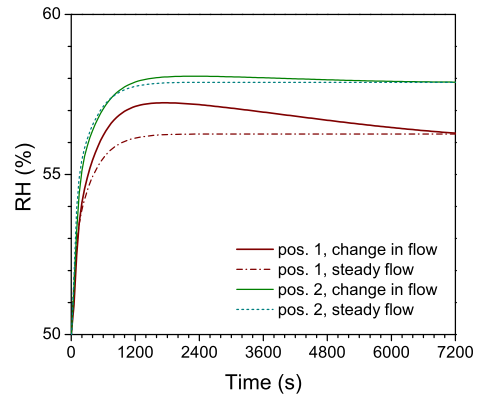


FIG. 11. (Color online) Modeled dependencies of RH on time for the case of convection with $u_0 = 2$ cm/s. For both sensor positions the simulation is done with time evolving (change in flow) and steady flows. See text for details.

First, the simulations show that adding even very small convection with $u_0 = 1$ cm/s corresponding to $Re = 2$ leads to a lowering of RH at the steady state. Second, further increase of the boundary velocity causes the appearance of a bump on the RH curve, thus, qualitatively reproducing the experimental measurements. Moreover, the initial rise of RH becomes much faster.

To get a better understanding of the physical reasons for the bumps on the humidity curves, two simulations for the case of the small vessel were done with $u_0 = 2$ cm/s ($Re = 17$). In the first simulation, the time evolution of RH is calculated using the assumption that the air is initially still in the cylinder but at $t = 0$ s the convection starts that leads to an evolving velocity profile until the steady-state velocity is reached. For the second simulation, the steady-state velocity profile obtained in the first simulation was used from the very beginning. The results of both simulations are presented in Fig. 11 for sensor positions (1) and (2). As seen in the figure, the first simulation is referred to as the time evolving flow and the second simulation as the steady-state flow.

One can see in Fig. 11 that the bumps occur only when a transient change in the air flow is present. By comparing these simulated curves with the experimental ones presented in Fig. 8 one can find good agreement in maximum and steady-state values of RH for both sensor positions. This allows one to conclude that the bumps are caused by convection introduced due to a short-term disturbance of air. This disturbance is assigned to the placement of the vessel inside the setup in the very beginning of the experiment causing unintentional movement of air which can include some nonlinear phenomena. It is worth noting that in the other series of experiments (not described here) the empty vessel placed in the setup was filled with water through a plastic pipe from outside thus minimizing possible unintentional air disturbances. In this case no bumps were observed, hence, proving our conclusion.

As one can see by comparing Figs. 11 and 8, the bump on the simulated curve is delayed with respect to the experimental one. Since it is hardly possible to measure the initial flow

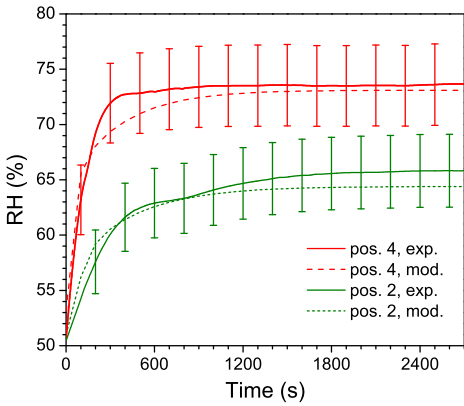


FIG. 12. (Color online) Experimental and modeled dependencies of RH on time for the setup with the large vessel. For the experimental curves, deviations due to the uncertainty of the sensor are shown as vertical bars. The simulated curves are based on the model including convection.

introduced by the moving vessel it cannot be expected that the model accurately predicts the bump appearances on the time scale.

By including convection and time evolving flow we also found good agreements between the simulations and experimental data on RH evolution for sensor positions (3) and (4) in the case of the small vessel as well as for all four positions in the case of the large vessel. In the simulations, the best agreement between the model and experiment was reached when the convection velocity was chosen to be between 1 and 2 cm/s. To demonstrate good agreement, a comparison of simulations and measurements for two sensor positions and the case of the large vessel is shown in Fig. 12. As one can see the model predicts the humidity evolution very accurately when the steady state is reached.

A snapshot of a typical, simulated RH profile in the setup with convection is shown in Fig. 13. The boundary condition $u_0 = 1$ cm/s. When comparing with the profile presented in Fig. 7 it can be noticed that the RH becomes more evenly distributed when convection is included in the model.

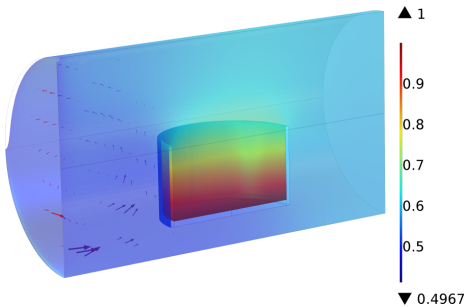


FIG. 13. (Color online) Simulated RH after 4000 s with $u_0 = 1$ cm/s for the case of the setup with the large water vessel. Color scale shows RH and the arrows indicate air flow.

TABLE III. Calculated fluxes and experimentally measured fluxes. The calculations include the slow convection process as discussed in the text. The fluxes have been calculated using Eq. (6), combined with Eqs. (8) and (17).

	Calculated flux	Measured flux
Small vessel	$1.17 \times 10^{-4} \frac{\text{mol}}{\text{s m}^2}$	$(3.15 \pm 0.25) \times 10^{-4} \frac{\text{mol}}{\text{s m}^2}$
Large vessel	$0.89 \times 10^{-4} \frac{\text{mol}}{\text{s m}^2}$	$(2.32 \pm 0.1) \times 10^{-4} \frac{\text{mol}}{\text{s m}^2}$
Flux ratio	1.31	1.36 ± 0.05

Adding the convection to the simulations also requires corrections of the water evaporation flux. New calculated data are presented in Table III showing better agreement with the experiment. There is still a difference between the modeled and the measured fluxes but one can see that the simulated and measured ratio values become the same within the standard deviations interval.

VI. CONCLUSION

We have studied relative humidity distribution in a simple cylindrical setup filled with air and containing a vessel with freely exposed water. This system imitates a box or cabinet at outdoor conditions in which the previously condensed water affects the spatial humidity profile through evaporation. This is a simplified model system which is of interest for reliability engineering. The spatial humidity distribution is studied both experimentally and theoretically.

In the experiments the flux of water evaporated from a vessel is measured and found to be small, on the order of $10^{-4} \frac{\text{mol}}{\text{s m}^2}$. Thus, the relative humidity increase due to the evaporation can be considered to be a dynamical but slowly evolving process. The change in RH and its time evolution is obtained at different sensor positions in the setup and for two configurations with the water vessels of different sizes. Experimental data are compared with the modeling. The model for simulation of spatial humidity distribution is based on statistical rate theory and computational fluid dynamics. It utilizes macroscopic quantities and the modeling is carried out by simultaneous solving of the Navies-Stokes and continuity equations for the water vapor. In our approach we use SRT for a number of sequent short-term steady-state time steps to simulate a slowly evolving dynamic system. The model is developed in two stages. At the first stage the diffusion is considered to be the only transport mechanism for the water vapor. This allows one to reach qualitative agreement with the experimental results but the model fails to predict correct RH values at the steady state and the effect of short-term rise of the humidity in the beginning of the experiment. The second stage introduces convection as an additional transport phenomenon, and thus significantly improves the model. One can conclude about its suitability for the prediction of RH spatial profiles in containers with simple geometry. Moreover, by including and tuning the convective flow one can further develop the approach towards modeling of more complex geometries, for instance containers with openings, and thus coming closer to the systems of practical engineering interest.

ACKNOWLEDGMENTS

This work is a part of research activities within the Center of Reliable Power Electronics (CORPE) funded by the Danish Strategic Research Council. We would like to acknowledge

the company Grundfos for providing the experimental setup. We would also like to thank Jens Peter Krog from Grundfos and Dietmar Weiss from Danfoss for useful comments on the manuscript.

-
- [1] R. Meland, A. Frezzotti, T. Ytrehus, and B. Hafskjold, *Phys. Fluids* **16**, 223 (2004).
 - [2] M. Bond and H. Struchtrup, *Phys. Rev. E* **70**, 061605 (2004).
 - [3] T. Ytrehus and S. Østmo, *Int. J. Multiphase Flow* **22**, 133 (1996).
 - [4] S. Cheng, J. B. Lechman, S. J. Plimpton, and G. S. Grest, *J. Chem. Phys.* **134**, 224704 (2011).
 - [5] K. Yasuoka, M. Matsumoto, and Y. Kataoka, *J. Chem. Phys.* **101**, 7904 (1994).
 - [6] T. Tsuruta, H. Tanaka, and T. Masuoka, *Int. J. Heat Mass Transfer* **42**, 4107 (1999).
 - [7] J. Caputa and H. Struchtrup, *Physica A* **390**, 31 (2011).
 - [8] S. Hardt and F. Wondra, *J. Comput. Phys.* **227**, 5871 (2008).
 - [9] G. Fang and C. A. Ward, *Phys. Rev. E* **59**, 417 (1999).
 - [10] C. A. Ward and G. Fang, *Phys. Rev. E* **59**, 429 (1999).
 - [11] C. A. Ward and D. Stanga, *Phys. Rev. E* **64**, 051509 (2001).
 - [12] H. Bruus, *Theoretical Microfluidics*, Oxford Master Series in Physics (Oxford University Press, Oxford, 2008).
 - [13] S. Chapman and T. Cowling, *The Mathematical Theory of Non-Uniform Gases: An Account of the Kinetic Theory of Viscosity, Thermal Conduction and Diffusion in Gases*, Cambridge Mathematical Library (Cambridge University Press, Cambridge, 1970).
 - [14] A. Kapoor and J. A. Elliott, *J. Phys. Chem. B* **112**, 15005 (2008).
 - [15] T. Marrero and E. A. Mason, *J. Phys. Chem. Ref. Data* **1**, 3 (1972).
 - [16] R. Weast and M. J. Astle, *CRC Handbook of Chemistry and Physics: A Ready Reference Book of Chemical and Physical Data* (CRC Press, Boca Raton, FL, 2013).
 - [17] J. Zhang, A. Gupta, and J. Baker, *Heat Transfer Eng.* **28**, 335 (2007).
 - [18] *COMSOL Multiphysics: Version 4.3b. User's Guide* (Comsol, 2013).
 - [19] J. Guermond, P. Mineev, and J. Shen, *Comput. Methods Appl. Mech. Eng.* **195**, 6011 (2006).

Paper B

Free surface entropic lattice Boltzmann simulations
of film condensation on vertical hydrophilic plates

Morten A. Hygum, Iliya V. Karlin, Vladimir N. Popok

The paper has been published in the
International Journal of Heat and Mass Transfer Vol. 87, pp. 576–582, 2015.

© 2015 Elsevier
The layout has been revised.



Free surface entropic lattice Boltzmann simulations of film condensation on vertical hydrophilic plates

Morten A. Hygum^{a,*}, Iliya V. Karlin^b, Vladimir N. Popok^a

^a Department of Physics and Nanotechnology, Aalborg University, 9220 Aalborg, Denmark

^b Department of Mechanical and Process Engineering, ETH Zurich, 8092 Zurich, Switzerland

ARTICLE INFO

Article history:

Received 9 January 2015

Received in revised form 31 March 2015

Accepted 11 April 2015

Keywords:

Film condensation

Entropic lattice Boltzmann

Free surface lattice Boltzmann

ABSTRACT

A model for vapor condensation on vertical hydrophilic surfaces is developed using the entropic lattice Boltzmann method extended with a free surface formulation of the evaporation–condensation problem. The model is validated with the steady liquid film formation on a flat vertical wall. It is shown that the model is in a good agreement with the classical Nusselt equations for the laminar flow regime. Comparisons of the present model with other empirical models also demonstrate good agreement beyond the laminar regime. This allows the film condensation modeling at high film Reynolds numbers without fitting, tuning or empirical parameters.

© 2015 Elsevier Ltd. All rights reserved.

1. Introduction

Condensation processes play a crucial role in various engineering and scientific aspects affecting energy conversion, safety and reliability issues as well as design aspects of devices and constructions. Condensation can be divided into two main types: dropwise and film condensation [1,2]. Dropwise condensation occurs on hydrophobic surfaces. Alternatively, condensate can wet the surface and form a film. This case is typical for hydrophilic surfaces. Since the thermal resistance is low at dropwise condensation the heat transfer is significantly higher than for the film condensation. Moreover, in order to consider droplet formation, a number of parameters need to be taken into account and modeling becomes rather involved. Therefore, a majority of the models are developed for the film condensation.

The first model for film condensation was introduced almost a century ago by Nusselt [3]. Nevertheless, Nusselt's model remains very popular and it is often used because in this case the closed-form analytical solution is available. Nusselt's model assumes (i) a linear temperature distribution across the film condensate, (ii) constant film properties, (iii) the shear stress at the surface and inertia effects are negligible, (iv) laminar flow in the forming film, and (v) pure still vapor from which the condensation occurs. In Fig. 1 an illustration of the system considered by Nusselt is shown. Nusselt obtained analytical expressions for the velocity profile in the film, the film thickness, mass flow and the heat transfer coefficient along a hydrophilic wall.

Nusselt's model has been found to have a good accuracy but only for low flow velocities [2]. One of the reasons for low accuracy at high flow velocities is the neglect of inertia and interface shear effects. The role of these effects has been intensely studied in the literature and it has been found that at low Prandtl numbers the interface shear must be taken into account while at high Prandtl numbers the effect of shear is small and can be neglected [4,5]. Both effects (inertia and interface shear) lower the mass flow rate. Also, subcooling effects are discarded in Nusselt's model which may alter the condensation flux at the liquid–gas interface. In [2] it is shown how the above effects can be taken into account.

Nusselt's model also assumes a laminar film without ripples or waves at the interface. This assumption has been studied and found to be valid for film Reynolds numbers $Re_f \leq 33$ [6]. To classify different condensation flows the film Reynolds number is defined as

$$Re_f = \frac{4\dot{m}(z=L)}{\mu_l}, \quad (1)$$

where \dot{m} is the mass flow in the bottom of the film at the length L and μ_l is the dynamic viscosity of the film. For $Re_f \geq 33$ the condensate film turns wavy-laminar and for $1000 \leq Re_f \leq 1800$ the flow in the film becomes turbulent [2]. These surface wave and turbulence effects have been suggested to alter the film thickness that leads to a significant change in the heat transfer coefficient. Therefore, it is normal practice to use empirical correlations for these regimes [1,2].

On the other hand, the lattice Boltzmann (LB) method has over the last two decades become a successful numerical approach to

* Corresponding author.

efficiently simulate various complex flows [7–14]. Different LB methods for multiphase flows have been suggested [15] and recently a LB model to predict film and dropwise condensation was developed [16,17] using the so-called Shan-Chen multiphase method. It was, however, reported that the model becomes numerically unstable if the Prandtl number deviates from one. Furthermore, a general issue using the Shan-Chen method is that the interface between the vapor and the liquid is diffuse [15].

To address tracking of interfaces between the gas and liquid phases as well as further strengthen the model, a free surface LB (FSLB) methods have been developed [18–20]. However, to ensure numerical stability, adaptive time steps [19] or adaptive grids [21] need to be implemented in the model which causes a significant complication.

In this paper we suggest a free surface entropic LB (FSELB) model and demonstrate how the model can be used to predict film condensation. Unlike the previous LB models, the entropic LB scheme in the free-surface framework demonstrates excellent stability and accuracy without considering adaptive grid or time steps. Furthermore, the model is not limited to laminar flows and, thus, it is applicable to laminar, wavy-laminar and turbulent film flows. We consider the construction in detail in two dimensions (2D); extension to 3D is straightforward.

It is worth mentioning that a lattice Boltzmann condensation model with no limitation on model parameters has not been developed so far. Moreover, the presented model is the first FSELB model. Finally, adding mass transfer to the liquid–vapor interface in FSLB methods is an extension which to our best knowledge have not been reported before. Thus, FSELB allows for modeling of more complex processes, e.g. evaporation and condensation.

The outline of the paper is as follows: in Section 2.1 the entropic lattice Boltzmann (ELB) model will be described and in Section 2.2 the modeling of the temperature field is presented. In Section 2.3 the FSLB method developed in [19] is reviewed and in order to validate the FSELB model the key concepts and equations of Nusselt's model are presented in Section 2.4. Finally, in Section 2.5 the set-up of our model will be described showing how it is developed from the FSLB framework. The results are presented and discussed in Section 3 while Section 4 concludes the paper.

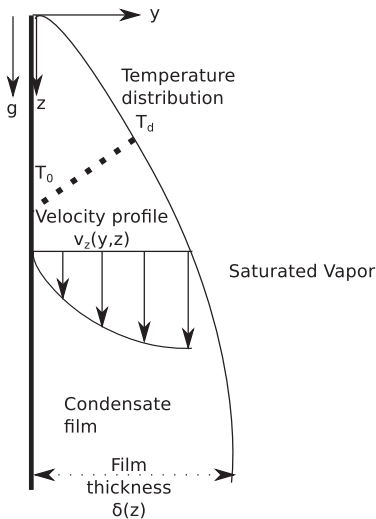


Fig. 1. Film condensation on a vertical surface according to Nusselt's model. T_w is the wall temperature and T_d is the temperature at the interface between the gas and liquid phase.

2. Model descriptions

The 2D FSELB model, presented here, is constructed using the ELB approach for modeling of the flow in the film. The liquid–gas interface is treated as a boundary according to the FSLB framework and the temperature field is treated as a passive scalar described below in Section 2.2.

2.1. Entropic lattice Boltzmann

The LB method concerns a discrete kinetic equation which solves for populations $f_i(\vec{x}, t)$ corresponding to discrete velocities $\vec{c}_i, i = 1, \dots, n_d$. The velocities fit into a regular spatial lattice with the nodes \vec{x} . The ELB method is a generalization of the LB method and involves restoring the second law of thermodynamics. This additional step renders excellent non-linearly numerical stability and drastically reduces the computational demand at high Reynold numbers [11,22].

The ELB equation with the lattice Bhatnagar–Gross–Krook (LBGK) collision operator including a body force is given as [11]

$$f_i(\vec{x} + \vec{c}_i dt, t + dt) = f_i(\vec{x}, t) + \alpha \beta (f_i^{eq}(\rho, \vec{u}) - f_i(\vec{x}, t)) + f_i^{eq}(\rho, \vec{u} + \Delta \vec{u}) - f_i^{eq}(\rho, \vec{u}), \quad (2)$$

where β is related to the kinematic viscosity ν as follows:

$$\nu = c_s^2 \left(\frac{1}{2\beta} - \frac{1}{2} \right) dt. \quad (3)$$

Here, c_s is the speed of sound in the model, dt is the time step, ρ is the density, \vec{u} is flow velocity, and α is the non-trivial root of the entropy estimate which will be described below. The density and momentum are obtained from the populations as:

$$\rho = \sum_{i=1}^{n_d} f_i \quad (4)$$

and

$$\rho \vec{u} = \sum_{i=1}^{n_d} \vec{c}_i f_i. \quad (5)$$

The body force is incorporated using the exact difference method which provides the expression for the velocity increment $\Delta \vec{u}$ as [23]

$$\Delta \vec{u} = \frac{\vec{F}}{\rho} dt, \quad (6)$$

where the force $\vec{F} = \vec{g} \rho$ with \vec{g} to be the gravitational acceleration. The actual fluid velocity \vec{U} is obtained by averaging the fluid momentum before and after the collision:

$$\rho \vec{U} = \rho \vec{u} + \frac{dt \vec{F}}{2}. \quad (7)$$

The equilibrium function f_i^{eq} is the minimizer of the discrete entropy function H under local conservation laws of mass and momentum. The entropy function is given as

$$H = \sum_{i=1}^{n_d} f_i \ln \frac{f_i}{W_i}, \quad (8)$$

with W_i to be the lattice specific weights. Expanding the minimization problem to the order u^2 gives rise to

$$f_i^{eq}(\rho, \vec{u}) = \rho W_i \left(1 + \frac{\vec{c}_i \cdot \vec{u}}{c_s^2} + \frac{(\vec{c}_i \cdot \vec{u})^2}{2c_s^4} - \frac{\vec{u} \cdot \vec{u}}{2c_s^2} \right). \quad (9)$$

The entropy balance is maintained at each node for each time step through the parameter α . It is obtained as the non-trivial root of the following equation:

$$H(f) = H(f + \alpha(f^{eq} - f)). \quad (10)$$

In order to ensure an efficient simulation the following asymptotic expansion for α is used for the condition $|(f_i^{eq} - f_i)/f_i| < 10^{-2}$ [24]:

$$\alpha = 2 - \frac{4a_2}{a_1} + \frac{16a_2^2}{a_1^2} - \frac{8a_3}{a_1} + \frac{80a_3a_2}{a_1^2} - \frac{80a_2^3}{a_1^3} - \frac{16a_4}{a_1}, \quad (11)$$

with the coefficients a_n obtained from

$$a_n = \frac{(-1)^{n-1}}{n(n+1)} \sum_{i=1}^{n_d} \frac{(f_i^{eq} - f_i)^{n+1}}{f_i^n}, \quad n \geq 1. \quad (12)$$

If $|(f_i^{eq} - f_i)/f_i| > 10^{-2}$ then α is found using the bi-section method.

The D2Q9 lattice [8] is chosen for the model. For that lattice

$$\begin{aligned} c_x &= (0, 1, 0, -1, 0, 1, -1, -1, 1), \\ c_y &= (0, 0, 1, 0, -1, 1, 1, -1, -1), \\ W &= (4/9, 1/9, 1/9, 1/9, 1/9, 1/36, 1/36, 1/36, 1/36), \end{aligned} \quad (13)$$

and $c_s = 1/\sqrt{3}$.

ELBM was originally developed to stabilize simulations of high Reynolds number, with large velocity gradients. The film flows, considered here, are not such systems. However, ELBM can still be adapted to ensure better stability of free surface simulations. As shown later, in Section 3, the source of numerical instability for the free surface simulations carried out in this paper is found to be the surface itself. Utilizing the ELBM approach, thus, allows for better stability for a wider range of input parameters.

2.2. Temperature field

One of the simplest LB realizations for modeling the temperature T is to treat it as a passive scalar. As suggested in [25] the temperature field can, thus, be solved using a second lattice. Here, the D2Q9 lattice is also considered. More advanced models do exist which e.g. include viscous heating [26]. However, while neglecting these effects the kinetic equation for the second population, representing T , is given as [25]

$$g_i(\vec{x} + \vec{c}_i dt, t + dt) = g_i(\vec{x}, t) + 2\beta_T(g_i^{eq}(T, \vec{u}) - g_i(\vec{x}, t)), \quad (14)$$

where the thermal diffusivity

$$D_T = c_s^2 \left(\frac{1}{2\beta_T} - \frac{1}{2} \right) dt. \quad (15)$$

The temperature is obtained from $T = \sum_{i=1}^{n_d} g_i$ and the equilibrium function g_i^{eq} is

$$g_i^{eq}(T, \vec{u}) = TW_i \left(1 + \frac{\vec{c}_i \cdot \vec{u}}{c_s^2} \right). \quad (16)$$

Eq. (14) is acceptable for the use in our model. As mentioned, the source of numerical instability does not originate from the temperature field which is why the LBGK relaxation is sufficient.

2.3. Free surface modeling

The free surface modeling is based on the approach described in [19] and for the sake of completeness the key points are presented here.

In the free surface model the gas phase is assumed to have a negligible effect on the fluid flow in the film. Therefore, surface tension and shear stress at the liquid–vapor interface are discarded. Moreover, the contact angle at the top of the film is found to have a negligible effect when considering film condensation [16] which justifies the simplification. As in any numerical realization the domain is discretized with a suitable set of nodes. Every node has one of the following flags: fluid/filled node, interface node, or

an gas/empty node, where the complication lies within the treatment of the interface nodes. An overview of the surface handling is shown in Fig. 2.

2.3.1. Interface movement

The movement of the interface is modeled by keeping track of the mass m and the fluid fraction ϵ in each node. The fluid fraction $\epsilon = m/\rho$ is one ($\epsilon = 1$) for a filled node, zero for an empty node ($\epsilon = 0$), and $0 < \epsilon < 1$ for an interface node. Mass fluxes between the nodes are directly computed through the streaming step, which for an interface node at \vec{x} and a fluid node at $\vec{x} + \vec{c}_i$ becomes

$$\Delta m_i^f(\vec{x}, t + dt) = f_i(\vec{x} + \vec{c}_i, t) - f_i(\vec{x} + \vec{c}_i, t), \quad (17)$$

where \vec{i} is the opposite direction of i : $\vec{c}_i = -\vec{c}_{\vec{i}}$. The notation f denotes that the neighbor is a fluid node.

The mass exchange between two interface nodes must account for the area between the nodes. This is approximated by the average of the fluid fractions of the two nodes as follows:

$$\Delta m_i^l(\vec{x}, t + dt) = [f_i(\vec{x} + \vec{c}_i, t) - f_i(\vec{x} + \vec{c}_i, t)] \frac{\epsilon(\vec{x} + \vec{c}_i, t) + \epsilon(\vec{x}, t)}{2}, \quad (18)$$

where l denotes that the neighbor is an interface node. Thus, the mass of the interface node at \vec{x} at the next time step is given as

$$m(\vec{x}, t + dt) = m(\vec{x}, t) + \sum_{i=1}^{n_d} \Delta m_i^f(\vec{x}, t + dt), \quad (19)$$

with $k = \{F, I\}$.

2.3.2. Surface reconstruction

At the interface nodes the populations which would have streamed from the empty nodes are lacking and must therefore be reconstructed. It is assumed that the pressure at the interface gives rise to a density $\rho_A = 1$ and that the vapor does not affect the film flow. This allows for

$$f_i^f(\vec{x}, t + dt) = f_i^{eq}(\rho_A, \vec{u}) + f_i^{eq}(\rho_A, \vec{u}) - f_i(\vec{x}, t), \quad (20)$$

with f_i^f to be the post-streaming populations. Note that the surface tension can be included by modifying Eq. (20), see [27,28]. Using Eq. (20) we get a full set of populations. However, in order to balance

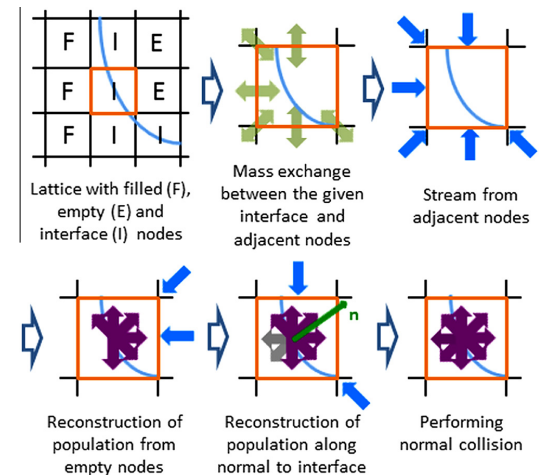


Fig. 2. Overview of the steps that have to be executed for the interface handling.

the force at each side of the interface, Eq. (20) is used for streaming along the direction of the normal vector \vec{n} to the surface. Thus, if

$$\vec{n} \cdot \vec{c}_i > 0, \quad \vec{n} = \frac{1}{2} \begin{pmatrix} \epsilon(\vec{x}_{j-1,k}) + \epsilon(\vec{x}_{j+1,k}) \\ \epsilon(\vec{x}_{j,k-1}) + \epsilon(\vec{x}_{j,k+1}) \end{pmatrix}, \quad (21)$$

with j being the x -coordinate and k being the y -coordinate, Eq. (20) is also used for the streaming.

2.3.3. Surface re-initialization

After the density and the momentum have been calculated it must be investigated whether the interface nodes have been filled or emptied during the time step. This is done according to:

$$\begin{aligned} m(\vec{x}, t + dt) &> (1 + \kappa)\rho(\vec{x}, t + dt) \rightarrow \text{node filled} \\ m(\vec{x}, t + dt) &< -\kappa\rho(\vec{x}, t + dt) \rightarrow \text{node emptied} \end{aligned} \quad (22)$$

where $\kappa = 10^{-4}$ is a threshold to prevent a re-initialization of the given node at the next time step. For implementation reasons the coordinate of the node of interest is stored in a separate list and the conversion is done when the main loop is executed for all nodes.

An empty node must have a mass equal to zero and a filled node must have a mass equal to the density times the volume. As in standard LB units we set $dx = dy = 1$ and $\rho = 1$. Therefore, the use of Eq. (22) inevitably leads to an excess mass m^{ex} which must be distributed to the neighboring interface nodes. The excess mass is given as following:

$$\begin{aligned} m^{\text{ex}} &= m \rightarrow \text{emptied node} \\ m^{\text{ex}} &= m - \rho dx dy \rightarrow \text{filled node.} \end{aligned} \quad (23)$$

It can be noticed, that if the emptied node has a numerically negative mass, the interface has moved beyond the current node. Similarly, if the mass of a filled node gives rise to a density larger than one the interface has moved past the node.

The conversion of the newly filled or emptied node must first be done. For a newly filled node the surrounding empty nodes are converted to interface nodes. For each of these nodes the average density ρ^{avg} and momentum $\rho^{\text{avg}} \vec{u}^{\text{avg}}$ are calculated considering the neighboring fluid and interface nodes. The newly converted interface nodes are then initialized with equilibrium functions $f_i^{\text{eq}}(\rho^{\text{avg}}, \vec{u}^{\text{avg}})$. Similarly, the fluid neighbors to the newly emptied nodes are converted to interface nodes. The former nodes population is used for each corresponding new interface node.

The last step is to distribute the excess mass to the neighboring interface nodes. The excess mass is weighted according to \vec{n} . Thus, the distribution of excess mass is calculated according to

$$m(\vec{c} + \vec{c}_i) = m(\vec{c} + \vec{c}_i) + m^{\text{ex}} \frac{\eta_i}{\eta_{\text{total}}}, \quad (24)$$

with η_{total} to be the sum of all the weights η_i , which are obtained according to

$$\eta_i = \begin{cases} \vec{n} \cdot \vec{c}_i & \text{if } \vec{n} \cdot \vec{c}_i > 0 \\ 0 & \text{otherwise} \end{cases} \quad \text{filled nodes} \quad (25)$$

$$\eta_i = \begin{cases} -\vec{n} \cdot \vec{c}_i & \text{if } \vec{n} \cdot \vec{c}_i < 0 \\ 0 & \text{otherwise} \end{cases} \quad \text{emptied nodes.}$$

With the excess mass distributed, the re-initialization is completed and the simulation can continue to the next time step. It can, however, happen that single interface nodes are left behind the flow or interface nodes get trapped inside the fluid. These are artifacts but they do not perturb the flow. In order to remove these artifacts the procedure described in [19] is applied.

2.4. The Nusselt model

With the LB framework of the model described we proceed with its validation. For that we need to introduce a few key equation of the Nusselt model described in [2] and refer once again to the condensation process illustrated in Fig. 1. The Nusselt formulas can be derived by considering the Navier–Stokes equation at steady-state combined with the enthalpy balance. The flow is due to gravity and the film thickness arises from the condensing mass flux at the liquid–vapor interface. The film thickness is obtained as

$$\delta(z) = \left[\frac{4k_l \mu_l (T_d - T_0) z}{\Delta h_{\text{vap}} \rho_l (\rho_l - \rho_g) g} \right]^{1/4}, \quad (26)$$

with k_l to be the thermal conductivity of the liquid, T_0 to be the wall temperature, T_d to be the temperature at the interface between the gas and liquid phases, Δh_{vap} to be the latent heat of condensation, ρ_l to be the density of the liquid, ρ_g to be the density of the gas, and g to be the acceleration due to gravity. The velocity profile v is given as

$$v = \frac{(\rho_l - \rho_g) g}{\mu_l} \left[y \delta - \frac{y^2}{2} \right] \quad (27)$$

and the mass flow rate \dot{m} is, according to Nusselt, given as

$$\dot{m} = \rho_l \frac{(\rho_l - \rho_g) g}{3 \mu_l} \delta^3. \quad (28)$$

The local heat transfer coefficient h is given as $h = k_l / \delta$ which leads to the average heat transfer coefficient as follows:

$$\bar{h} = \frac{4}{3} \frac{1}{4^{1/4}} \left[\frac{k_l^3 \Delta h_{\text{vap}} \rho_l (\rho_l - \rho_g) g}{\mu_l (T_d - T_0) L} \right]^{1/4} \approx 0.943 \left[\frac{k_l^3 \Delta h_{\text{vap}} \rho_l (\rho_l - \rho_g) g}{\mu_l (T_d - T_0) L} \right]^{1/4}, \quad (29)$$

where L is the length of the film. This allows for the non-dimensional Nusselt formula of the averaged heat flux:

$$H_f = \frac{\bar{h}}{k_l} \left[\frac{\mu_l^2}{\rho_l (\rho_l - \rho_g) g} \right]^{1/3} = 1.47 \text{Re}_f^{-1/3}. \quad (30)$$

With the theoretical foundation in place the set-up of our model will be presented below. The model is developed in the way that it can be compared with the Nusselt formulas as a benchmark.

2.5. Simulation set-up

Similar to the Nusselt formulation the surface tension is considered to be negligible and the pressure of the vapor is assumed to be constant and saturated in our model.

A computation domain of $N_x \times N_y = 300 \times 300$ is proven to yield grid independent results. At the wall boundary the no-slip condition and the temperature T_0 are applied. The no-slip condition is realized with the bounce-back method. The temperature at the interface is set to T_0 using the approach presented in [29] and at the bottom the extrapolation boundaries is applied according to the procedure suggested in the same reference. The top nodes are fixed as vapor nodes and therefore never addressed. At the interface the temperature T_d is enforced.

The condensation flux couples the energy equation to the mass flux at the interface. The energy conservation at the surface implies

$$k_l \vec{\nabla} T|_{\text{interface}} = k_g \vec{\nabla} T|_{\text{interface}} - \vec{J} \Delta h_{\text{vap}}, \quad (31)$$

with \vec{J} to be the condensation flux and k_g to be the thermal conductivity of the gas.

The contribution of the condensation flux is added to the right side of Eq. (19) for the mass at the interface, thus, converting it to

$$m(\vec{x}, t + dt) = m(\vec{x}, t) + \sum_{i=1}^{n_d} \Delta m_i^k(\vec{x}, t + dt) + A J dt, \quad (32)$$

with A to be the area of the surface at the given node. This area, which for 2D simulations correspond to a line, is found by assuming that the area of the interface can be approximated by a right-angled triangle. Note, that this additional mass flux is our extension to the FSELB framework to be able to address condensation-evaporation problems.

The fluid flow and heat transfer of steady film condensation on hydrophilic surfaces can be characterized by the following two dimensionless numbers:

$$Pr = \frac{v}{D_T} = \frac{c_p \mu_l}{k_l}, \quad Ja = \frac{c_p (T_d - T_0)}{\Delta h_{vap}}, \quad (33)$$

which are the Prandtl and Jakob numbers, respectively, and c_p is the specific heat at constant pressure. The Prandtl number is a material constant and the Jakob number is the ratio of the sensible heat of the film and the latent heat of the vapor. Thus, for a fixed Pr the film thickness will increase with the Jakob number since the energy flux at the interface increases.

3. Results and discussion

3.1. Comparisons of FSELB with the Nusselt model

In Fig. 3 film thickness modeled by the developed FSELB method and the classic Nusselt model are compared for two pairs of Prandtl and Jakob numbers, $Pr = 7$ and $Ja = 0.185$, and $Pr = 0.8$ and $Ja = 0.4$. These parameters were chosen, in order to demonstrate that the model works well within some range of input parameters. For all the simulations $L = 1$ mm, $g = 9.81$ m/s, $\rho = 10^3$ kg/m³, $\Delta h_{vap} = 2260$ kJ/kg, $\mu_l = 1.002 \cdot 10^{-3}$ Pa · s, k_l and $(T_d - T_0)$ is calculated from Pr and Ja , respectively. As in normal LB practice, the velocity is set so that it does not exceed 0.05 in lattice units. It is seen that our simulations agree well with those carried out using the analytical Nusselt formula.

Comparisons of z-components of the velocities between the two models are shown in Fig. 4 along with the film Reynolds numbers. The mass flow in the FSELB model is calculated by the following formula:

$$\dot{m} = \sum_{y=1}^{y_f} u_y \rho_y dy, \quad (34)$$

where y_f is the y-coordinate of the interface node at L . It can be seen that both models agree well for low length values. However, the

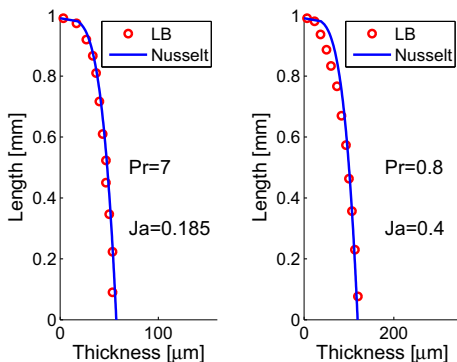


Fig. 3. Comparisons of film thicknesses predicted by FSELB simulation and Nusselt formula.

velocities predicted by the FSELB model are found to be smaller than those calculated by Nusselt model's and this difference increases with the velocity rise. Actually, this is expected behavior because the FSELB method takes into consideration the effects of inertia forces which lowers the velocity.

The same tendencies were found in [4,16] where the deviation was found to be the highest for high Jakob numbers and low Prandtl numbers. According to [4,16] inertia, shearing stress and viscous effects become increasingly important at high Jakob numbers and low Prandtl numbers which is where the present FSELB model also deviates from the Nusselt model.

The dimensionless temperature $\theta = \frac{T-T_0}{T_d-T_0}$ profile at L and mean heat transfer coefficient for the two models are compared in Fig. 5. It is seen that the linear approximation of the temperature is a quite suitable approach for predicting the mean heat transfer coefficient in the laminar regime.

In Fig. 6 the contours of T and v are shown for simulations with $Pr = 7$ and $Ja = 0.185$. The contours of T and v for simulations with $Pr = 0.8$ and $Ja = 0.4$ are presented in Fig. 7. Good agreement between the profiles modeled with FSELB and the Nusselt formulas can be seen.

3.2. Beyond the laminar regime

As mentioned in the introduction, the Nusselt model has experimentally been proven to be true only for $Re_f < 30$. Beyond this regime empirical expressions were developed. In this paper we use two expressions proposed by Kutateladze [30] and Chen et.

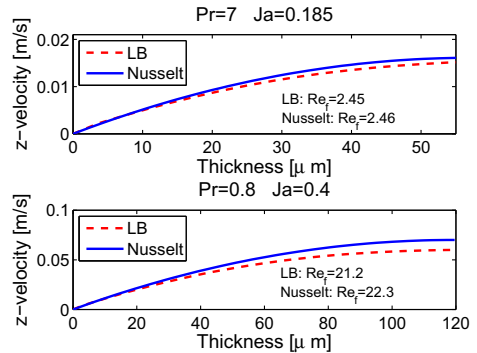


Fig. 4. Comparisons of z-components of the velocities predicted by FSELB simulation and Nusselt formula.

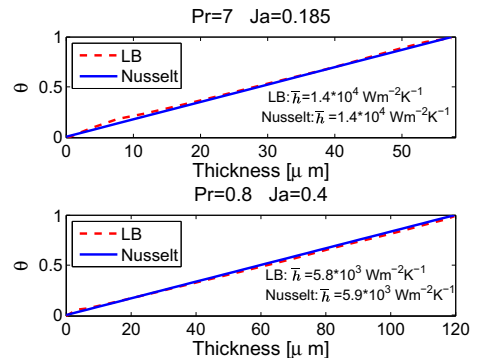


Fig. 5. Comparisons of dimensionless temperature profiles predicted by FSELB simulation and Nusselt formula.

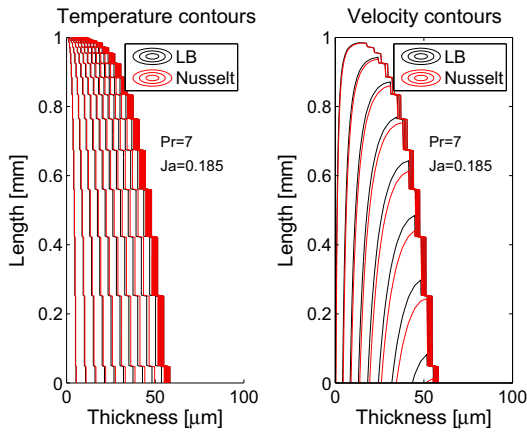


Fig. 6. Comparisons of temperature and velocity contour profiles predicted by FSELB simulation and Nusselt formula with $Pr = 7$ and $Ja = 0.185$.

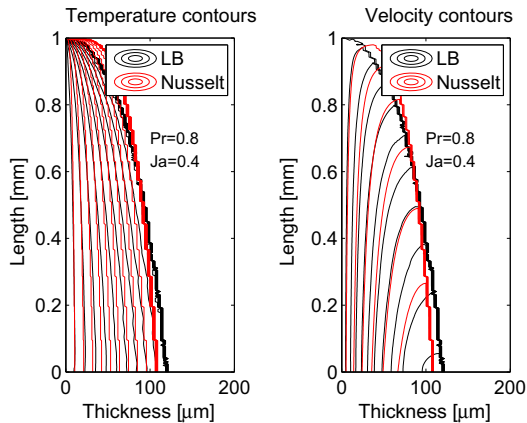


Fig. 7. Comparisons of temperature and velocity contour profiles predicted by FSELB simulation and Nusselt formula with $Pr = 0.8$ and $Ja = 0.4$.

al [31] for comparisons with our model. Since the presented model is in 2D, only comparisons for the wavy-laminar regime is carried out.

In Fig. 8 the non-dimensional averaged heat flux is compared to the Nusselt formula and the empirical models proposed by Kutateladze [30] and Chen et. al [31]. It can be seen, that the simulations using FSELB model show a reasonable agreement with the two empirical models for the range of used film Reynolds numbers while the Nusselt calculations significantly underestimate the flux especially for high Reynolds numbers.

It is worth mentioning that wave-like behavior of the film can be simulated by the presented FSELB approach with high enough resolution. To illustrate this, two simulations were conducted with same input parameters and initial conditions but with different resolutions, namely 600×600 and 3000×3000 grids. The simulations are carried out with $Pr = 0.8$, $Ja = 2.5$ and $L = 200$ mm. A snapshot of both simulations where $Re_f = 94.65$ can be found in Fig. 9. It is seen that the film becomes wave-like when simulated with high resolution. This indicates that the present approach can be used beyond the laminar flow regime. A detailed study of

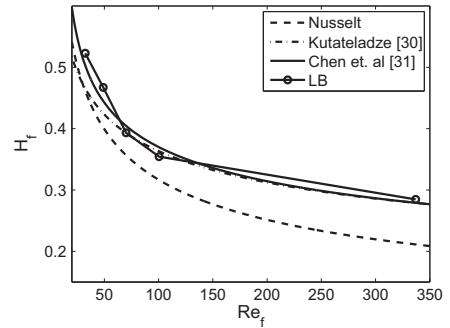


Fig. 8. Comparison of non-dimensional averaged heat fluxes predicted by the various models for the given range of film Reynolds numbers.

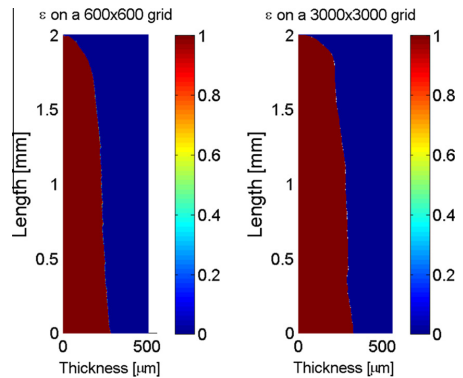


Fig. 9. Comparison of fluid fraction ϵ profiles at a snapshot where $Re_f = 94.65$. The simulations are carried out with two different resolutions shown in the panels.

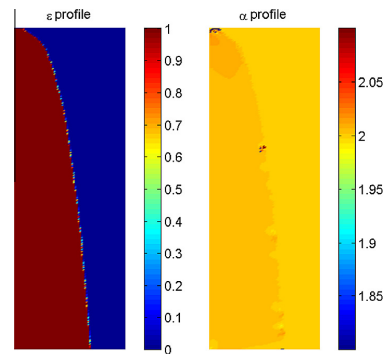


Fig. 10. A snapshot of the fluid fraction ϵ and α -profile of a condensation film flow where $L = 1.5$ mm, $Pr = 0.8$ and $Ja = 2.4$.

the corresponding effects require a three-dimensional extension of the model which is beyond the scope of the present paper.

Finally, a comment on the use of the entropic LB scheme instead of the conventional LBGK is in order. As mentioned earlier, the source of numerical instability in the free surface flows is the surface itself. To prove this a snapshot of the α -profile of a condensation film flow where $L = 1.5$ mm, $Pr = 0.8$ and $Ja = 2.4$ is shown in

Fig. 10. To visualize the film the fluid fraction ϵ is also shown in Fig. 10. This simulation was proven to be unstable with the standard LBGK but it is stable using the ELB model. In Fig. 10 it is seen that the entropic estimations are activated, at this snapshot, mainly in two places at the surface. Furthermore, the α values cover a range of 1.8 to 2.05. We remind that the conventional LBGK corresponds to the fixed value $\alpha = 2$. The need for the entropic stabilization is therefore clear.

4. Conclusion

A free surface entropic lattice Boltzmann approach has been introduced and the model is applied to predict steady laminar film condensation on a flat vertical hydrophilic surface. The model framework enables to reach Prandtl and Jakob numbers not reported before for lattice Boltzmann simulations of film condensation. Furthermore, the model allows film condensation modeling beyond the laminar regime and it shows good agreement with earlier developed empirical models in a relatively wide range of film Reynolds numbers.

The presented model is developed for simulations of saturated vapor. However, adjustment of the mass balance equation at the interface can allow to model condensation of non-uniformly saturated vapor, thus, extending use of the model. Furthermore, evaporation can be introduced in the model as further development of the approach.

Since the model displays good agreement with empirical models for film condensation beyond the laminar flow the next improvement would be to develop accurate simulations of turbulent film flows in three dimensions.

Conflict of interest

None declared.

Acknowledgment

This work is a part of research activities within the Center of Reliable Power Electronics (CORPE) funded by the Danish Strategic Research Council. We thank the Aerothermochemistry and Combustion Systems Laboratory of ETH for the hospitality during the stay of M.A.H. and Shyam Chikatamarla for helping setting up the ELB simulations in the beginning.

I.V.K. gratefully acknowledges support by the ERC Advanced Grant 291094-ELBM.

References

- [1] R. Bird, W. Stewart, E. Lightfoot, *Transport Phenomena*, Wiley, Wiley International edition, 2007.
- [2] S. Ghiaasiaan, *Two-Phase Flow, Boiling, and Condensation*, Cambridge University Press, In Conventional and Miniature Systems, 2007.
- [3] W. Nusselt, Die Oberflächenkondensation des Wasserdampfes the surface condensation of water, *Zetschr. Ver. Deutch. Ing.* 60 (1916) 541–546.
- [4] M.M. Chen, An analytical study of laminar film condensation: part 1 flat plates, *J. Heat Transfer* 83 (1) (1961) 48–54.
- [5] J. Koh, E. Sparrow, J. Hartnett, The two phase boundary layer in laminar film condensation, *Int. J. Heat Mass Transfer* 2 (1) (1961) 69–82.
- [6] P.L. Kapitza, Wave flow of thin layers of a viscous fluid, i. the free flow, *Zh. Eksperim. Theor. Fiz.* 18 (3) (1916) 541–546.
- [7] F. Higuera, S. Succi, R. Benzi, Lattice gas dynamics with enhanced collisions, *EPL (Europhys. Lett.)* 9 (4) (1989) 345–349.
- [8] Y. Qian, D. d'Humières, P. Lallemand, Lattice BGK models for Navier-Stokes equation, *EPL (Europhys. Lett.)* 17 (6) (1992) 479–484.
- [9] X. Shan, X. He, Discretization of the velocity space in the solution of the Boltzmann equation, *Phys. Rev. Lett.* 80 (1998) 65–68.
- [10] I.V. Karlin, A.N. Gorbun, S. Succi, V. Boffi, Maximum entropy principle for lattice kinetic equations, *Phys. Rev. Lett.* 81 (1998) 6–9.
- [11] I. Karlin, A. Ferrante, H. Öttinger, Perfect entropy functions of the lattice Boltzmann method, *EPL (Europhys. Lett.)* 47 (2) (1999) 182–188.
- [12] S. Ansumali, I. Karlin, H. Öttinger, Minimal entropic kinetic models for hydrodynamics, *EPL (Europhys. Lett.)* 63 (6) (2003) 798–804.
- [13] S. Ansumali, I.V. Karlin, H.C. Öttinger, Thermodynamic theory of incompressible hydrodynamics, *Phys. Rev. Lett.* 94 (2005) 080602.
- [14] S. Ansumali, I.V. Karlin, Consistent lattice Boltzmann method, *Phys. Rev. Lett.* 95 (2005) 260605.
- [15] S. Succi, *The Lattice-Boltzmann Equation*, Oxford University Press, Oxford, 2001.
- [16] X. Liu, P. Cheng, Lattice Boltzmann simulation of steady laminar film condensation on a vertical hydrophilic subcooled flat plate, *Int. J. Heat Mass Transfer* 62 (2013) 507–514.
- [17] X. Liu, P. Cheng, Lattice Boltzmann simulation for dropwise condensation of vapor along vertical hydrophobic flat plates, *Int. J. Heat Mass Transfer* 64 (2013) 1041–1052.
- [18] I. Ginzburg, K. Steiner, Lattice Boltzmann model for free-surface flow and its application to filling process in casting, *J. Comput. Phys.* 185 (1) (2003) 61–99.
- [19] N. Thürey, C. Körner, U. Rüde, Interactive free surface fluids with the lattice Boltzmann method, Technical Report 05-4. University of Erlangen-Nuremberg, Germany.
- [20] U. Rüde, N. Thürey, Free surface lattice-Boltzmann fluid simulations with and without level sets, in: *Vision, Modeling, and Visualization 2004: Proceedings*, November 16–18, 2004, USA, IOS Press, Stanford, 2004, p. 199.
- [21] N. Thürey, U. Rüde, Stable free surface flows with the lattice Boltzmann method on adaptively coarsened grids, *Comput. Visual. Sci.* 12 (5) (2009) 247–263.
- [22] I.V. Karlin, S. Succi, S.S. Chikatamarla, Comment on numerics of the lattice Boltzmann method: effects of collision models on the lattice boltzmann simulations, *Phys. Rev. E* 84 (2011) 068701.
- [23] A. Kupershtokh, New method of incorporating a body force term into the lattice Boltzmann equation, in: *Proceedings of the 5th International EHD Workshop*, University of Poitiers, Poitiers, France, 2004, pp. 241–246.
- [24] S.S. Chikatamarla, S. Ansumali, I.V. Karlin, Entropic lattice Boltzmann models for hydrodynamics in three dimensions, *Phys. Rev. Lett.* 97 (2006) 010201.
- [25] X. He, S. Chen, G.D. Doolen, A novel thermal model for the lattice boltzmann method in incompressible limit, *J. Comput. Phys.* 146 (1) (1998) 282–300.
- [26] I.V. Karlin, D. Sichau, S.S. Chikatamarla, Consistent two-population lattice Boltzmann model for thermal flows, *Phys. Rev. E* 88 (2013) 063310.
- [27] N. Thürey, C. Wojtan, M. Gross, G. Turk, A multiscale approach to mesh-based surface tension flows, *ACM Transactions on Graphics (TOG)*, Vol. 29, ACM, 2010, p. 48.
- [28] X. Xing, D.L. Butler, C. Yang, A lattice boltzmann based single-phase method for modeling surface tension and wetting, *Comput. Mater. Sci.* 39 (2) (2007) 282–290.
- [29] Q. Zou, X. He, On pressure and velocity boundary conditions for the lattice Boltzmann BGK model, *Phys. Fluids* 9 (6) (1997) 1591–1598 (1994–present).
- [30] S. Kutateladze, Semi-empirical theory of film condensation of pure vapours, *Int. J. Heat Mass Transfer* 25 (5) (1982) 653–660.
- [31] S. Chen, F. Gerner, C. Tien, General film condensation correlations, *Exp. Heat Transfer Int. J.* 1 (2) (1987) 93–107.

Paper C

Humidity evolution (breathing effect) in enclosures
with electronics

Morten A. Hygum, Vladimir N. Popok

The paper has been accepted for the
The IMAPS Nordic Annual Conference Proceedings June 8-9, 2015, Helsingør,
Denmark.

© 2015 IMAPS – Nordic
The layout has been revised.

Humidity evolution (breathing effect) in enclosures with electronics

Morten A. Hygum and Vladimir N. Popok

Aalborg University, Skjernvej 4a, 9220 Aalborg East, Denmark

Phone:+45 9940 9215, Fax:+45 9940 9235 and E-mail: mah@nano.aau.dk

Abstract

Packaging and enclosures used for protecting power electronics operating outdoors are designed to withstand the local climatic and environmental changes. Hermetic enclosures are expensive and therefore other solutions for protecting the electronics from a harsh environment are required. One of the dangerous parameters is high humidity of air. Moisture can inevitable reach the electronics either due to diffusion through the wall of an enclosure or small holes, which are designed for electrical or other connections. A driving force for humid air movement is the temperature difference between the operating electronics and the surrounding environment. This temperature, thus, gives rise to a natural convection, which we also refer to as breathing. Robust and intelligent enclosure designs must account for this breathing as it can significantly change the humidity distribution in the enclosure.

In the current work we suggest a modelling procedure to investigate a breathing effect for an enclosure with opening (hole). The simulations are carried out by solving an energy equation coupled with the Navier-Stokes equation. The movement of moisture is considered through a convection-diffusion equation. The approach is verified by measuring the temperature and humidity profiles in a test setup (container) while also considering the moisture flux outside the container. The test setup is a vertical cylinder enabling to simplify the modeling to 2D case. The experimental measurements are compared to simulations and good agreement is obtained.

Key words: Modeling of humidity distribution, Enclosures with electronics.

1 Introduction

In reliability engineering a significant issue is the problem of climatic simulations which includes the aspect of relative humidity (RH) of air. It is a well-known fact that a humid climate greatly affects the lifetime of electronics.

Completely hermetic boxes or cabinets are quite expensive and therefore not used in routine packaging technology. The humidity and temperature inside a cabinet are thus affected by the climate outside the packaging e.g. through small openings. Operating electronics inevitably heats the environment inside an enclosure in which it is installed. Thus, the packaging will be exposed to thermal gradients. Due to gravity, this leads to pressure gradients in the air inside the enclosure that gives rise to movement of the air. This natural convection, sometimes also referred to as breathing, can transport water vapor from/in the enclosure. In order to design not expensive and intelligent packaging solutions which ensure good reliability towards high humidity, simulations based on the physics-based climatic models of such systems are of importance.

To our knowledge, a significant attention has been paid to predict the moisture absorption by the

electronic packaging, the moisture distribution inside the encapsulating material and at circuit boards, see e.g. [1, 2, 3, 4, 5]. However, approaches to predict the climatic conditions, to which the electronics is exposed to, have not been intensively studied. Here, an investigation of the water vapor mass flow through openings in a test setup (enclosure) is presented. The experiments are designed to obtain the values of the mass flow through the openings of different diameters.

2 Theory

Theoretical prediction of natural convection is a complicated matter because it involves coupling the Navier-Stokes equations with the energy equation using Boussinesq approximation. The generated pressure gradient is considered with a buoyancy force and the air is set to be incompressible [7]. The momentum conservation equation is

$$\rho \left(\frac{\partial \vec{u}}{\partial t} + (\nabla \vec{u}) \cdot \vec{u} \right) = -\nabla p + \vec{\nabla} \cdot \tau + \vec{f}, \quad (1)$$

where ρ is the density, t is the time, p is the pressure, \vec{f} is the body force and the viscous stress tensor is

$$\tau = \nu (\nabla \vec{u} + (\nabla \vec{u})^T) - \frac{2}{3} \nu (\nabla \vec{u}) \mathbf{I}, \quad (2)$$

with I to be the identity matrix and ν to be the dynamic viscosity. The velocity field \vec{u} obeys the continuity equation for incompressible fluids

$$\frac{\partial \rho}{\partial t} + \rho \vec{\nabla} \cdot \vec{u} = 0. \quad (3)$$

Equation (1) and (2) are the Navier-Stokes equations. The continuity equation for the energy is

$$\rho C_p \frac{\partial T}{\partial t} + \rho C_p \vec{u} \cdot \nabla T = \nabla \cdot (k \nabla T) + Q, \quad (4)$$

with C_p to be the heat capacity at constant pressure, T to be the temperature, k to be the heat conductivity and Q to be a source term. The coupling between equation (1) and (3) is through the body force term \vec{f} . The Boussinesq approximation enables:

$$\vec{f} = \rho \vec{g} = (\bar{\rho} - \bar{\rho} \beta (T - \bar{T})) \vec{g}, \quad (5)$$

where β is the thermal expansion coefficient and \vec{g} is the acceleration due to gravity. In this study these non-linear, coupled partial differential equations must be solved numerically. By simultaneously solving of the equations the temperature and movement of the air inside the enclosure is obtained. For reliability engineering the amount of water vapor in the air is the most critical parameter. The transport of water vapor can be modeled as movement of a diluted species in air. This is likewise governed by the continuity equation:

$$\frac{\partial c}{\partial t} + \vec{\nabla} \cdot \vec{J} = 0, \quad (6)$$

where c is the concentration of water vapor and \vec{J} is the vapor flux, which is divided into a diffusion part and a convective part, as follows:

$$\vec{J} = -D_c \vec{\nabla} c + c \vec{u}, \quad (7)$$

with D_c to be the diffusion coefficient [6, 7]. The vapor pressure is given as

$$p_v = cRT, \quad (8)$$

with R as the ideal gas constant. The vapor pressure allows the RH obtained from

$$RH = \frac{p_v}{p_{sat}}, \quad (9)$$

where p_{sat} is the saturated vapor pressure.

2 Experiments

The test setup is made in shape of a cylinder that allows to reduce the model to a 2D axisymmetric domain. A cylindrical wetted sponge was then inserted into the middle of the cylinder with a steel wire, where the other end of the steel wire was attached to a scale which was placed over the test setup. At the top of the tube an end cap was mounted with a small hole in the middle. The hole size was varied for each experimental series. At the bottom of the tube a Peltier element was mounted. A schematic of the setup is shown in figure 1.

The experiments were conducted by lowering the wetted sponge into the test setup, attaching the other end of the steel wire to a scale

above the setup, covering the opening with a napkin to avoid convective disturbance from the surroundings. Then, one should wait until the air inside the tube was saturated with water vapor and weigh the sponge. The next stage was to heat the setup using the Peltier element. After the heating procedure was done the sponge was weighed again and an average flux of water vapor through the opening could be calculated from the known mass difference of the sponge and evaporation time. The starting temperature of the experiments was 21°C.

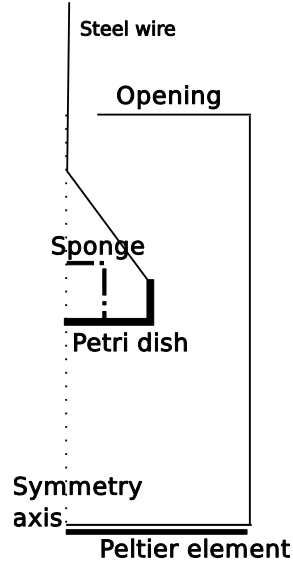


Figure 1: 2D schematic of the half of the cylindrical setup.

To obtain significantly weight losses from the sponge the heating profile was applied 3-5 times in a row depending on the size of the opening. To isolate sources of error, two different heating profiles were tested. The first profile is shown in figure 2 while the second profile is shown in figure 3. The first heating profile was carried out by heating the device to 29°C and letting the device cool. This was done to mimic an operating circuit board. Reasons for the second profiles are mentioned in detail in section 5.

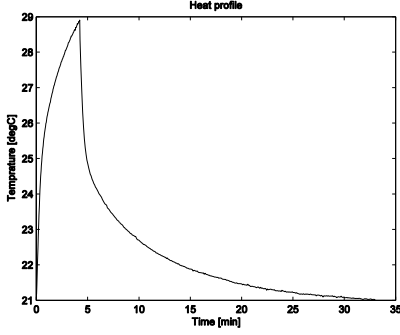


Figure 2: The first heating profile as a function of time.

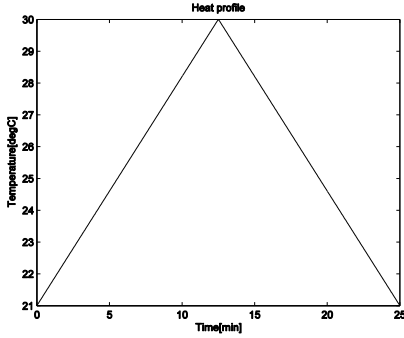


Figure 3: The second heating profile as a function of time.

4 Modeling

The modelling was carried out with COMSOL Multiphysics. All material properties are that of humid air and obtained from [8].

The heating profile was loaded into the software and applied as a boundary condition at the bottom of the tube. Otherwise all boundary conditions and initial conditions were set to $T = 21^\circ\text{C}$.

The initial condition was set to still air. All the walls are set to no-slip conditions. At the opening the pressure was set to atmospheric value.

Throughout the chamber, the no-flux boundary condition was used, except for the opening and the sponge. At the sponge, the water vapor concentration was set to that of a RH of 100 %, as follows:

$$c_{\text{sponge}} = \frac{p_{\text{sat}}}{RT}, \quad (10)$$

where the saturated vapor pressure p_{sat} for water vapor is given as [9]

$$p_{\text{sat}}(T) = 2.53 \cdot 10^{11} e^{-\frac{2.501 \cdot 10^6}{461.5 T}} [\text{Pa}]. \quad (11)$$

At the opening the following boundary condition was applied:

$$c_{\text{opening}} = \frac{p_{\text{sat}}}{2RT}, \quad (12)$$

which amounts to the water vapor concentration of a RH of 50 %. The initial condition was the vapor concentration corresponding to a RH of 90 %.

$$c_{\text{initial}} = 0.9 \frac{p_{\text{sat}}}{RT}, \quad (13)$$

The following diffusion coefficient was used:

$$D_{H_2O,air} = 1.87 \cdot 10^{-6} \cdot T^{2.072} \left[\frac{m^2}{s} \right], \quad (14)$$

which is valid for the temperature range 282-450K [10].

5

Results and discussion

The modeled and measured average dissipation of vapor for the first heating profile are shown in table 1. Since the values are small we consider the agreement to be satisfactory (same order of magnitude) for small openings. The larger difference between the model and experiments for the opening with radius 2 cm is believed to be due to convective disturbances of the test setup surrounding Movement of air at the top of the cylinder would mix the air from outside the setup with the air inside it. This would lead to larger concentration gradients in water vapor which causes large diffusion flux of water vapor out of the setup. Another possible error, which is worth mentioning, is that the model being done with the Boussinesq approximation itself leading to not very appropriate simulation of the air compression inside the cylinder. Thus, the deviations in the heating profile can cause a difference between the model and experiments.

Table 1. Calculated and measured dissipation of vapor for heat profile in the first series of experiments.

OPENING RADIUS	MODELED DISSIPATION	MEASURED DISSIPATION
0.5[cm]	0.0031[mol]	0.0083±0.019[mol]
1[cm]	0.0033[mol]	0.0087±0.0021[mol]
2[cm]	0.0037[mol]	0.311±0.0196[mol]

To eliminate possible errors due to the heating profile shown in Fig. 2 we applied simpler and better controlled heating profile illustrated in figure 3. Furthermore, to lower the effect from the surrounding of the experimental setup a smaller opening was used for these experiments. The modeled and measured average dissipation of vapor for the second series of experiments is shown in table 2 demonstrating much better agreement compared to the first heating profile, thus, convincing that the deviations between the simulations and experiments are most probably related to uncontrolled air disturbances outside the setup.

Table 2. Calculated and measured dissipation of vapor for heat profile in the second series of experiments.

OPENING RADIUS	MODELED DISSIPATION	MEASURED DISSIPATION
0.25[cm]	0.0021[mol]	0.0015±0.00067[mol]

The modeled RH and temperature distributions for the first heating profile at t=251 s. are shown in figure 4 and 5, respectively.

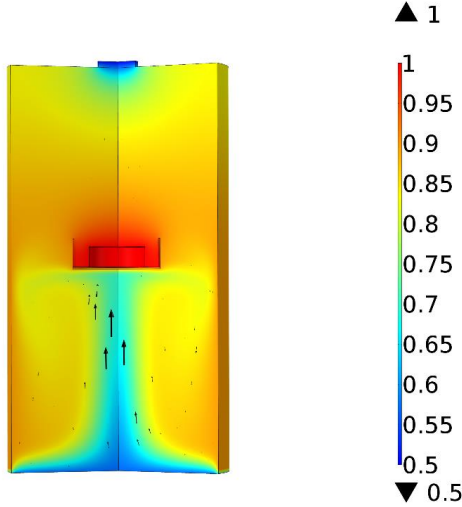


Figure 4: The modeled RH distribution after 251 s for the first heating profile. The black arrows indicate the natural convection.

In figure 6 and 7 the temperature and RH, respectively, for the experiments and simulations are compared. This comparison is done for the first heating profile but the trend is observed to be nearly the same for the other measurements and simulations. It is seen that the model underestimates the transient shift in the temperature and therefore also leads to deviation from the experimental data for RH.

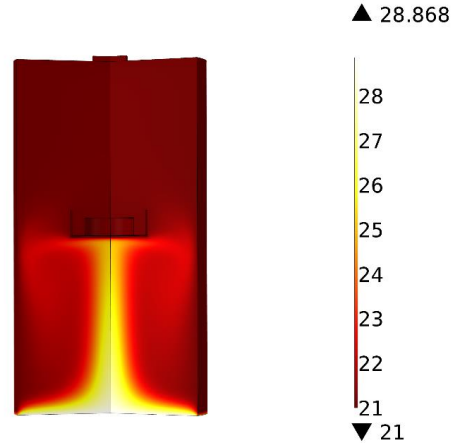


Figure 5: The modeled temperature distribution after 251 s for the first heat profile.

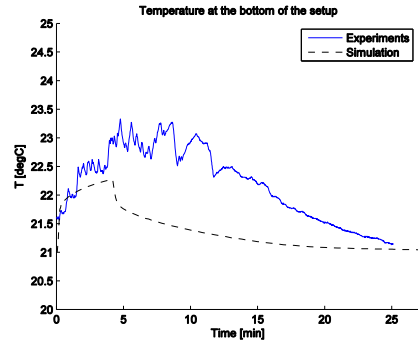


Figure 6: The temperature as a function of time in the bottom of the test setup for the first heating profile.

As mentioned, the model does not account for some convective disturbance from the surrounding of the setup. Thus, the model is expected to, somewhat underestimate the transient behavior of the temperature, since convective surrounding enhances stirring in the setup and rises the heat flux at the bottom. Hence, more energy is released in the setup.

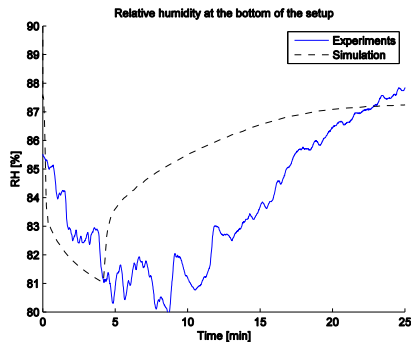


Figure 7: The RH as a function of time in the bottom of the test setup for the first heating profile.

6

Conclusion

The water vapor dissipation was model using the Boussinesq approximation combined the Navier-Stokes equations and the continuity equation for heat and vapor. Experiments provided reasonable agreement with the simulations, at least showing the same order of magnitude values for the vapor flux. The found deviations between the calculated and measured data were related to uncontrolled air disturbances outside the experimental setup.

The presented approach, thus, can, be suggested as a tool to design and optimize packaging technologies with respect to humidity.

Acknowledgements

This work is a part of research activities within the Center of Reliable Power Electronics (CORPE) funded by the Danish Strategic Research Council (currently Innovation Fund Denmark).

References

- [1] Ee Hua Wong, Yong Chua Teo, and Thiam Beng Lim. Moisture diffusion and vapour pressure modeling of ic packaging. In *Elec. Comp. amp; Tech. Conf., 1998. 48th IEEE*, pages 1372–1378, May 1998.
- [2] EH Wong, R Rajoo, SW Koh, and TB Lim. The mechanics and impact of hygroscopic swelling of polymeric materials in electronic packaging. *Journal of Electronic Packaging*, 124(2):122–126, 2002.
- [3] Jiang Zhou and Japhet S Law. Effect of non-uniform moisture distribution on the hygroscopic swelling coefficient. *Comp. and Pack. Techn., IEEE Transactions on*, 31(2):269–276, 2008.
- [4] B Xie, XJ Fan, XQ Shi, and H Ding. Direct concentration approach of moisture diffusion and whole-field vapor pressure modeling for reflow process -part i: theory and numerical

implementation. *J. Elect.Pack.*, 131(3):031010, 2009.

- [5] Haleh Ardebili, Craig Hillman, Marjorie Ann Erickson Natishan, Patrick McCluskey, Michael G Pecht, and Dave Peterson. A comparison of the theory of moisture diffusion in plastic encapsulated microelectronics with moisture sensor chip and weight-gain measurements. *Comp. and Pack. Techn., IEEE Transactions on*, 25(1):132–139, 2002.
- [6] H. Bruus. *Theoretical Microfluidics*. Oxford University Press, New York, 2008.
- [7] R.B. Bird, W.E. Stewart, and E.N. Lightfoot. *Transport Phenomena*. Wiley International edition. Wiley, 2007.
- [8] Jiehei Zhang, Ajaykumar Gupta, and John Baker. Effect of relative humidity on the prediction of natural convection heat transfer coefficients. *Heat transfer engineering*, 28(4):335–342, 2007.
- [9] Mark G Lawrence. The relationship between relative humidity and the dewpoint temperature in moist air: a simple conversion and applications. *Bulletin of the American Meteorological Society*, 86(2), 2005.
- [10] T.R. Marrero and E. A. Mason. Gaseous diffusion coefficients. *J. Phys. and Chem. Ref. Data*, 1(1):3–118, 1972.

Paper D

Modeling of humidity-related reliability in enclosures with electronics

Morten A. Hygum, Vladimir N. Popok

The paper has been accepted for the
The IMAPS Nordic Annual Conference Proceedings June 8-9, 2015, Helsingør,
Denmark.

© 2015 IMAPS – Nordic
The layout has been revised.

Modeling of humidity-related reliability in enclosures with electronics

Morten A. Hygum and Vladimir N. Popok

Aalborg University, Skjernvej 4a, 9220 Aalborg East, Denmark

Phone:+45 9940 9215, Fax:+45 9940 9235 and E-mail: mah@nano.aau.dk

Abstract

Reliability of electronics that operate outdoor is strongly affected by environmental factors such as temperature and humidity. Fluctuations of these parameters can lead to water condensation inside enclosures. Therefore, modelling of humidity distribution in a container with air and freely exposed water is of importance for reliability engineering.

Reliability assessment of large complex systems is often done by dividing the complex into decoupled subsystems. The reliability of such system is then obtained by combining the reliability of each subsystem. In this paper we set up a framework to predict humidity-related reliability of a printed circuit board (PCB) located in a cabinet by combining structural reliability methods and non-linear diffusion models. This framework can, thus, be used for reliability prediction from a climatic point-of-view. The proposed numerical approach is then tested to estimate the reliability of a case example with liquid water at the bottom of a cabinet and PCB positioned on one of the walls. The water vapor profile inside the enclosure is calculated using a diffusion equation whereas the release of vapor from the water surface is modeled using statistical rate theory. The novelty in this work lies within the reliability prediction based on physical modeling of the climate in the system of interest.

Key words: Modeling of humidity distribution, Statistical rate theory, Humidity-related reliability, Enclosures with electronics.

1 Introduction

A significant issue in reliability engineering is the problem of climatic simulations which includes the aspect of relative humidity of air. Some electronics operate outdoor and are, thus, exposed to daily alterations of temperature and humidity. It is a well-known fact that a humid climate greatly affects the reliability of electronics. Catastrophic failure can occur if water condenses on a PCB short-circuiting the electronic devices. Corrosion is, likewise, one more well-known failure mechanism. If the circuit board is exposed to a high relative humidity (RH) moisture can diffuse through the encapsulation and oxidize the wiring. See for example [1] for various reliability models for PCB with RH as the stressing factor. Since completely hermetic boxes or cabinets are quite expensive, accurate reliability models based on the physical climatic models of such systems are of importance.

Much attention has been paid to predict the moisture absorption by the electronic packaging, the moisture distribution inside the encapsulating material and circuit boards, see e.g. [2-6]. However, approaches to predict the reliability using climatic simulation for enclosures have not been intensively studied. This type of simulations should include appropriate physics-based model for the humidity

distribution and evolution as a first step. Descriptions of humidity distribution affected by freely exposed water surfaces require accurate models for the vapor flux at the water-interfaces. For this framework the statistical rate theory (SRT) approach for the interface flux can be used [7-9]. It is experimentally verified and it offers climatic modeling of enclosures without any fitting parameters, making it to be a general-purpose method applicable for reliability prediction and as a design tool.

Following the philosophy suggested in [10] proper design for reliability should originate from physical understanding of the system. Therefore, the model presented in this paper is SRT-based approach for the simulation of the humidity profile in a container of given geometry with a condensed water and the simulated humidity distribution can be applied for the prediction of failure of electronics. Thus, the tool provides opportunities for intelligent packaging design and/or reliability assessment.

In this paper the case example is restricted to an enclosure with no temperature gradients at steady state and diffusion is considered as the main contributor to the transport of water vapor in air. Thus, it mimics an outdoor cabinet at night with no operating electronics. However, the proposed framework is not restricted to such relatively simple

inside the enclosure. Thus, we consider a given value of RH to be the failing criterion. In other words, as soon as RH reaches this value at the location of a circuit board it should fail. RH is simulated using the approach briefly described in section 2.1.

3 Modeling

In moisture-related reliability, the RH is of interest. It is given by

$$RH = \frac{p_v}{p_{sat}}, \quad (9)$$

with the saturated vapor pressure for water vapor given as [14]

$$p_{sat}(T) = 2.53 \cdot 10^{11} e^{-\frac{2.501 \cdot 10^6}{T - 461.5}} [Pa], \quad (10)$$

The vapor pressure p_v follows the ideal gas equation:

$$p_v = cRT, \quad (11)$$

where R , here, is the gas constant. To predict the humidity distribution, the diffusion constant of water vapor in air is needed. At atmospheric pressure, it has been experimentally determined to be

$$D_{H_2O,air} = 1.87 \cdot 10^{-6} \cdot T^{2.072} \left[\frac{m^2}{s} \right], \quad (12)$$

which holds in the temperature range 282-450K [15].

The steady-state water vapor distribution was obtained using the finite volume method. The iteration approach was an over relaxed Gauss-Seidel scheme with a relaxation factor of $\omega = 1.9$. The water vapor flux at the water-air interface was calculated using the Newton-Raphson method. For more details on the iteration scheme, see e.g. [16] or [17]. Furthermore, for computational reasons the model is kept two dimensional.

In the model three stochastic variables were considered. The half-width length, L , of the opening in the enclosure, the temperature T and RH outside, RH_{out} . In table 1 the simulation parameters for the stochastic variables are given.

Table 1. Simulation parameters for stochastic variables.

VARIABLE	DISTRIBUTION	MEAN	STD. DEV.
$L[L_x]$	Log Normal	0.0135	$1.35 \cdot 10^{-6}$
$T[K]$	Normal	303	10
RH_{out}	Normal	0.6	0.02

At the walls of the enclosure no-flux boundary conditions were applied. For the opening the following concentration boundary condition was used:

$$c_0 = RH_{out} \frac{p_{sat}}{RT}. \quad (13)$$

Finally, a failing criterion must be defined. Here, we put the criterion to be a maximum value of relative humidity RH_f at the bottom of the circuit board,

located $L_y/3$ below the top wall of the enclosure. Estimation of RH_f is beyond the tasks of the current paper. Some examples will be discussed in the next section.

A flowchart of the solving procedure is shown in figure 2.

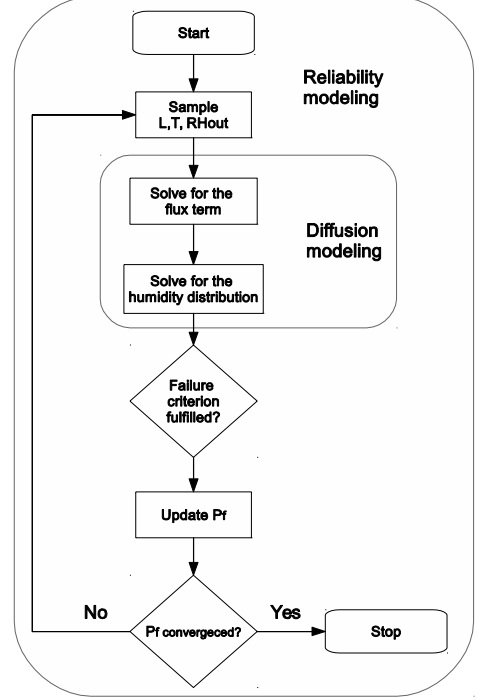


Figure 2: Illustration of the solving procedure.

4 Results

The diffusion problem was solved using 100 control volumes of equal size in each direction. Every length in the x-direction is normalized to L_x and likewise for the y-direction. Finally, the convergence criterion for the diffusion problem was set so that on average the change in the water vapor concentration at the control volumes was $\Delta c < 10^{-4} mol \cdot m^{-3}$.

A RH profile, generated by the sampling procedure, for a case with the stochastic inputs sampled to be $T = 300K$, $RH_{out} = 0.62$ and $L = 0.0133L_x$ is shown in figure 3. One can see that the RH is highest just above the water surface and lowest at the opening, as expected.

Histograms of all the sampled values of T , RH_{out} and L for the simulation with $RH_f = 0.9$ are presented in figures 4, 5 and 6, respectively. The histograms are shown with a rescaled frequency in

order to compare with the associated probability density functions (PDF) for the stochastic inputs. The rescaling is done so that the total area of the bins is equal to unity. From figures 4-6 it is clear that the sampling procedure has generated enough data for the histograms to recover the associated PDFs.

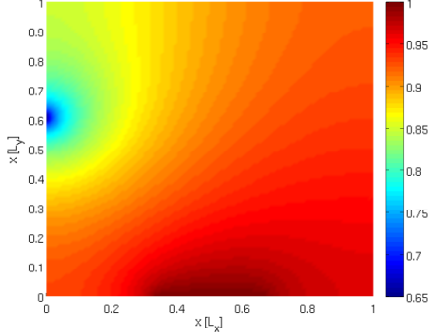


Figure 3: Simulated RH profile in the enclosure with be $T = 300K$, $RH_{out} = 0.62$ and $L = 0.0133L_x$.

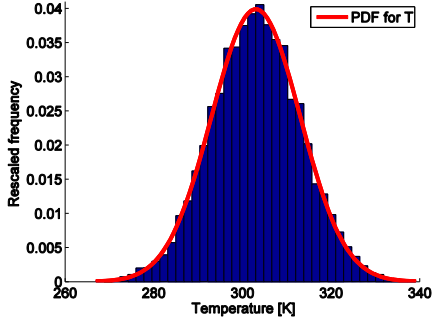


Figure 4: Histogram of the sampled T .

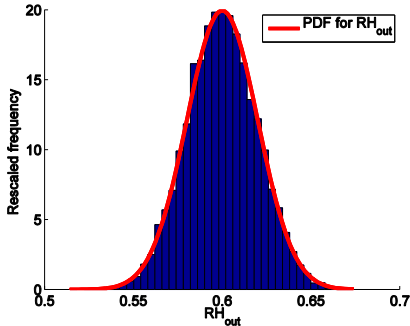


Figure 5: Histogram of the sampled RH_{out} .

The probability of failure for three different failing criteria was modeled with a convergence match of 10^{-5} . The obtained P_f corresponding to different RH_f are given in table 2. The table shows how the

choice of the failing criterion directly affects P_f . It is found that small increase of RH from 0.90 to 0.95 as a failing criterion significantly decreases the probability of failure. Further increase of RH_f leads to a significantly smaller failure probability of 0.044.

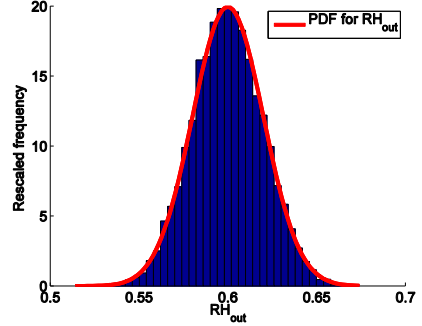


Figure 6: Histogram of the sampled L .

Table 2. Simulated failure probabilities

FAILING CRITERION	P_f
$RH_f = 0.9$	1.000
$RH_f = 0.95$	0.320
$RH_f = 0.98$	0.044

Humidity-related failing criterion can be found experimentally for a particular type of PCB and operational conditions. One can see some examples in [18] where the RH issue was combined with presence of chemicals (residuals of organic acids after soldering). Overcoming of RH_f does typically not lead to immediate catastrophic failure. However, leakage currents are significantly and stepwise increased promoting electrochemical migration and accelerated corrosion which finally causes the failure.

5

Conclusion

Reliability prediction model based on climatic simulations in enclosures is described. The climatic simulation predicts humidity distribution in a box of given configuration. Diffusion is considered to be the predominant transport mechanism of water vapor in the enclosure with the water vapor flux at the water-air interface described according to SRT. Thus, this part of the model is based on the appropriate description of physical phenomena in the framework of fluid dynamics. The failure probability is calculated by a Monte Carlo method, thus, linking the calculated RH at the given location with the humidity-related failing criterion for the electronic circuit. Hence, the humidity-related reliability of the device inside an enclosure can be estimated. The developed framework for the reliability prediction is not limited to only humidity. Any other failure criteria can be

used in the similar way. The predictions can be also developed for more complex geometries of enclosures.

Further improvements of the framework can be done by including thermal gradients and convection of the air inside the enclosure. The probability of failure, predicted by our Monte Carlo approach, can also be compared to other reliability prediction methods, for example, the first- or second order reliability method known from structural reliability [13].

Acknowledgements

This work is a part of research activities within the Center of Reliable Power Electronics (CORPE) funded by the Danish Strategic Research Council.

References

- [1] McPherson, J., 2013. Reliability Physics and Engineering: Time-To-Failure Modeling. Bücher. Springer.
- [2] Wong, E. H., Teo, Y. C., and Lim, T. B., 1998. "Moisture diffusion and vapour pressure modeling of ic packaging". In Elec. Comp. amp; Tech. Conf., 1998. 48th IEEE, pp. 1372–1378.
- [3] Wong, E., Rajoo, R., Koh, S., and Lim, T., 2002. "The mechanics and impact of hygroscopic swelling of polymeric materials in electronic packaging". Journal of Electronic Packaging, 124(2), pp. 122–126.
- [4] Zhou, J., and Law, J. S., 2008. "Effect of non-uniform moisture distribution on the hygroscopic swelling coefficient". Comp. and Pack. Techn., IEEE Transactions on, 31(2), pp. 269–276.
- [5] Xie, B., Fan, X., Shi, X., and Ding, H., 2009. "Direct concentration approach of moisture diffusion and whole-field vapor pressure modeling for reflow processpart i: theory and numerical implementation". J. Elect. Pack., 131(3), p. 031010.
- [6] Ardebili, H., Hillman, C., Natishan, M. A. E., Mc-Cluskey, P., Pecht, M. G., and Peterson, D., 2002. "A comparison of the theory of moisture diffusion in plastic encapsulated microelectronics with moisture sensor chip and weight-gain measurements". Comp. and Pack. Techn., IEEE Transactions on, 25(1), pp. 132–139.
- [7] Ward, C. A., and Stanga, D., 2001. "Interfacial conditions during evaporation or condensation of water". Phys. Rev. E, 64, p. 051509.
- [8] Fang, G., and Ward, C., 1999. "Temperature measured close to the interface of an evaporating liquid". Phys. Rev. E, 59(1), p. 417.
- [9] Ward, C., and Fang, G., 1999. "Expression for predicting liquid evaporation flux: Statistical rate theory approach". Phys. Rev. E, 59(1), p. 429.
- [10] Wang, H., Liserre, M., Blaabjerg, F., de Place Rikken, P., Jacobsen, J., Kvisgaard, T., and Landkildehus, J., 2014. "Transitioning to physics-of-failure as a reliability driver in power electronics". Emerging and Selected Topics in Power Electronics, IEEE Journal of, 2(1), pp. 97–114.
- [11] Hygum, M. A., and Popok, V. N., 2014. "Humidity distribution affected by freely exposed water surfaces: Simulations and experimental verification". Phys. Rev. E, 90, Jul, p. 013023.
- [12] Bruus, H., 2008. Theoretical Microfluidics. Oxford University Press, New York.
- [13] Choi, S., Grandhi, R., and Canfield, R., 2006. Reliability-based Structural Design. Springer, London.
- [14] Lawrence, M. G., 2005. "The relationship between relative humidity and the dewpoint temperature in moist air: a simple conversion and applications". Bulletin of the American Meteorological Society, 86(2).
- [15] Marrero, T., and Mason, E. A., 1972. "Gaseous diffusion coefficients". J. Phys. and Chem. Ref. Data, 1(1), pp. 3–118.
- [16] Versteeg, H., and Malalasekera, W., 2007. An Introduction to Computational Fluid Dynamics: The Finite Volume Method. Pearson Education, London.
- [17] Patankar, S., 1980. Numerical Heat Transfer and Fluid Flow. Taylor & Francis.
- [18] Verdinovas, V., Jellesen, M.S., Ambat, R., 2015. "Solder Flux Residues and Humidity-Related Failures in Electronics: Relative Effects of Weak Organic Acids Used in No-Clean Flux Systems". Journal of Electronic Materials 44(4), pp. 1116–1127.